

DOE/ET-53088-586

IFSR #586

Statistical Behavior of Filamentary Plasmas

RODNEY MICHAEL KINNEY
Institute for Fusion Studies
The University of Texas at Austin
Austin, Texas 78712

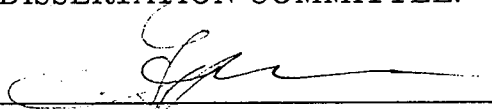
(THESIS)

December 1992

STATISTICAL BEHAVIOR OF FILAMENTARY PLASMAS

APPROVED BY
DISSERTATION COMMITTEE:

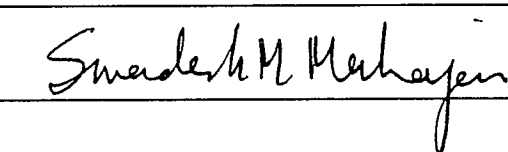
Supervisor:











**STATISTICAL BEHAVIOR OF FILAMENTARY
PLASMAS**

by

RODNEY MICHAEL KINNEY, B.S.

DISSERTATION

Presented to the Faculty of the Graduate School of

The University of Texas at Austin

in Partial Fulfillment

of the Requirements

for the Degree of

DOCTOR OF PHILOSOPHY

THE UNIVERSITY OF TEXAS AT AUSTIN

December 1992

Dedicated to my family in general, and my parents in particular.

Copyright
by
Rodney Michael Kinney
1992

Acknowledgements

In the face of strong reluctance to state the obvious, I must begin with thanks to Toshi, my advisor. The inspiration, guidance, and great personal freedom he gave me have made my graduate experience both pleasant and productive. Haruyuki Irie deserves much credit for his contributions to this effort, as do the father-son team Vladimir and Nickolai Petviashvili. Nick especially must be singled out for the close collaboration we have enjoyed. For their interest in this project and for discussions both interesting and helpful, I am grateful to James McWilliams, Bryan Taylor, and Swadesh Mahajan. I also thank Wendell Horton for his recommendations and for agreeing to serve on my committee, for which Phil Morrison and Ethan Vishniac also deserve my thanks.

For setting my mind at ease in matters organizational and administrative, I am indebted to many people. The tremendous support staff at the Institute for Fusion Studies is foremost in this category for their astounding organizational talents. I also thank two people I have never met: Leslie Lamport and Lonnie Abelbeck for their computer tools \LaTeX and Kaleidagraph, helping make science so much prettier. On the low-tech end, I thank the Berol pencil company and especially Staedtler-Mars for their high-quality products, good friends for many years.

Finally, I wish to point out some who have contributed to my general peace of mind while living the graduate experience. I thank Jeff Hellmer for teaching me to play jazz, and many personal influences who should know who they are. Topping this list, of course, is my family, particularly the girl named Lari, Micki, my partner throughout this and all adventures.

STATISTICAL BEHAVIOR OF FILAMENTARY PLASMAS

Publication No. _____

Rodney Michael Kinney, Ph.D.
The University of Texas at Austin, 1992

Supervisor: Toshiki Tajima

This work describes a study of plasmas with highly intermittent filamentary structures. A statistical model of two-dimensional magnetohydrodynamics is presented, based on a representation of the fluid as a collection of discrete current-vorticity concentrations. This approach is modeled after discrete vortex models of hydrodynamical turbulence, which cannot be expected in general to produce results identical to a theory based on a Fourier decomposition of the fields. In a highly intermittent plasma, the induction force is small compared to the convective motion, and when this force is neglected, the plasma vortex system is described by a Hamiltonian. Canonical and micro-canonical statistical calculations show that both the vorticity and the current may exhibit large-scale structure, and the expected states revert to known hydrodynamical states as the magnetic field vanishes. These results differ from previous Fourier-based statistical theories, but it is found that when the filament calculation is expanded to include the inductive force, the results approach the Fourier equilibria in the low-temperature limit, and the previous Hamiltonian plasma vortex results in the high-temperature limit. Numerical simulations of a large number of filaments are carried out and support the theory. A three-dimensional vortex model is outlined as well, which is also Hamiltonian when

the inductive force is neglected. A statistical calculation in the canonical ensemble and numerical simulations show that a non-zero large-scale magnetic field is statistically favored, and that the preferred shape of this field is a long, thin tube of flux.

In a tokamak, a stochastic magnetic field will give rise to strongly filamented current distributions. An external magnetic field possesses field lines described by a non-linear map, while current fluctuations along these field lines have a toroidal dependence which takes the same form as the time dependence of a system of hydrodynamical vortices. Magnetic surfaces of a tokamak interior in steady state are given by the asymptotic limit of the behavior of the current filaments. Numerical simulations combining the effects of the internal and external fields show that ideal magnetic surfaces are always disrupted by current fluctuations along the field lines, and measures the dependence of the diffusion on external field strength and current fluctuation magnitude.

Table of Contents

| | |
|--|-----------|
| Acknowledgements | v |
| Abstract | vi |
| List of Figures | x |
| Chapter 1. Introduction | 1 |
| Chapter 2. Self-Organization and Structures in Neutral Fluids | 6 |
| 2.1 Basic Hydrodynamical Equations | 6 |
| 2.2 Harmonic Analysis | 8 |
| 2.3 Point-Vortex Representation | 11 |
| 2.4 Simulations of Two-Dimensional Turbulence | 17 |
| Chapter 3. Current Filaments in a Tokamak | 19 |
| 3.1 Taylor's Tokamak Interior Model | 20 |
| 3.2 Interior Model with External Applied Field | 23 |
| 3.3 The Standard Map | 27 |
| 3.4 Computational model | 29 |
| 3.5 Results | 31 |
| Chapter 4. Theory of Two-Dimensional MHD Filaments | 37 |
| 4.1 MHD Harmonic analysis | 37 |
| 4.2 Filamentary Equations of Motion | 39 |
| 4.3 Fixed-Strength Filaments | 43 |
| 4.3.1 Canonical Ensemble | 45 |
| 4.3.2 Microcanonical Ensemble | 47 |
| 4.3.3 Most Probable Filamentary States | 53 |
| 4.4 Variable-Strength Filaments | 55 |

| | |
|---|----------------|
| Chapter 5. Simulations of Two-Dimensional MHD Filaments | 62 |
| 5.1 Numerical Algorithm | 62 |
| 5.2 Constants of the Motion | 66 |
| 5.3 Tests of Known Fixed-Strength Filament Solutions | 67 |
| 5.4 Simulations of Large-N Filament Systems | 73 |
| Chapter 6. Filamentary Objects in Three Dimensional MHD Turbulence | 93 |
| 6.1 Isolated Current-Vorticity Distributions | 94 |
| 6.2 Canonical Ensemble | 96 |
| 6.3 Numerical Study | 99 |
| Chapter 7. Overview | 107 |
| Bibliography | 111 |
| Vita | 118 |

List of Figures

| | | |
|-----|---|----|
| 1.1 | Current columns from a 3-dimensional particle simulation of the coalescence instability. Two columns with parallel currents are attracted, meet explosively, and break up into many smaller currents in (b). | 5 |
| 2.1 | Equilibrium spectra for (a) $\alpha \sim 1$ (b) $0 < \alpha \ll 1$, and (c) $\alpha < 0$ | 12 |
| 3.1 | Phase-space plot (x_n, y_n) for 25,000 iterations of the standard map beginning at a point near the X-point, $(0,0)$. Plot shows stochastic region of the standard map for (a) $U = 0.15 < U_{\text{crit}}$ and (b) $U = 0.20 > U_{\text{crit}}$ | 28 |
| 3.2 | Crosses show computed diffusion time, T_{diff} , versus the parameter U for the standard map. The solid line is the fit calculated by Chirikov. | 30 |
| 3.3 | Plots of mean square diffusion, $\frac{1}{N} \sum_i x_i(t) - x_i(0) ^2$, vs. time for $\kappa = 10^{-4}$. (a) field-dominated regime $U = 2.0$. (b) transition regime $U = 0.15$, (c) current-dominated regime $U = 0$ | 32 |
| 3.4 | T_{diff} , vs. U for $\kappa = 0.05, 0.01, 10^{-3}, 10^{-4}$, and 10^{-5} | 33 |
| 3.5 | Log-log plot of T_{diff} vs. κ . The solid line represents the data from $U = 0$. The o's are from $U = 0.06$, the +'s from $U = 0.15$, and the *'s from $U = 0.20$ | 35 |
| 3.6 | T_{diff} vs. U in the accelerator mode regime. (a) in the absence of self-interaction, $\kappa = 0.0$. (b) for $\kappa = 0.1$. The effect is diminished but still noticeable. (c) for $\kappa = 0.2$ the modes are all but gone. | 36 |
| 4.1 | Magnetic spectra of Fyfe et. al., showing large-scale magnetic island in the negative temperature regime. | 40 |
| 4.2 | Structure functions for (a) the single-species hydrodynamical system, and (b) the $u-w$ system. Solid lines are from theory, while points are histograms from random data samples. The dotted line in (b) is a Gaussian distribution, shown for comparison. | 49 |
| 4.3 | Spectra of $\langle \omega^2 \rangle$ from the $u-w$ micro-canonical ensemble. Positive energies give large-scale velocity field structure. | 52 |

| | | |
|------|--|----|
| 4.4 | Equilibrium spectra of the u - w filamentary system with source included. Regime shown is $ \beta \gg 1$, the low-energy limit for which the spectra approach the Fourier theory's predictions. . . | 60 |
| 4.5 | Spectra of ω and j for $ \beta \sim 1$, the high-energy limit that mimics the behavior of the $S = 0$ approximation. | 61 |
| 5.1 | Paths of two rotating filaments (a), and the time history of their relative distance (b). | 69 |
| 5.2 | Paths of the collapsing trio of u - w filaments. The triangle rotates while shrinking, reflects, and expands. | 71 |
| 5.3 | Plots of λ^2 , vs. t during (a) collapse, (b) bounce, and (c) expansion. The shape of the triangle is maintained during collapse and expansion, but changes slightly during the bounce. | 72 |
| 5.4 | Phase-space plot of u -filament positions for $\tilde{E} \approx 75$ (a) initially and (b) at end of run. | 74 |
| 5.5 | Contours of (a) A_z and (b) Ψ for the final state of the run in the previous figure. | 75 |
| 5.6 | Filament positions from a run with $\tilde{E} \approx 150$. Initial positions are shown in (a). Large clusters of filaments form as in (b), eventually merging to a single clump as in (c). | 76 |
| 5.7 | Filament positions from a run with filaments clustered onto a square lattice. The clusters quickly fall into a stable hexagonal lattice. Marked clusters correspond to the same cluster of filaments at different times, indicating that clusters occasionally interchange sites on the lattice. | 77 |
| 5.8 | Time histories of H for four separate runs with filaments-per-cell of (a) 1, (b) 4, (c) 1/4, and (d) 16. | 79 |
| 5.9 | Time histories of E^u for the same runs as in the previous figure. | 80 |
| 5.10 | Time histories of E^w | 81 |
| 5.11 | Time histories of A | 82 |
| 5.12 | A_z and Ψ contours during $\tilde{E} = 2$ run. | 83 |
| 5.13 | Current and vorticity spectra (a) at a single time-step and (b) averaged over 2000 time steps. $\tilde{E} = 2$ | 85 |
| 5.14 | Current and vorticity spectra (a) at a single time-step and (b) averaged over 2000 time steps. $\tilde{E} = -1$ | 86 |
| 5.15 | Values of the minimum k mode of ω^2 and j^2 from a series of simulations, compared with theory. | 87 |

| | | |
|------|--|-----|
| 5.16 | Time histories and spectra for velocity-dominated $S \neq 0$ run. Diffusion leads to a decay of the invariants and a $1/k^2$ spectrum at large k . Small k values agree with $S = 0$ theory based on average value of H | 88 |
| 5.17 | Time histories and spectra for magnetically-dominated $S \neq 0$ run. As in the previous figure, diffusion alters the large- k spectrum, but the long wavelength behavior agrees with $S = 0$ theory. | 89 |
| 5.18 | Time histories and spectra from velocity-dominated run with diffusion compensated for. Spectra show shape and asymptotic behavior consistent with theory. | 91 |
| 5.19 | Time histories and spectra from magnetically-dominated run with diffusion correction. | 92 |
| 6.1 | Graphical solutions of $x = F(\beta F(\beta x))$ for (a) $\beta = 2$, (b) $\beta = 3$, and (c) $\beta = 4$ | 98 |
| 6.2 | Plots of $D \cdot r$ and r^5 for dipoles collapsing along a line. | 100 |
| 6.3 | Plots of $D \cdot r$ and r^5 for dipoles collapsing along a spiral. | 101 |
| 6.4 | Time histories of the spatial components (a-c) and the magnitude (d) of the total dipole strengths of the u and w fields. Initial conditions are random, from which the two fields grow in opposite directions, generating a magnetic field. | 103 |
| 6.5 | Time history of mean alignment angle between u and w fields for three separate runs with different random initial conditions. | 104 |
| 6.6 | Surfaces of constant B^2 for fixed dipole magnitude run (a) at initial time and (b) as the field begins to organize. | 105 |
| 6.7 | Continuation of the run from the previous figure, showing organization of magnetic field into flux tubes. | 106 |

Chapter 1

Introduction

General plasma dynamics are so complex, and the equations that describe them so intractable that physicists have had great difficulty determining plasma behavior in any degree of generality. While waiting for mathematical techniques for handling non-linear partial differential equations to be developed, the physics community has meanwhile had to rely heavily on its collective ingenuity to wrest information from their models.

Before the age of the calculating machine, much effort was expended on a linearized version of the magnetohydrodynamical (MHD) equations, simply because the assumption rendered the equation soluble in special cases. Eventually, however, the inherent importance of the non-linearity of the plasma equations became clear, and with the convenient introduction of machines capable of calculation significantly quicker than the average human, non-linear problems have begun to become tractable.

As an alternative to what has been the traditional approach of describing a plasma as a collection of potential “instabilities” which may be stable or unstable under certain conditions, and in the face of our inability to solve non-linear partial differential equations analytically, some investigators are looking for probabilistic descriptions of plasmas to shed light on what is happening in these gases. This leads us naturally into the field of statistical mechanics. Mathematically, the formalism of statistical mechanics is applicable to

any system described by a phase space in which the volume is conserved by the system's evolution. Because fundamentally, a fluid is just a whole lot of molecules, one may naively expect a fluid's equilibrium states to conform to the bland Gaussian of true thermodynamic equilibrium. Certainly, if one is sufficiently patient, and in the absence of external influences, any fluid must eventually reach such an equilibrium, but how long must one wait, and what is transpiring meanwhile? The time required for the N bodies to reach their ultimate distribution may be agonizingly long, and they may find some long-lived states in the interim. If the time- and length-scales of a fluid are such that a continuous description is more apt than an N -molecule model, then any statistical analysis should be based on the fluid equations, which will produce states quite different from a particle model.

Because a fluid is a continuous system, very different mathematical tools must be employed in performing the ensemble averages that define statistical mechanics. Tools, in fact, which at the moment barely exist [1]. To perform statistical mechanics as we know it on a fluid system, one must first make some discretization that will approach the continuous system in some limit, and take on faith that the final results will be applicable as well. A point of great subtlety is that discrete representations of continuous objects are in no sense unique, and results obtained via one representation may be quite different from those obtained through another discretization [2].

Two discrete representations which have been shown to be effective in modeling hydrodynamical turbulence in two dimensions are a Fourier-mode representation and a discrete-vortex representation. The two approaches do not yield identical results, but both display interesting thermodynamical features in that the temperature is allowed to be negative (in two dimensions), permitting the system to exhibit self-organizational tendencies. The matter of the difference in results between the two approaches should not be cause to panic into thinking one approach is wrong, but the question of which model

is a fairer representation of reality, and under what conditions, is legitimate. The discrete-vortex model is appealing in that it is a Hamiltonian system, for which great number of mathematical tools are available, but the question of which model more accurately represents a real fluid, like the choice of basing statistics on the fluid equations rather than particle equations, may ultimately be only phenomenologically resolvable.

There is a well-known tendency for a fluid to form very intermittent structures when dissipation is small. In addition to casual observations of naturally-occurring vortices in day-to-day life, experimental observations of thin films of superfluid Helium [3] have been rich in vortex structure. Very high-resolution spectral-based numerical simulations of high Reynolds-number [4, 5] fluids have consistently shown a tendency towards intermittency, specifically a formation of axisymmetric sharply peaked vortex filaments which are quite persistent in time. While such structures can clearly be represented by Fourier modes, the phase correlations represented by the intermittency are very difficult to treat in a statistical theory. Present statistical theories based on Fourier representation are unable to predict the formation of these filaments, the presence of which has significant effects on dynamical quantities such as cascade rates [6].

The case for intermittent structures in plasmas is equally strong, if not stronger. Pouquet, in an analysis of two-dimensional MHD using a closure method [7], showed that a cascade of current to small wavelengths is to be expected, with singularities formed within a finite time from smooth initial conditions. Since strongly intermittent magnetic were first observed in the solar atmosphere [8], much evidence of intermittent, filamentary plasma structures has been found in many astrophysical plasmas [9, 10, 11]. Laboratory plasmas have also displayed key features indicating intermittency [12], as have numerical simulations. Two-dimensional spectral fluid simulations at increasingly high resolution [13, 14, 15] have shown strongly peaked structures in both

current and vorticity. Our own simulations indicate this as well. Figure 1.1 shows results from a simulation of the coalescence instability [16] with a three-dimensional magneto-inductive particle code [17]. The contours show surfaces of constant axial current. An explosive collapse breaks the pair of current columns into many smaller columns.

The purpose of this work is to describe a turbulent MHD model that has singular structures as its fundamental objects. Chapter 2 contains a review of work done previously for two-dimensional neutral fluid turbulence, in both the Fourier and point vortex discretizations. Chapter 3 studies filamentary currents in a steady-state tokamak, using statistical arguments and numerical simulations to obtain information on the interior magnetic surfaces. Chapter 4 introduces a general formalism for fitting MHD into a discrete vortex formalism in two dimensions, and chapter 5 describes computer simulations of such vortex systems. Chapter 6 extends the MHD vortex model to three dimensions, with accompanying analysis and simulation results, and chapter 7 gives an overview of the results and their implications.

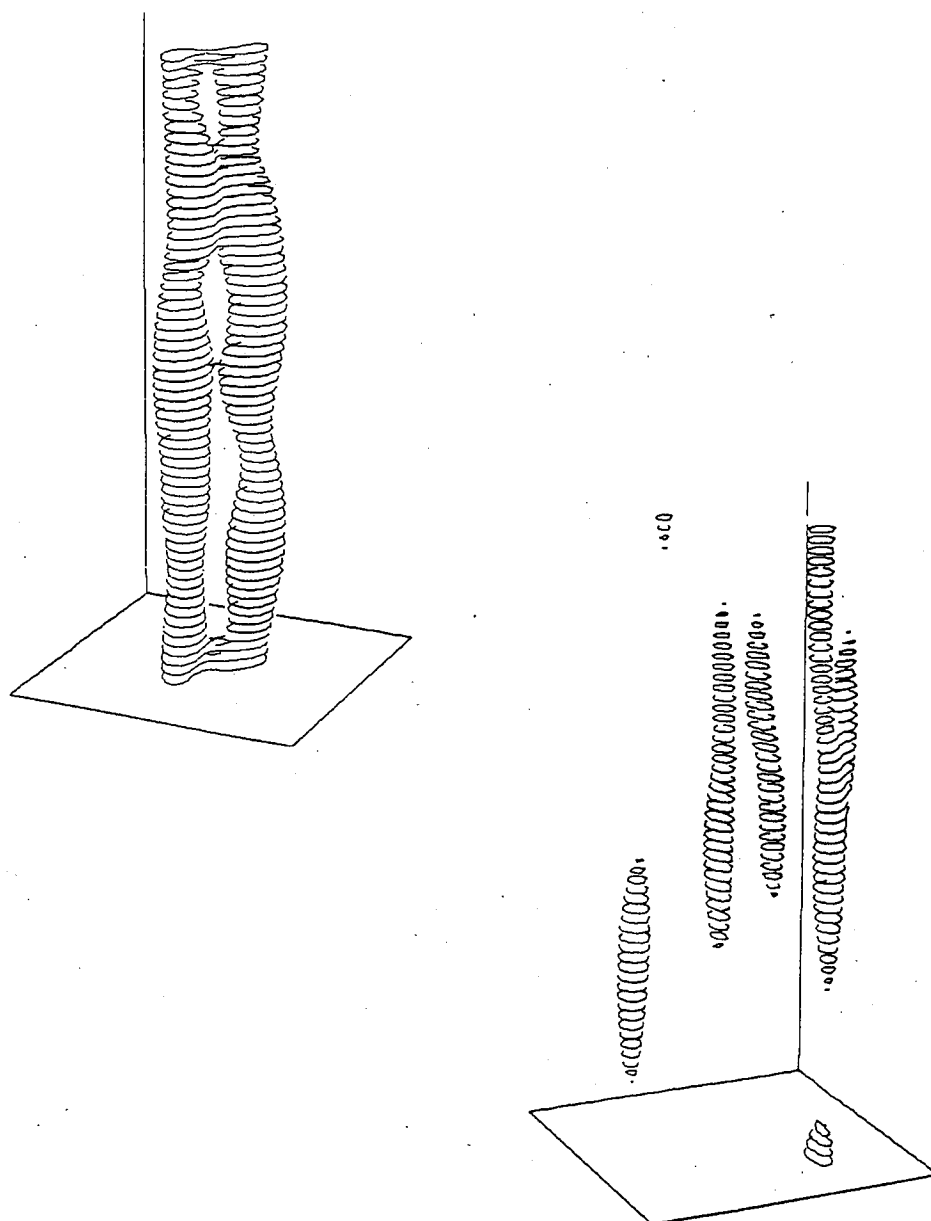


Figure 1.1: Current columns from a 3-dimensional particle simulation of the coalescence instability. Two columns with parallel currents are attracted, meet explosively, and break up into many smaller currents in (b).

Chapter 2

Self-Organization and Structures in Neutral Fluids

Given the unpredictable, chaotic behavior of fluids at high Reynolds numbers, a statistical approach to describing turbulence seems very natural. Beginning with Onsager's 1949 paper [18], authors have found no shortage of interesting statistical properties of turbulent neutral fluids, especially in two dimensions. A simple first approach of taking a Gibbs ensemble based on the kinetic energy of the system leads to a simple result: the energy is partitioned equally among Fourier modes. No structure is present, no phase transitions. However, a proper construction of a Gibbs canonical ensemble must take account of all additive invariants of a system, and there is another for two-dimensional hydrodynamics: the enstrophy, or mean squared vorticity, which completely changes the character of the Fourier analysis results. Reviews are available in the literature [19, 20]. This chapter gives an outline of the results of decades of investigation into two-dimensional turbulence as it relates to the present parallel attempts for magnetohydrodynamics.

2.1 Basic Hydrodynamical Equations

Throughout this dissertation, the velocity field will be assumed to incompressible, and the effects of viscosity will be neglected. The fluid motion is described

by the Navier-Stokes equation,

$$\partial_t \mathbf{v} + \mathbf{v} \cdot \nabla \mathbf{v} + \nabla p / \rho = 0, \quad (2.1)$$

with

$$\nabla \cdot \mathbf{v} = 0. \quad (2.2)$$

These two equations (actually four) are to be solved for the vector velocity field $\mathbf{v}(\mathbf{x}, t)$ and the pressure field $p(\mathbf{x}, t)$. If the mass density $\rho(\mathbf{x}, t)$ is not constant, an equation of state must also be specified. We will take ρ to be a constant, and furthermore, choose units in which $\rho = 1$. For convenience we define the vorticity $\boldsymbol{\omega} = \nabla \times \mathbf{v}$ and separate equations for \mathbf{v} and p by taking the curl and the divergence of eq. (2.1), giving

$$\partial_t \boldsymbol{\omega} + \nabla \times (\mathbf{v} \times \boldsymbol{\omega}) = 0 \quad (2.3)$$

and

$$\nabla^2 p + \nabla \cdot (\mathbf{v} \cdot \nabla \mathbf{v}) = 0. \quad (2.4)$$

Since most of the interesting information of the system is contained in the velocity field, we concentrate on solving eq. (2.3), knowing that the pressure is obtainable from (2.4) once (2.3) has been solved.

The Navier-Stokes equation has a number of dynamic invariants. If one chooses a closed loop which moves with the fluid, then the integral around any such loop $\oint \mathbf{v} \cdot d\mathbf{l}$ is a constant. These invariants do not survive when the continuous system is truncated into a discrete form. Invariants which do survive are the linear invariants of total momentum and vorticity:

$$\begin{aligned} \int \mathbf{v} d\mathbf{x} &= \text{const.} \\ \int \boldsymbol{\omega} d\mathbf{x} &= \text{const.}, \end{aligned} \quad (2.5)$$

which serve only to locate the origin of phase space, and the quadratic invariants of total energy and helicity:

$$\begin{aligned}\frac{1}{2} \int v^2 d\mathbf{x} &= \text{const.} \\ \int \mathbf{v} \cdot \boldsymbol{\omega} &= \text{const.},\end{aligned}\tag{2.6}$$

which are the critical invariants for determining statistical behavior.

In two dimensions, $v_z = 0$, $\boldsymbol{\omega} = \omega \hat{\mathbf{z}}$, and we define the stream function Ψ such that $\mathbf{v} = \nabla \times \hat{\mathbf{z}} \Psi$. The vorticity field solves

$$\partial_t \omega + \mathbf{v} \cdot \nabla \omega = 0.\tag{2.7}$$

The helicity is identically zero in two dimensions, but taking its place as a quadratic invariant is the enstrophy,

$$\Omega = \int \omega^2 d\mathbf{x}.\tag{2.8}$$

2.2 Harmonic Analysis

In order to legitimize the use of statistical mechanics, a system must be shown to have a conservative flow in phase space; it must obey Liouville's theorem. Given a system which is described by a set of coordinates $\{q_i\}$, with a probability distribution function $f(q_1(t), \dots)$, the total phase volume occupied by the system is $\int f \prod_i dq_i$. In order for this to be conserved, we must have

$$\frac{d}{dt} \int f \prod_i dq_i = \int f \sum_i -\frac{\partial \dot{q}_i}{\partial q_i} \prod_i dq_i = 0.\tag{2.9}$$

Liouville's theorem,

$$\sum_i \frac{\partial \dot{q}_i}{\partial q_i} = 0,\tag{2.10}$$

is necessary and sufficient for phase volume conservation. A detailed Liouville's theorem results if the equality holds when the sum runs over some subset of the i 's (or even for each individual q_i).

A statistical analysis of a continuous fluid based on the harmonic functions of the field variables is made possible on the basis of the existence of a detailed Liouville theorem, which was first proved for hydrodynamics by Lee [21]. The simpler proof given here is due to Kraichnan [22], who is also responsible for most of the early work in this area [23, 24]. If we introduce orthonormal eigenfunctions of the Laplacian operator,

$$\nabla^2 \phi_n(\mathbf{x}) + k_n^2 \phi_n(\mathbf{x}) = 0, \quad (2.11)$$

and write

$$\omega(\mathbf{x}, t) = \sum_n \omega_n(t) \phi_n(\mathbf{x}) \quad (2.12)$$

with

$$\omega_n(t) = \int \omega(\mathbf{x}, t) \phi_n(\mathbf{x}). \quad (2.13)$$

Then the coefficients ω_n evolve according to

$$\dot{\omega}_n = \sum_{lm} A_{nlm} \omega_l \omega_m \quad (2.14)$$

where the A's are constant coefficients given by

$$\begin{aligned} A_{nlm} &= \int \phi_n \epsilon_{ij} \partial_i \phi_l \partial_j \phi_m \\ A_{nlm} &= -A_{nml} \end{aligned} \quad (2.15)$$

The enstrophy is given by

$$\Omega = \sum_n \omega_n^2, \quad (2.16)$$

while the energy is

$$E = \sum_n k_n^{-2} \omega_n^2. \quad (2.17)$$

The conservation of these quantities implies that

$$\begin{aligned} \sum_{nlm} A_{nlm} \omega_n \omega_l \omega_m &= 0 \\ \sum_{nlm} k_n^{-2} A_{nlm} \omega_n \omega_l \omega_m &= 0 \end{aligned} \quad (2.18)$$

for all possible flows at all times. This can only be true if

$$\begin{aligned} A_{nlm} + A_{lnm} + A_{mln} &= 0 \\ k_n^{-2} A_{nlm} + k_l^{-2} A_{lnm} + k_m^{-2} A_{mln} &= 0, \end{aligned} \quad (2.19)$$

from which we may deduce

$$A_{nnn} = A_{nmn} = A_{nmm} = A_{mnn} = 0, \quad (2.20)$$

and

$$\frac{\partial \dot{\omega}_n}{\partial \omega_n} = 0. \quad (2.21)$$

Eq. (2.21) is our detailed Liouville's theorem. That the relation (2.21) holds for each mode individually is important, for it allows one to truncate the system after a finite number of modes and still enjoy a conservative flow in phase space. The coefficients ω_n are the phase-space coordinates used to describe the state of the turbulent system. In a periodic box, the eigenfunctions ϕ_n are simply $e^{ik \cdot x}$, and the eigenvalues are the wavenumbers.

In a periodic box, there is a minimum wavenumber k_{\min} , but there must be a maximum wavenumber in order to avoid an ultraviolet divergence in the partition function. Restricting therefore the wavenumbers to $k_{\min}^2 < k^2 < k_{\max}^2$, and taking the ω_n 's as phase variables, the partition function is

$$Z = \int \exp(-\beta E - \alpha \Omega) \prod_n d\omega_n. \quad (2.22)$$

The inverse temperatures β , and α are determined uniquely by the mean energy and enstrophy along with the minimum and maximum wave numbers. Using (2.22), the expected mode distributions are:

$$\langle \omega_n^2 \rangle = \frac{k_n^2}{\beta + 2\alpha k_n^2}. \quad (2.23)$$

First, note the importance of including Ω as an invariant. Without it ($\alpha = 0$), the energy is partitioned equally between the modes, β is necessarily positive, and there is no structure in the statistical state.

The addition of the invariant Ω allows for a varied structure in the expected state. The temperatures α and β may be either positive or negative, although the non-negativity of $\langle \omega_n^2 \rangle$ gives the restrictions

$$\begin{aligned} \beta + 2\alpha k_{\min}^2 &> 0 \quad \text{if } \alpha > 0 \\ \beta + 2\alpha k_{\max}^2 &> 0 \quad \text{if } \alpha < 0. \end{aligned} \quad (2.24)$$

There are three regimes for the temperatures. One in which both α and β are positive, and two regimes in which either α or β is positive and the other is negative. Typical expected spectra for the three regimes are shown in figure 2.1. When $\alpha > 0$ and $\beta < 0$, k_{\min} is exaggerated above the other modes, organizing the vorticity into large-scale structures. When $\alpha > 0$ and $\beta > 0$, the k_{\min} mode is suppressed. With k_{\max} fixed, as α shrinks in magnitude, the expected energy rises, and the $\beta > 0$ spectrum begins to grow $\propto k^2$, until α drops below 0, and the k_{\max} mode is exaggerated. Practically, though, k_{\min} is restricted by the size of the periodic system, whereas k_{\max} is an arbitrary limit and may be taken as large as desired for any given system. Consequently, k_{\max} the $\alpha < 0$ states are difficult to obtain due to the limitations of eq. (2.24), and are not expected to appear in real systems.

2.3 Point-Vortex Representation

Another possible representation of a general turbulent fluid is as a system of point vortices. The total velocity field is expressed simply as a sum of divergence-free fields from individual vortex filaments. A single vortex filament with a strength α produces a velocity field at \mathbf{r} of

$$v_x = -\alpha \frac{y}{r} \quad v_y = \alpha \frac{x}{r}. \quad (2.25)$$

In other words, the vorticity field is a sum of delta functions

$$\omega(\mathbf{x}, t) = \sum_i \alpha_i \delta(\mathbf{x} - \mathbf{x}_i(t)). \quad (2.26)$$

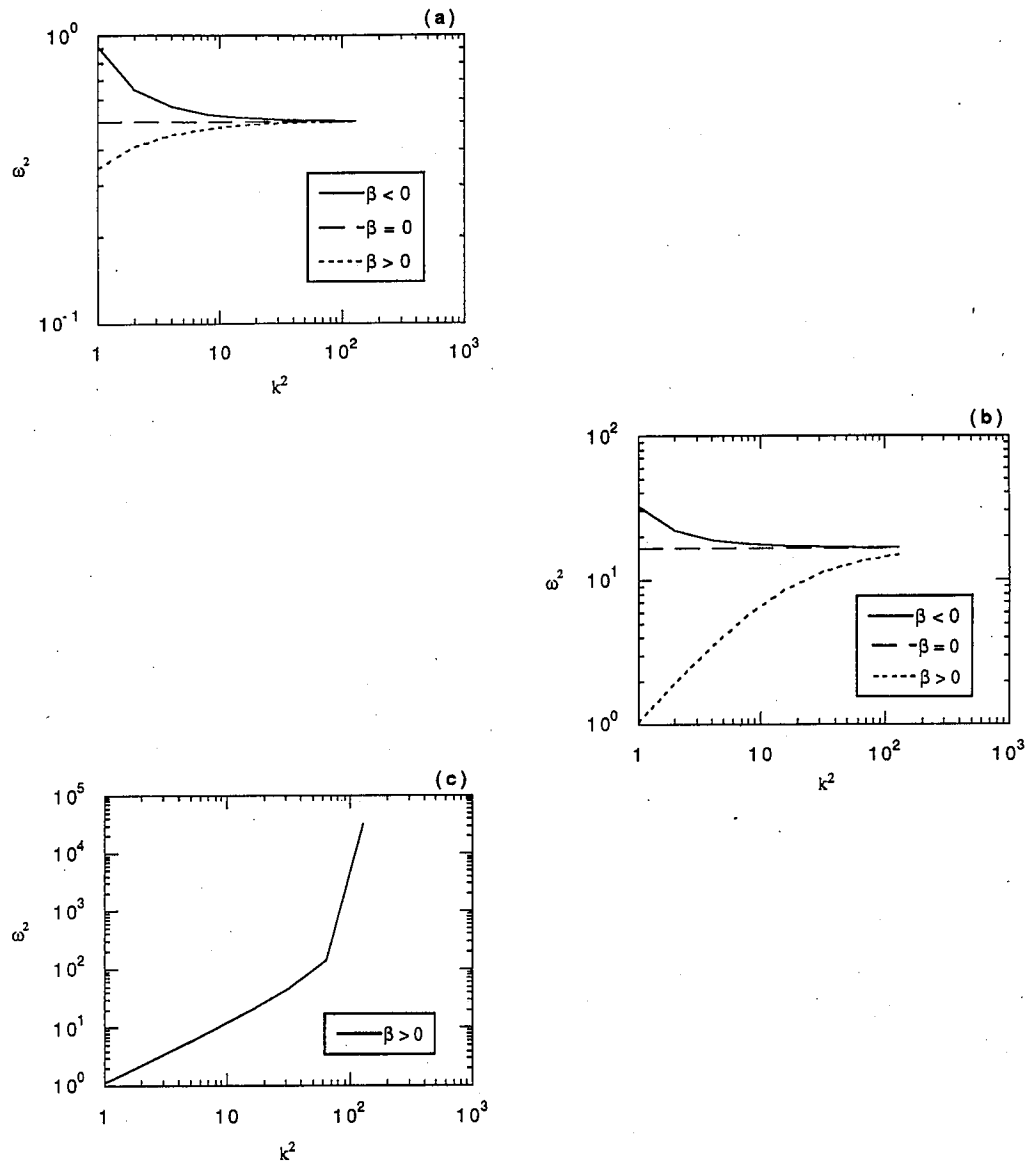


Figure 2.1: Equilibrium spectra for (a) $\alpha \sim 1$ (b) $0 < \alpha \ll 1$, and (c) $\alpha < 0$

The scalar potential, Ψ , is given by

$$\Psi(\mathbf{x}, t) = - \sum_i \alpha_i G(\mathbf{x} | \mathbf{x}_i), \quad (2.27)$$

where G is a Green's function that satisfies

$$\nabla^2 G(\mathbf{x} | \mathbf{x}') = \delta(\mathbf{x} - \mathbf{x}'). \quad (2.28)$$

The total kinetic energy is

$$E = \frac{1}{2} \sum_i \alpha_i \Psi(\mathbf{x}_i) = \frac{1}{2} \sum_{ij} \alpha_i \alpha_j G(\mathbf{x}_i | \mathbf{x}_j), \quad (2.29)$$

which includes a self-energy from each filament. When the boundaries are rigid walls, a filament's self-energy depends on its proximity to the boundary, but with free or periodic boundary conditions, each filament has a constant self-energy, so the total energy may be replaced by the interaction energy, in which the summation includes only terms with $i \neq j$. This is one manifest difference between the vortex and Fourier discretizations. The self-energies of any intermittent structures in a Fourier representation are not subtracted from the energy that appears in the Boltzmann distribution.

Each filament simply moves with the total velocity field at its location. It is easy to see that the equations of motion for the filaments can be written

$$\alpha_i \frac{dx_i}{dt} = - \frac{\partial E}{\partial y_i} \quad \alpha_i \frac{dy_i}{dt} = \frac{\partial E}{\partial x_i}, \quad (2.30)$$

from which it is plain that the interaction energy E is a Hamiltonian for the system. The canonical coordinates are none other than the Cartesian coordinates of the filaments themselves. The detailed Liouville theorem follows directly from the existence of a Hamiltonian.

When Onsager first proposed the idea of a statistical treatment of fluid turbulence, based on a representation in terms of discrete vortices, he was motivated simply by their observed prevalence in experimental (and indeed

everyday) fluids. He made some very simple arguments that extracted intuitively and qualitatively many of the results which would follow later from more detailed mathematical treatments. His argument was that in a fluid with a boundary, or a fluid in a periodic box, the system's phase space is simply the volume of the fluid and hence is finite. The structure function, $\Phi(E)$, the volume of phase space with energy E , is positive everywhere, but must approach 0 as $E \rightarrow \pm\infty$. Therefore, Φ must have a maximum at some finite E_m . The temperature Φ/Φ' must then be negative for $E > E_m$. A negative temperature means that as the system energy increases, the entropy *decreases*. A large positive energy is created when filaments of like sign come close together. Raising the energy while decreasing entropy is accomplished by creating large clusters of like-signed filaments, while the other extreme, large negative energies, are accompanied by an increase in entropy, and so are manifested by large numbers of tightly-bound positive-negative vortex filament pairs.

First descriptions of systems of vortex filaments were characterized by the invocation of a "random-phase approximation," [25, 26, 27] in which a change of variables was made from the coordinates of the filaments, \mathbf{x}_i to the density modes

$$\rho(\mathbf{k}) = \sum_i \alpha_i e^{i\mathbf{k} \cdot \mathbf{x}_i}. \quad (2.31)$$

The idea is that if the particles are distributed randomly, then these modes are simply a sum of random phases. The central limit theorem applies, and the distribution of these modes (which is the Jacobian of the transformation) is simply a Gaussian

$$J \propto e^{-|\rho|^2/a^2}. \quad (2.32)$$

The interaction energy can be expressed as

$$H = \sum_{i < j} \alpha_i \alpha_j G(\mathbf{x}_i | \mathbf{x}_j) = \sum_{\mathbf{k} \neq 0} k^{-2} |\rho(\mathbf{k})|^2 + E_0 \quad (2.33)$$

The constant E_0 may be disregarded for some purposes, but must be carefully evaluated in order to produce a proper thermodynamic limit because of its unusual scaling with the system size. For a system of N filaments of strength α , and N with $-\alpha$, Seyler [28] showed the constant to be

$$E_0 = -2.62N\alpha^2 + N\alpha^2 \ln V. \quad (2.34)$$

Edwards and Taylor [27] used the micro-canonical ensemble, and evaluated the structure function,

$$\Phi = \int \delta(H\{\mathbf{x}_i\} - E) \prod_i d\mathbf{x}_i, \quad (2.35)$$

under the random-phase approximation, using the ρ_n 's as variables, reducing eq. (2.35) to a single-dimensional integral which they evaluated by approximate techniques. The central result was that when the energy climbs above a certain value, the temperature becomes negative, and the amplitude of the lowest wavenumber component of the vorticity begins to climb relative to the rest of the modes. Thus, negative-temperature states are represented by large-scale filament clumping.

A second approach, following initial efforts by Joyce and Montgomery [29], sought a differential equation which was solved by the vorticity in the most probable state. The volume is divided into cells with area Δ_i , and one defines occupation numbers n_i in each cell for each of the two types of filaments: positive and negative. The value of the vorticity at cell i , ω_i , is just $n_i^+ - n_i^-$. Entropy, the logarithm of the probability of obtaining a given set of occupation numbers $\{n_i^\pm\}$ is

$$\sigma = \sum_i n_i^+ \ln \frac{n_i^+}{\Delta_i} + n_i^- \ln \frac{n_i^-}{\Delta_i}. \quad (2.36)$$

The idea of this approach is to maximize the entropy subject to certain constraints. One constraint is that the Hamiltonian remain constant. The Hamiltonian may be expressed in terms of the Green's function matrix G_{ij} between

two cells i and j ,

$$H = \sum_{ij} [n_i^+ n_j^+ + n_i^- n_j^- - n_i^+ n_j^- - n_i^- n_j^+] G_{ij}. \quad (2.37)$$

We introduce a Lagrange multiplier (inverse temperature) for each constraint. For example, if we wish to keep the total number of (positive and negative) filaments constant, we use the multiplier β for the Hamiltonian, and α for the total number of filaments, and maximize $\sigma + \beta H + \alpha N$ under individual variations of the n_i^\pm 's. The requirement that the entropy be stationary leads to the relations

$$\begin{aligned} \ln n^+ + \beta \sum_j G_{ij}(n^+ - n^-) + \alpha &= 0 \\ \ln n^- - \beta \sum_j G_{ij}(n^+ - n^-) + \alpha &= 0. \end{aligned} \quad (2.38)$$

In the limit of small cell size, these occupation numbers revert to the continuous fields, and eq. (2.38) leads to

$$\nabla^2 \Psi = -C^2 \sinh \beta \Psi. \quad (2.39)$$

where C is a constant that is determined by the total number of filaments, and β follows from the Hamiltonian. This result was re-derived by more sophisticated methods from a canonical ensemble [30] as well as for the microcanonical ensemble [31, 32]. The solutions to (2.39) were also calculated in detail in [33]. When $N^+ \neq N^-$ the solutions are unique, given β . They characteristically show a smooth stream function with a single minimum or maximum in the center of the box. When $N^+ = N^-$, there are several branches of solutions, with different values of the temperature for a specified energy. One branch gives a solution similar to the non-neutral case, while other branches give solutions that divide the domain into regions which contain vorticity of one sign or another. A typical high-entropy solution is one which fills the box with a large extended vortex of each sign.

These two methods were shown to be equivalent by Lundgren and Pointin [33], who showed that there were two possible asymptotic scalings of the energy with N . The random-phase approximation was appropriate in the “low-energy” limit, in which the energy scaled as N . In the “high-energy” limit, the energy scales as N^2 , and the vorticity modes can be shown to have non-Gaussian distributions, such that (2.32) is no longer appropriate. They showed that in this limit, with a properly chosen Jacobian, evaluation of the probability density leads to the same results as the entropy-maximizing approach.

2.4 Simulations of Two-Dimensional Turbulence

Recently, experimenters have begun to run laboratory tests of the guiding-center plasma theories [34], but because of the difficulty of realizing two-dimensional systems in a laboratory, the primary test of two-dimensional theories has remained the computer simulation. Early numerical tests of Kraichnan’s Fourier-mode theory [35] consisted of runs on a grid of roughly 16×16 modes. Initial conditions in which the energy was concentrated into a small number of modes evolved into states with spectra that agreed well with Kraichnan’s theory in all three regimes. Other simulations [36, 37] established the mixing properties of the system, and that canonical and micro-canonical ensemble averages yielded nearly the same results. In the negative temperature regime, large-scale vortices were clearly visible from streamline plots of the final states, as predicted by both Fourier and vortex theories.

At the same time, other authors were conducting direct simulations of discrete vortex systems to compare with the vortex theories [29, 30, 27]. Comparison with the theory was not so quantitative as with the truncated Fourier runs, but large-scale clustering of filaments was also clearly observed at energies above the threshold value for negative temperatures. Vortex methods of fluid simulation have continued to be used and developed [57], and are now

being proposed as appropriate models for viscid fluids [43].

Simulations have also been able to provide answers to dynamical questions of spectral transfer and relaxation. As computational capacity increased, simulation grids increased in resolution, to the point that Reynolds numbers 10^4 were able to be simulated on a grid that was sufficiently smaller than the diffusion length scale [4, 38, 39]. McWilliams [4, 40] found that under a broad range of initial conditions, the flow evolved so as to concentrate the vorticity into compact axisymmetric structures, which quickly became the dominant features of the flow. Close encounters between like-signed vortices, which became rarer as the system evolved, would result in the two vortices merging into a single vortex. These vortices have a marked effect on the rates of spectral transfer [6]. The classic Kolmogorov scaling theory of turbulent cascade [41, 42] has as its basis the assumption that phases of different Fourier modes are random and uncorrelated, and that the most important information is contained in the energy spectrum. Flows in which coherent structures dominate clearly violate this assumption, and will require a completely new formalism to describe them, perhaps in terms of a vortex scaling theory [43].

The work of McWilliams was extended and carried out to very long times recently [44]. These runs were carried out to the point at which all vortices of like sign had merged together into just two vortices, one of each sign. What was most remarkable was that the final state was almost perfectly described by a negative β solution of the sinh-Poisson equation, eq. (2.39). The tendency of the fluid to form coherent vortices was so strong that even a spectral simulation code evolved to a state seemingly better described by a discrete vortex model than by a truncated Fourier model.

Chapter 3

Current Filaments in a Tokamak

A two-dimensional system of charged rods that move with the $\mathbf{E} \times \mathbf{B}$ force in a uniform background vertical magnetic field has identical equations of motion to the system of hydrodynamical vortices discussed in the last chapter. For this reason, many of the work on two-dimensional vortices was presented as a theory of a guiding-center plasma. Our interest is to show that this formalism can be applied to more general plasmas as well. The first step is to present a model for a steady-state two-dimensional plasma. Here, it is current filaments within the plasma which form a Hamiltonian system.

The tokamak, as a toroidal plasma containment device, does exhibit evidence of possessing a natural current profile, just as in other devices, such as the reversed field pinch (RFP). This is in spite of the fact that, unlike some fusion devices, the tokamak cannot be said to undergo relaxation. Relaxed profiles for such experiments as RFP's can be obtained by assuming that the plasma is in or undergoes a period of strong turbulence, during which the magnetic field memory is destroyed and energy is dissipated subject to the constraint that the global magnetic helicity remains constant [45]. Thus, a variational principle can predict the relaxed state of the plasma by minimizing the magnetic energy while helicity remains constant. There have also been variational treatments in which complete relaxation of the plasma is not assumed to take place, and the helicity density is conserved [46].

In a tokamak the physical justification for such a method is absent, because such strong turbulence does not occur during the device's normal operation, though such variational calculations have been carried out for the tokamak, and do lead to plausible profiles [47, 48, 49]. Taylor [51] has proposed a physical model of the tokamak interior which can lead to the same current profiles, but without relying on an *ad hoc* variational principle. In this model, which owes much to the "clump" picture of magnetohydrodynamic (MHD) turbulence put forth by Tetreault [52], the tokamak interior is characterized by filamented currents running along stochastic magnetic field lines. The field-line trajectories are determined self-consistently by the self-interactions of the current filaments. This chapter focuses on integrating the current self-interaction together with the external field's action.

3.1 Taylor's Tokamak Interior Model

The fundamental assumption of this model is that the magnetic field is to some degree stochastic. Even though the ideal MHD equations allow for perfect flux surfaces from which a given field line will never deviate, we assert that small-scale turbulent effects neglected in those equations will always cause a field line to wander from any surface. The plasma interior is considered to be filled with ergodic field lines that wander throughout the torus and never close on themselves. Current in the plasma flows along the magnetic field lines.

One may find the toroidal (z) projection of the magnetic field by selecting a set of field lines (each of which carries a current) at a particular cross-section in the plasma, and tracing their progression through an infinite number of revolutions around the torus. Note that because field lines do not close on themselves *individual field line positions are not periodic functions of z* . At the same time, there may be a periodic (possibly uniform) environment set up by the external coils which influences the motion of the filaments. Even

though the overall flux function is periodic, this does not necessarily translate into periodic behavior for each field line, as the total flux is obtained in the limit $z \rightarrow \infty$. Taylor considered only the flux from the internal current filaments, and we will add the effects of an external field in the next section.

In a slow-moving or equilibrium plasma in a tokamak, we consider the combined internal and external toroidal and poloidal magnetic fields to take the form

$$\mathbf{B} = B_0(\hat{z} + \hat{z} \times \nabla \Psi), \quad (3.1)$$

where the poloidal field is related to the toroidal current by

$$\mathbf{J} = J\hat{z} = \nabla \times \mathbf{B} = (\nabla^2 \Psi)\hat{z}, \quad (3.2)$$

and the current and magnetic field satisfy

$$\nabla \times (\mathbf{J} \times \mathbf{B}) = 0. \quad (3.3)$$

Eq (3.3) can be written as

$$\frac{\partial J}{\partial z} + [\Psi, J] = 0, \quad (3.4)$$

where $[\dots]$ indicates the usual Poisson bracket in the poloidal coordinates. From (3.4) it is plain that with z acting as a time-like variable, Ψ acts as a Hamiltonian describing the evolution of the toroidal current. We represent the current as a collection of filaments of strength κ_i :

$$J(\mathbf{r}, z) = \sum_i \kappa_i \delta(\mathbf{r} - \mathbf{r}_i(z)). \quad (3.5)$$

The filaments' positions evolve according the Hamiltonian equations

$$\kappa_i \frac{d\mathbf{r}_i}{dz} = \hat{z} \times \frac{\partial H(\mathbf{r}_1, \dots, \mathbf{r}_N; z)}{\partial \mathbf{r}_i}, \quad (3.6)$$

where $\sqrt{\kappa_i}x_i$ is conjugate to $\sqrt{\kappa_i}y_i$, and the part of the Hamiltonian is played by the flux function Ψ , which will in general have contributions both from the current filaments and from an external field.

This discretization may be looked upon as a representation of the nature of flux found in a real tokamak, but may more generally be considered as a mathematical procedure in which the number of degrees of freedom representing the current field is reduced from the continuum infinity of a field variable to the discrete infinity of a set of filament positions, which may even be represented by a large but finite number of filaments in order to be handled computationally. This most-probable state method was applied to general two-dimensional MHD systems by Montgomery, Turner, and Vahala [53], and later extended by Ambrosiano and Vahala [54] to parameter regimes relevant to both tokamak and RFP devices with good results.

The essential point is the realization that because our system is governed by a Hamiltonian set of equations, conventional statistical mechanics can be used to find reasonable (and physically justifiable) current profiles. The randomization necessary to perform statistical mechanics comes not from strong turbulence in the fluid, which would not be compatible with typical tokamak operations, but from the stochasticity of the magnetic field. Assuming all filaments have equal strength κ , one may define a statistical distribution function of filament positions $\rho(\mathbf{r}_1, \dots, \mathbf{r}_N)$, and calculate the expected current profile $J(\mathbf{r}) = \kappa \langle \rho(\mathbf{r}) \rangle$. A calculation for the most probable state, like that which lead to the "sinh-Poisson" equation 2.39, gives an equation for the most probable current profile,

$$J(\mathbf{r}) = K e^{-\mu \kappa \Psi(\mathbf{r})}, \quad (3.7)$$

which, together with the equilibrium equation (3.2), gives the profile

$$J = \frac{J_0}{(1 + \alpha r^2/a^2)^2}. \quad (3.8)$$

This profile is hardly new, having been derived by variational methods [47, 48, 49], and from Vlasov theory as early as 1934 [50], but the ideas used in arriving at it are different from these previous derivations. The current profile is assumed to be the $z \rightarrow \infty$ limit of the distribution of a collection of z -dependent

current filaments that run along stochastic field lines. This limit is obtained from the ensemble-average of a statistical collection of such filaments, which obey Hamilton's equations. Even though the system is steady-state and hence time-independent, the equations we are solving are dynamical rather than variational in nature. The techniques are the same as used in Ref. [53] and [54], except that our filaments are associated with physical currents (rather than conceptual discretizations of a continuous field), and the invariant "Hamiltonian" arises naturally out of the MHD equations rather than being one of a number of freely-chosen possible invariants.

3.2 Interior Model with External Applied Field

In the previous section, the flux Ψ arose entirely from the field of the current filaments. Now we wish to add the effects of a field from the external coils of the tokamak. This external field will provide a periodic background in which the interior current filaments interact. The structure of the total field is determined by the action of these interacting filaments on top of the basic structure of the imposed field. We assume the following form for the flux-function Hamiltonian:

$$H \equiv \Psi = \sum_i \kappa_i [\Psi_{\text{ext}}(\mathbf{r}_i) + \Psi_{\text{int}}(\mathbf{r}_i)], \quad (3.9)$$

where we write

$$\Psi_{\text{int}}(\mathbf{r}_i) = \sum_{j < i} \kappa_j G(\mathbf{r}_i | \mathbf{r}_j), \quad (3.10)$$

the appropriate flux for a system of parallel currents in two dimensions. G is the Green's function of Poisson's equation appropriate for the chosen boundary conditions (in a boundaryless domain, $G(\mathbf{r}_i | \mathbf{r}_j) = \ln |\mathbf{r}_i - \mathbf{r}_j|$). For our numerical simulations, we choose boundary conditions periodic in x and y . Ψ_{int} represents the mutual interaction of the current-carrying filaments; its Laplacian is the sum of delta functions in eq. (3.5). The first term of (3.9), Ψ_{ext} , is

the external field, and has Laplacian equal to zero. Ψ_{ext} takes the general form

$$\Psi_{\text{ext}}(\mathbf{r}) = \Psi_0(r) + \sum_{m,n} U_{mn}(r) e^{i(m\theta - n\phi)}, \quad (3.11)$$

in which $\phi = z/R$.

Although the analysis in the last section dealt with global profiles, we investigate here only local filament dynamics in the vicinity of a rational surface of the external field, i.e. we restrict Ψ_{ext} to a single helical mode such that

$$U_{mn} = \begin{cases} U_0 = \text{constant} & m = \pm m_0, n = \pm n_0 \\ 0 & \text{otherwise} \end{cases}, \quad (3.12)$$

and expand Ψ_0 to second order around r_0 (where $q(r_0) = m_0/n_0$).

To emphasize the dynamical nature of our equations, we express the filament coordinates as functions of t (defined below) rather than z . We point out again that the filament positions need not be periodic functions of t , but that the external field is periodic in t . The equations (3.6) and (3.11) lead to equations of motion for the current filaments as follows:

With $\phi \equiv \frac{z}{R}$, the field line is described by

$$\frac{dr}{d\phi} = \frac{B_r}{B_0}, \quad \frac{d\theta}{d\phi} = \frac{B_\theta}{rB_0}. \quad (3.13)$$

Define

$$\Phi = \frac{\Psi_{\text{ext}}}{L}, \quad I = \frac{B_0 r^2}{2LR}, \quad (3.14)$$

as normalized external poloidal and toroidal flux. Ψ_{ext} is the external flux of section 3.2, and L is an arbitrary quantity with dimensions of length. The coordinates I and θ obey Hamiltonian's equations with ϕ as the time coordinate:

$$\frac{dI}{d\phi} = \frac{\partial \Phi}{\partial \theta}, \quad \frac{d\theta}{d\phi} = -\frac{\partial \Phi}{\partial I}. \quad (3.15)$$

Let us change coordinates from (I, θ) to (ρ, η) by way of a canonical transformation with the generating function

$$F(\rho, \theta; \phi) = \rho(m_0\theta - n_0\phi) + I_0\theta. \quad (3.16)$$

Our new coordinates are determined by the equations

$$\begin{aligned} I &= \frac{\partial F}{\partial \theta} = m_0 \rho + I_0 \\ \eta &= \frac{\partial \Phi}{\partial \rho} = m_0 \theta - n_0 \phi, \end{aligned} \quad (3.17)$$

while the “Hamiltonian” transforms like

$$\Phi_{\text{new}} = \Phi_{\text{old}} + \frac{\partial F}{\partial \phi}. \quad (3.18)$$

The general form for Φ_{old} is

$$\Phi_{\text{old}} = \Phi_0(r) + \sum_{m,n} U_{mn}(r) e^{i(m\theta - n\phi)}. \quad (3.19)$$

In order that this represent the field from an external current source, the Laplacian of this flux must be zero. Therefore, Φ_0 must be a logarithm, and the U_{mn} ’s are modified Bessel functions. We choose modified Bessel functions of the first kind $U_{mn}(r) = U_0 I_m(nr/R)$, and look at a local region around $I = I_0$ by expanding Φ_0 to second order and letting $U_{mn} = U_0 I_m(nr_0/R)$. The transformed flux, Φ_{new} , looks like

$$\begin{aligned} \Phi_{\text{new}} &\approx \Phi_0(I_0) + m_0 \rho \Phi'_0(I_0) + \frac{1}{2} (m_0 \rho)^2 \Phi''_0(I_0) \\ &\quad + \sum_{m,n} U_{mn} e^{i(m\theta - n\phi)} - n_0 \rho. \end{aligned} \quad (3.20)$$

If we now choose I_0 such that

$$\Phi'(I_0) = \frac{n_0}{m_0}, \quad (3.21)$$

in other words, look at the region where the local $q = m_0/n_0$, then

$$\Phi_{\text{new}} \approx \Phi_0(I_0) + \frac{1}{2} (m_0 \rho)^2 \Phi''_0(I_0) + \sum_{m,n} U_{mn} e^{i(\frac{m}{m_0} \eta - (n - \frac{m}{m_0} n_0) \phi)}. \quad (3.22)$$

Now let us restrict the flux to a single helical mode such that $m = \pm m_0, n = \pm n_0$ (but both having the same sign). In this case, we have

$$\Phi_{\text{new}} \approx \Phi_0(I_0) + \frac{1}{2} (m_0 \rho)^2 \Phi''_0(I_0) U_0 \cos \eta, \quad (3.23)$$

absorbing all constant factors into U_0 . In our helical coordinates, the field-line moves in a way which is not explicitly ϕ -dependent. The field-line equations become

$$\begin{aligned}\frac{d\eta}{d\phi} &= \frac{\partial \Phi_{\text{new}}}{\partial \rho} = \Phi_0''(I_0) m_0^2 \rho \\ \frac{d\rho}{d\phi} &= -\frac{\partial \Phi_{\text{new}}}{\partial \eta} = U_0 \sin \eta,\end{aligned}\tag{3.24}$$

and with the definition

$$U = 2\pi \Phi_0''(I_0) \left(\frac{m_0}{n_0}\right)^2 U_0,\tag{3.25}$$

we obtain the equations of motion for the field lines:

$$\begin{aligned}\frac{dx_i}{dt} &= U \sin(2\pi y_i) \\ &\quad - \sum_{j \neq i} \frac{\kappa_j}{2\pi} \frac{\sigma^2 (y_i - y_j)}{(x_i - x_j)^2 + (y_i - y_j)^2}, \\ \frac{dy_i}{dt} &= x_i \\ &\quad + \sum_{j \neq i} \frac{\kappa_j}{2\pi} \frac{x_i - x_j}{(x_i - x_j)^2 + (y_i - y_j)^2},\end{aligned}\tag{3.26}$$

with

$$\begin{aligned}x &= \frac{\sigma m_0}{2\pi r_0} (r^2 - r_0^2) && \text{a rescaled radial coordinate,} \\ y &= \frac{(m_0 \theta - n_0 \phi)}{2\pi} && \text{a helical angular coordinate,} \\ t &= \frac{n_0 z}{2\pi R} && \text{the time-like toroidal coordinate,} \\ \text{and } \sigma &= \frac{2\pi}{m_0} \left. \frac{d \ln |\frac{1}{q}|}{d \ln r} \right|_{r_0} && \text{proportional to the magnetic shear.}\end{aligned}$$

In the absence of internal current, field lines from the external field move according to the first terms in the right-hand side of eq. (3.26). When field lines are allowed to carry currents of individual strengths κ_i , an additional interaction force must be taken into account, which is represented by the second terms in the right-hand side of (3.26).

3.3 The Standard Map

The portion of the filament motion due to the externally applied current in eq. (3.26) (that is, the first terms of the right-hand side) can be represented in its finite-difference form by the “standard map,” a well-known non-linear map which has been studied both for its own interest and as a model for various physical systems (See, e.g. Ref. [55] and [56]). The toroidal projection of the unperturbed ($\kappa_i = 0$) external magnetic field lines is given by successive iterations of this map, defined by:

$$\begin{aligned} y_{n+1} &= y_n + x_n \\ x_{n+1} &= x_n + U \sin(2\pi y_{n+1}) \end{aligned} \quad (3.27)$$

The map is characterized by stable orbits surrounded by stochastic regions, the areas of which increase with the parameter U . For a critical value of U near 0.1546, the stochastic regions of adjacent orbits overlap, and trajectories diffuse throughout the region without limit. For $U < U_{\text{crit}}$ trajectories stay confined within one particular orbit. Thus, a weak external field will produce magnetic surfaces that are distinct and separate, with individual field lines confined to roughly concentric tori. Under a stronger applied field, surfaces will overlap and the volume will approach one large stochastic region, with a single field line wandering ergodically throughout the region. Figure 3.1 shows stochastic regions for $U < U_{\text{crit}}$ and $U > U_{\text{crit}}$.

Another feature of the standard map are the “accelerator modes” [56]. These modes are present only for particular values of $U \gg U_{\text{crit}}$ such that when U takes on one of these (near-integral) values, there exist particular regions of phase space in which a trajectory may become greatly accelerated in x . The displacement of trajectories in this region grows faster than linearly with time (whereas over most of the phase space, diffusion is linear), although they eventually diffuse out of the accelerating region altogether, to diffuse at the normal rate.

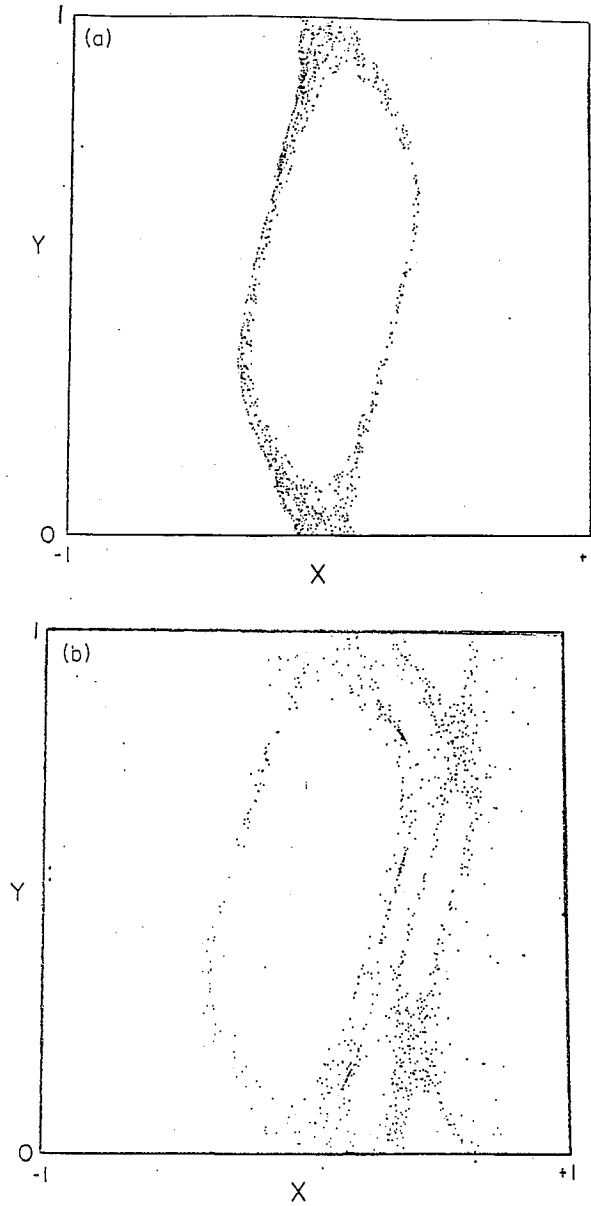


Figure 3.1: Phase-space plot (x_n, y_n) for 25,000 iterations of the standard map beginning at a point near the X-point, $(0,0)$. Plot shows stochastic region of the standard map for (a) $U = 0.15 < U_{\text{crit}}$ and (b) $U = 0.20 > U_{\text{crit}}$.

3.4 Computational model

The interaction term of (3.26) also takes a well-known form. Hydrodynamical vortices [57] and two-dimensional guiding-center plasmas [58] (in which particles move exclusively under the $\mathbf{E} \times \mathbf{B}$ force) both have equations of motion identical to ours, apart from scaling factors. We simulate this system with a two-dimensional electrostatic particle-in-cell technique. The code accumulates the filament density onto a grid from the filament positions. From this filament density, it calculates the electric potential Ψ_{int} and field in Fourier space via Poisson's equation, eq. (3.2). The field is then interpolated back to the filaments' positions to advance them forward in time. Calculations are performed for 1024 filaments on a 32×32 grid with periodic boundary conditions. On top of the interaction motion, we impose the action of the standard map. We let these "kicks" from the external field occur every 25 time steps. With the filament interaction strengths set to zero, we have measured the variance of diffusion times with U and obtained agreement with Chirikov's calculations [55]. These are shown in figure 3.2.

The computational grid represents the phase-space region $0 < y < 1$, $-1 < x < 1$, with a magnetic shear value $\sigma = 2$ in eq. (3.26). Filaments are given random strengths between $+\kappa$ and $-\kappa$ with mean zero, and were initially distributed randomly throughout $0 < y < 1$, $-1/2 < x < 1/2$. We calculate the diffusion time by fitting the curve

$$\frac{1}{N} \sum_i |x_i(t) - x_i(0)|^2 = \frac{t}{T_{\text{diff}}}. \quad (3.28)$$

For particularly slow diffusion, T_{diff} was measured by calculating the average time elapsed for a filament to first drift one unit in x from its starting position.

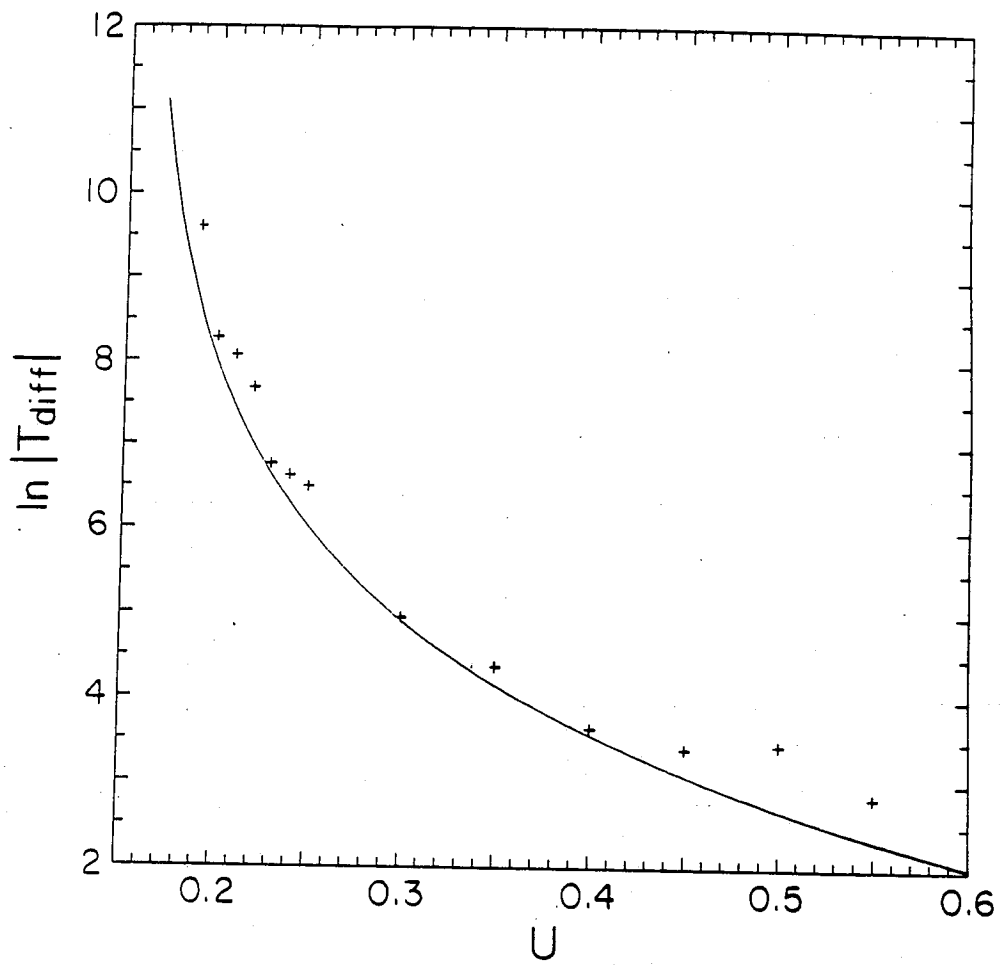


Figure 3.2: Crosses show computed diffusion time, T_{diff} , versus the parameter U for the standard map. The solid line is the fit calculated by Chirikov.

3.5 Results

We are interested in the “time” scale of filament “diffusion.” This determines the degree to which the ideal magnetic surfaces from the external current are maintained under the effects of internal current self-interaction in a tokamak equilibrium. It is important to remember that what we measure is not actually a diffusion time: our “time” is really the toroidal coordinate ϕ . Hence the “diffusion time” is the number of revolutions around the torus that a field line must traverse in order to deviate significantly from its original surface.

The diffusion of field lines is characterized by three regimes. When U is large, the stochasticity of the standard map dominates the diffusion. As $U \rightarrow U_{\text{crit}}$, the background magnetic surfaces become regular and the diffusion is driven by the current interaction. In between is a regime wherein the diffusion rates of the two effects are comparable. Figure 3.3 shows plots of the diffusion vs. time in the three regimes. In the field-dominated regime, the magnetic surfaces overlap, so the filaments wander throughout the region more or less freely. When the rates become comparable, a filament will spend a long time within a particular orbit before diffusing across a boundary, so the diffusion fluctuates around a mean linear growth. Finally, as $U \rightarrow 0$, the closed orbits narrow, and the fluctuations decrease in magnitude until the diffusion becomes smooth in the current-dominated regime. Figure 3.4 shows the dependence of diffusion time on U for different fixed values of the interaction κ . From this, one can see that the transition between the three regimes is smooth: the fluctuations around the mean diffusion appear and disappear without affecting the net diffusion rate.

Figure 3.5 shows the dependence of diffusion time on κ . In the absence of a background field, the current-dominated diffusion goes as $\sim \kappa^{-2}$. As κ grows large, the diffusion conforms to this law regardless of U . A qualitative look at this figure reveals that this regime sets in at around $\ln |\kappa| \approx -4.5$.

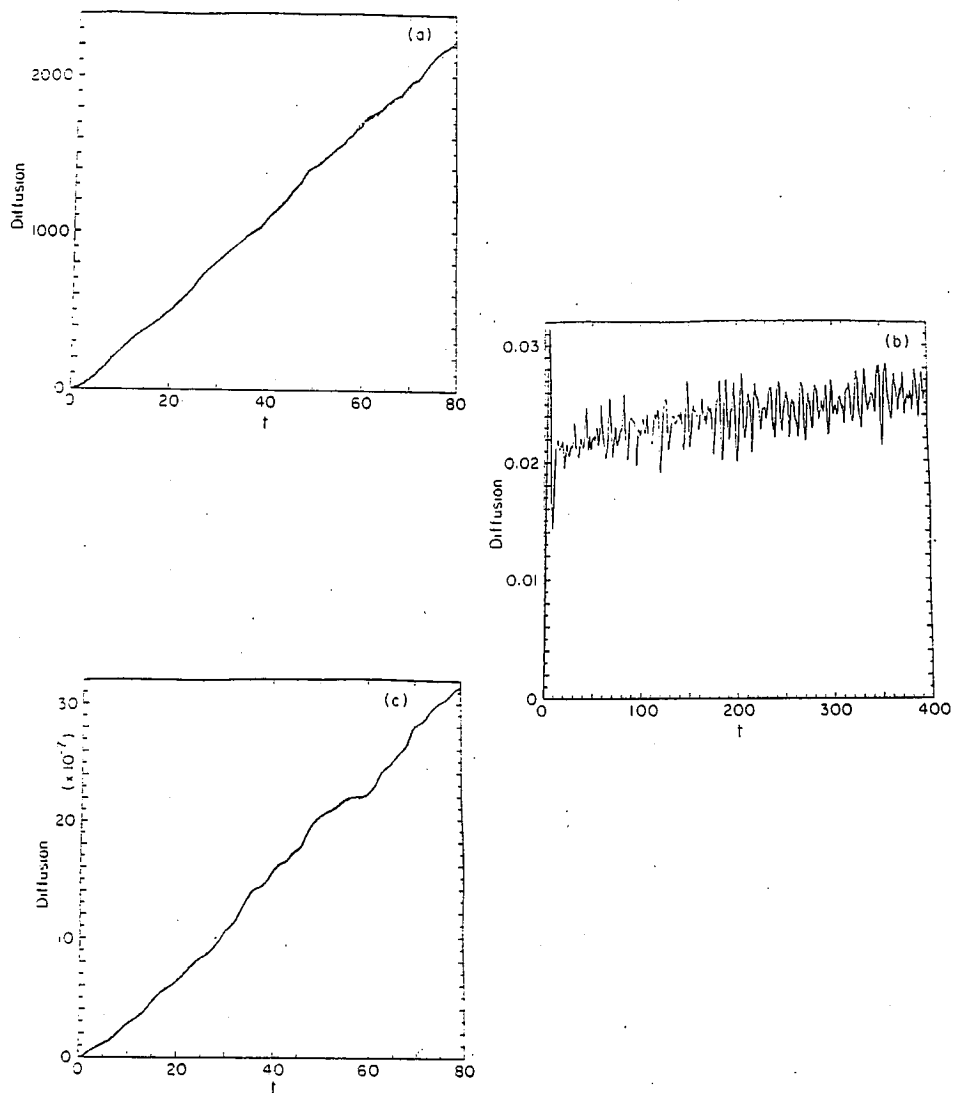


Figure 3.3: Plots of mean square diffusion, $\frac{1}{N} \sum_i |x_i(t) - x_i(0)|^2$, vs. time for $\kappa = 10^{-4}$. (a) field-dominated regime $U = 2.0$. (b) transition regime $U = 0.15$, (c) current-dominated regime $U = 0$.

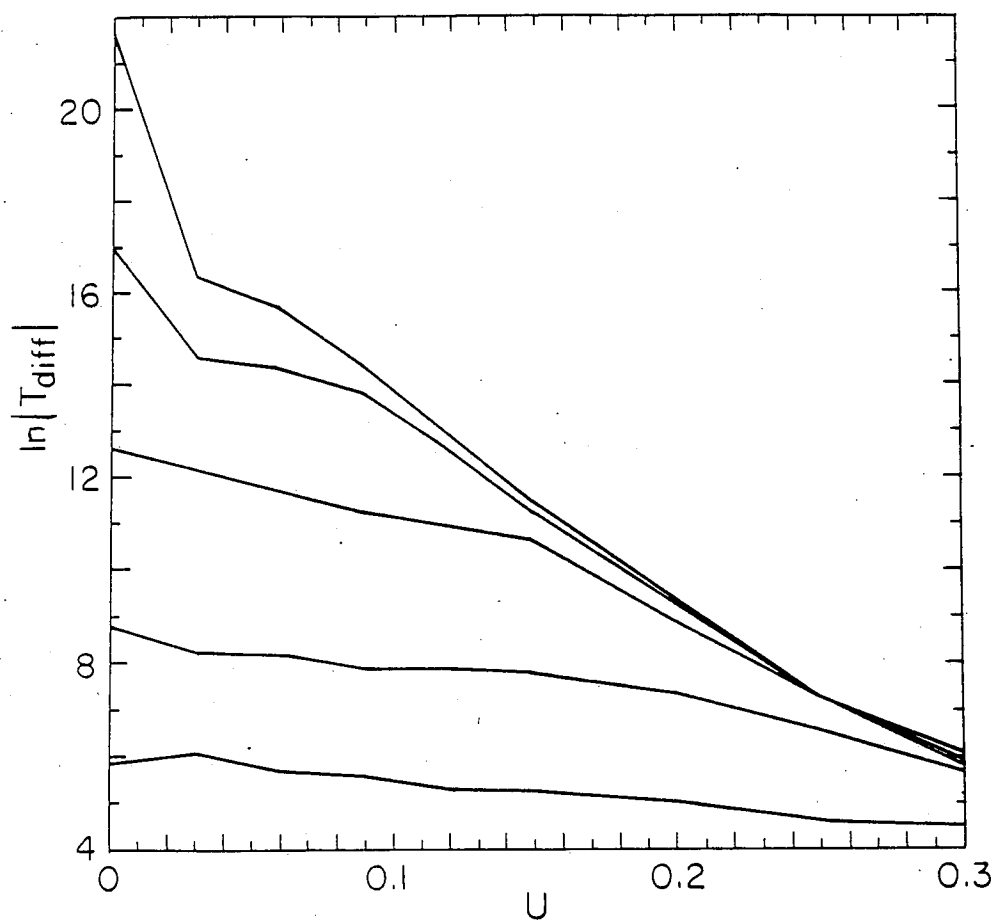


Figure 3.4: T_{diff} , vs. U for $\kappa = 0.05, 0.01, 10^{-3}, 10^{-4}$, and 10^{-5} .

When $U > U_{\text{crit}}$ the curve will flatten out as $\kappa \rightarrow 0$ (*'s in figure), making diffusion independent of κ and representing the field-dominated regime. Note that this regime does not exist for $U < U_{\text{crit}}$, as the diffusion time will increase without bound as $\kappa \rightarrow 0$, the rate of this increase growing inversely with U .

One possible anticipated effect of filament interaction was that a filament would be jostled out of an orbit's stochastic region and into a more tightly bound region, thus possibly slowing the diffusive process. This was indicated in some simulations involving only two filaments [59] but in none of our simulations was this observed. Without exception, diffusion of magnetic surfaces was enhanced by filament self-interaction. This effect may yet be observed with a smaller number of filaments in the system, but we expect that for a realistic model of a tokamak interior, a large number of filaments must be maintained, and the anticipated diffusion inhibition would not appear in experiments.

The presence of accelerator modes of the standard map continued to be observable for small values of κ . Figure 3.6 shows the presence of accelerator modes in our model. They are represented by dips in the diffusion time at $U \approx 1.1, 2.2$, and 3.2 , where the presence of these modes increases the general rate of diffusion. The effects of these modes can be seen for values of κ up to about the order of U_{crit} , after which the effect becomes indiscernible.

We find the effect of the interaction of local current deviations to be pronounced. When the interaction reaches a strength $\kappa \sim U_{\text{crit}}$, the accelerator modes cease to become noticeable. The parameter regime for which the field is stochastic ranges over all values of U , whereas for the unperturbed case, the field is stochastic only for $U > U_{\text{crit}}$. In the "field-dominated" regime, the stochasticity is due to the normal overlapping of magnetic islands, but even as the magnetic surfaces become regular, the plasma becomes "current-dominated" and the field remains stochastic due to filament interactions. The onset of this regime is at κ near 0.011 for U near the critical value 0.155.

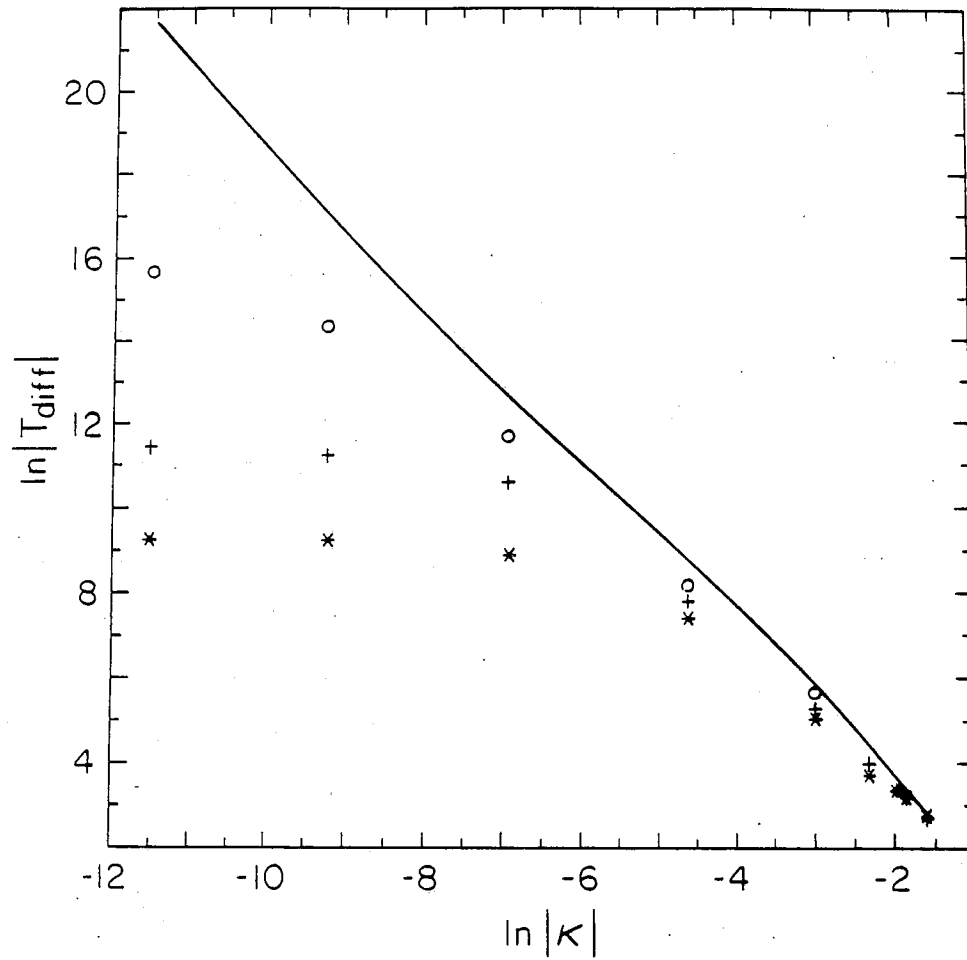


Figure 3.5: Log-log plot of T_{diff} vs. κ . The solid line represents the data from $U = 0$. The o's are from $U = 0.06$, the + 's from $U = 0.15$, and the * 's from $U = 0.20$.

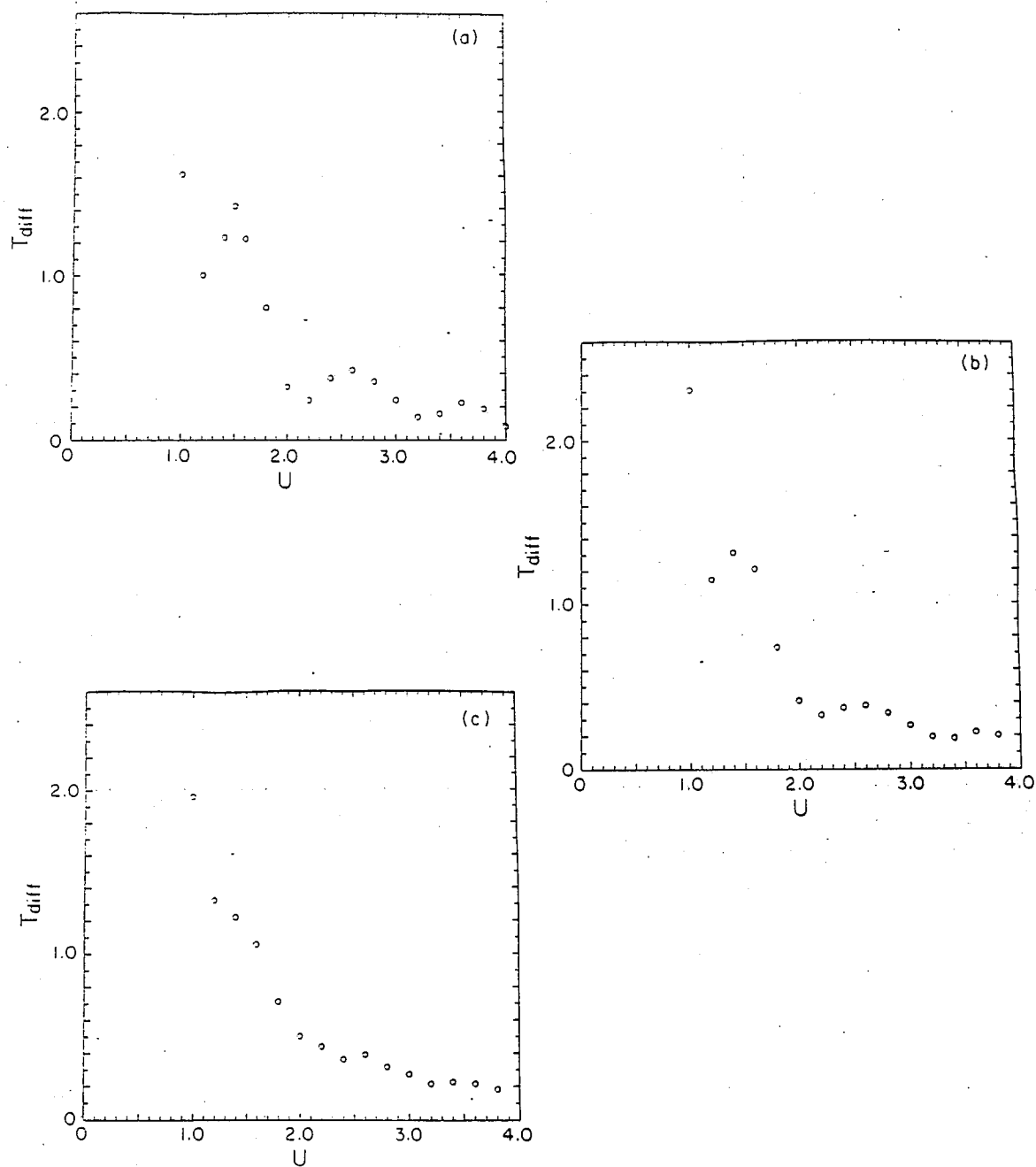


Figure 3.6: T_{diff} vs. U in the accelerator mode regime. (a) in the absence of self-interaction, $\kappa = 0.0$. (b) for $\kappa = 0.1$. The effect is diminished but still noticeable. (c) for $\kappa = 0.2$ the modes are all but gone.

Chapter 4

Theory of Two-Dimensional MHD Filaments

We wish to show that a point-vortex discretization like that of hydrodynamics is also possible for more general MHD, first in two dimensions, and in chapter 6, in three dimensions. This approach has motivations that are theoretical, observational, and computational. Briefly, we expect that a plasma description in which intermittency is inherent is desirable for the same reasons that discrete vortex models of hydrodynamics have been successful [19]. Because of the demonstrated lack of general equivalence between different discretizations of functional integrals [2], such a model may differ significantly from Fourier-based statistical theories. Observations of plasmas in the sun [8] and in laboratories [12] that reveal strong intermittencies, as well as numerical simulations [15] argue in favor of a model based on intermittent structures, and computational algorithms can benefit similarly by the efficiency with which point-vortex codes [57] can model high Reynolds-number fluids.

4.1 MHD Harmonic analysis

Fyfe, Joyce, and Montgomery [60] have presented a Fourier-mode-based statistical theory of 2-d MHD like that of Kraichnan's for hydrodynamics, showing that the Fourier components of the vorticity and current can be shown to obey Louisville's theorem as well [60]. In this case, there are three quadratic constants of the motion which survive the truncation of modes $k_{\min}^2 < k^2 < k_{\max}^2$

They are the total energy, the cross helicity, and the mean square potential,

$$\begin{aligned}
 E &= \frac{1}{2} \int (\mathbf{v}^2 + B^2) = \frac{1}{2} \sum_k \frac{1}{k^2} (|\omega(\mathbf{k})|^2 + |j(\mathbf{k})|^2) \\
 P &= \frac{1}{2} \int \mathbf{v} \cdot \mathbf{B} = \frac{1}{2} \sum_k \frac{1}{k^2} \omega(\mathbf{k}) j(-\mathbf{k}) \\
 A &= \frac{1}{2} \int A_z^2 = \frac{1}{2} \sum_k \frac{1}{k^4} |j(\mathbf{k})|^2.
 \end{aligned} \tag{4.1}$$

It has not been shown that other such constants do not exist. The construction of the canonical distribution for these constants with the partition function,

$$Z = \int \exp(-\alpha E - \beta P - \gamma A), \tag{4.2}$$

gives a predicted spectral distribution

$$\begin{aligned}
 \langle |j_k|^2 \rangle &= \frac{1}{2} \frac{k^2}{\alpha - \beta^2/4\alpha + \gamma/k^2} \\
 \langle |\omega_k|^2 \rangle &= \frac{k^2}{2} \left(\frac{1}{\alpha} + \frac{\beta^2/4\alpha^2}{\alpha - \beta^2/4\alpha + \gamma/k^2} \right).
 \end{aligned} \tag{4.3}$$

In the particular case in which $\langle \mathbf{v} \cdot \mathbf{B} \rangle = 0$, β is zero, and the spectra for \mathbf{v} and \mathbf{B} are

$$\begin{aligned}
 \langle |j_k|^2 \rangle &= \frac{k^2}{\alpha + \gamma k^{-2}} \\
 \langle |\omega_k|^2 \rangle &= \frac{k^2}{\alpha}.
 \end{aligned} \tag{4.4}$$

Compare these expected spectra with eq. (2.23). Regardless of the values of the parameters for the MHD system, the kinetic energy is partitioned equally between the modes. The ω^2 spectrum is the same as if one had ignored the effects of enstrophy in the derivation of (2.23). Indeed one has ignored these effects, as enstrophy is not an invariant of MHD. Still, as the magnetic field vanishes, the rate of change of the enstrophy slows to zero, so one would like to have a theory in which the MHD predictions include a neutral fluid's expected states as a subset.

Next, look at the behavior of the current spectrum in (4.4). The inverse temperature α must be positive, but γ can either positive or negative, subject to the constraints

$$\begin{aligned}\alpha + \gamma k_{\max}^2 &> 0 \text{ if } \gamma > 0, \\ \alpha + \gamma k_{\min}^2 &> 0 \text{ if } \gamma < 0.\end{aligned}\tag{4.5}$$

Plots of $\langle |j|^2 \rangle$ for three values of γ are shown in figure 4.1. The analogy with the formation of large vortices in hydrodynamical turbulence is overwhelming. The crucial parameter in determining whether magnetic islands will emerge is the relative sign of γ and α . In terms of physical quantities,

$$\sum_k \langle |v|^2 \rangle - \sum_k \langle |B|^2 \rangle = 2A \frac{\gamma}{\alpha},\tag{4.6}$$

indicating that whenever the magnetic field energy dominates the kinetic energy, the current will organize into two oppositely-signed current distributions. It is with the motivation of adopting a description that recognizes the apparent symmetry between the velocity and the magnetic fields and of a system which reproduces neutral fluid results in the appropriate limit that we present the point-vortex representation of magnetohydrodynamics.

4.2 Filamentary Equations of Motion

Long ago, Elsasser [61] pointed out that the basic equations of ideal MHD

$$\begin{aligned}\frac{\partial \mathbf{v}}{\partial t} + (\mathbf{v} \cdot \nabla) \mathbf{v} &= -\frac{\nabla p}{\rho} + \frac{(\nabla \times \mathbf{B}) \times \mathbf{B}}{4\pi\rho} \\ \frac{\partial \mathbf{B}}{\partial t} &= \nabla \times (\mathbf{v} \times \mathbf{B}) \\ \nabla \cdot \mathbf{v} = \nabla \cdot \mathbf{B} &= 0,\end{aligned}\tag{4.7}$$

can be written in the form

$$\frac{\partial \mathbf{u}}{\partial t} + (\mathbf{w} \cdot \nabla) \mathbf{u} = -\nabla \eta$$

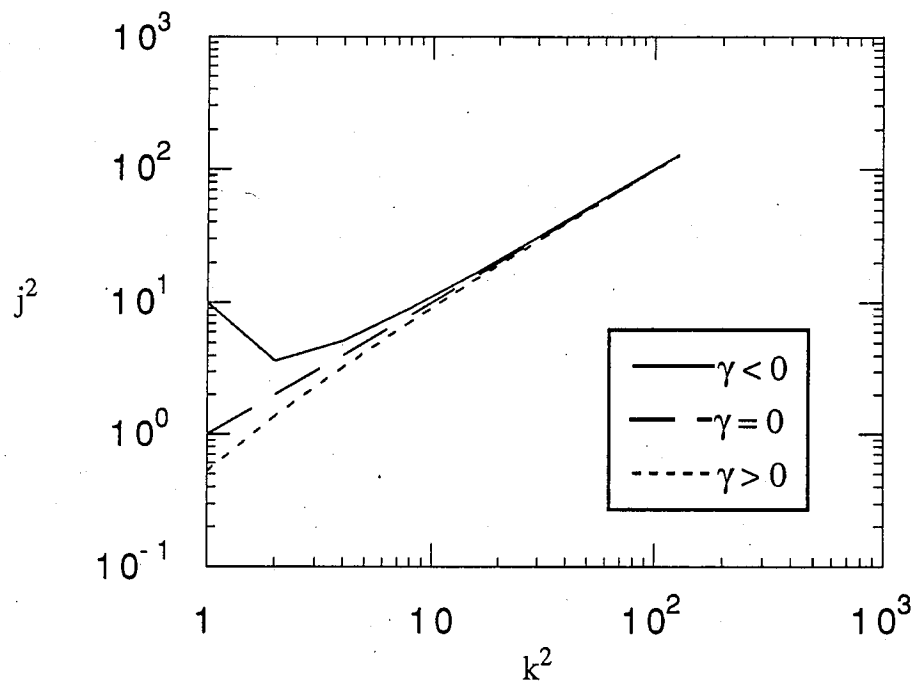


Figure 4.1: Magnetic spectra of Fyfe et. al., showing large-scale magnetic island in the negative temperature regime.

$$\begin{aligned}\frac{\partial \mathbf{w}}{\partial t} + (\mathbf{u} \cdot \nabla) \mathbf{w} &= -\nabla \eta \\ \nabla \cdot \mathbf{u} &= \nabla \cdot \mathbf{w} = 0,\end{aligned}\tag{4.8}$$

where the new variables are

$$\mathbf{u} = \mathbf{v} + \mathbf{B}, \quad \mathbf{w} = \mathbf{v} - \mathbf{B} \tag{4.9}$$

$$\eta = \frac{p}{\rho} + B^2. \tag{4.10}$$

Velocities are measured in units of an arbitrary constant v_0 , and the magnetic field is measured in units of $B_0 = \sqrt{4\pi\rho v_0^2}$.

Let us also define functions Ω and A by

$$\begin{aligned}\Omega^u &= \nabla \times \mathbf{u}, \quad \mathbf{u} = \nabla \times A^u \\ \Omega^w &= \nabla \times \mathbf{w}, \quad \mathbf{w} = \nabla \times A^w.\end{aligned}\tag{4.11}$$

We will use a general species superscript s to indicate one of either u or w , or omit any superscript to generically indicate both possibilities.

In a neutral fluid, the vorticity is conservatively advected through the fluid. We seek an analogous result for our Ω 's. Defining the total advective derivative operators

$$\begin{aligned}D^u V &\equiv \partial_t V - \nabla \times (\mathbf{u} \times V) \\ D^w V &\equiv \partial_t V - \nabla \times (\mathbf{w} \times V)\end{aligned}\tag{4.12}$$

one finds that the curl of the momentum equation becomes

$$D^w \Omega^u + D^u \Omega^w = 0, \tag{4.13}$$

while the induction equation may be written

$$D^w \Omega^u - D^u \Omega^w = 2S, \tag{4.14}$$

in which there is a source term

$$\begin{aligned}
 S = & \Omega^w \times \Omega^u \\
 & + [\Omega^w \cdot \nabla \mathbf{u} - \Omega^u \cdot \nabla \mathbf{w}] \\
 & + \frac{1}{2} [\nabla^2 (\mathbf{u} \times \mathbf{w}) - (\nabla^2 \mathbf{u}) \times \mathbf{w} - \mathbf{u} \times (\nabla^2 \mathbf{w})]. \quad (4.15)
 \end{aligned}$$

In two dimensions, $\Omega = \Omega \hat{z}$ and $\mathbf{A} = A \hat{z}$, and most of the terms in S vanish identically. What remains can be written

$$S = S \hat{z} = [\partial_i A^u, \partial_i A^w] \hat{z}, \quad (4.16)$$

where $[\dots]$ indicates the Poisson bracket in two dimensions. Let Ω take the form

$$\Omega^s = \sum_{i \in s} \alpha_i^s \delta(\mathbf{x} - \mathbf{x}_i^s). \quad (4.17)$$

Eqs. (4.13) and (4.14) are approximately solved by the motion of the filaments if

$$\begin{aligned}
 \frac{d\mathbf{x}_i^u}{dt} &= \mathbf{w}(\mathbf{x}_i^u) \quad , \quad \frac{d\alpha_i^u}{dt} = S(\mathbf{x}_i^u)/n^u(\mathbf{x}_i^u) \\
 \frac{d\mathbf{x}_i^w}{dt} &= \mathbf{u}(\mathbf{x}_i^w) \quad , \quad \frac{d\alpha_i^w}{dt} = -S(\mathbf{x}_i^w)/n^w(\mathbf{x}_i^w), \quad (4.18)
 \end{aligned}$$

where n^s is the local number density of filaments. This solution is not a "weak" solution of the MHD equations in the same sense that the point-vortex evolution in hydrodynamics is a solution of the Euler equations. The validity of eq. (4.18) relies on the number density of filaments of each species being large. The induction of current represented by the source term is manifested by a simultaneous increase in the strength of u -filaments and a decrease in the strength of w -filaments.

A fair question at this point is why to bother with the Elsasser variables at all. The MHD equations could equally well be written in terms of ω and j with their own source terms, but there are several reasons why the Elsasser

variables are a better choice for our purposes. The inherent symmetry in eq. (4.18), makes analytical study that much easier. In addition, there is real observational evidence that plasmas often find themselves in states such that $\mathbf{v} = \pm \mathbf{B}$ (in the solar wind, for example [62]), and the use of u and w gives the source term the desirable property of being small for an intermittent plasma.

Of importance in eq. (4.14) is the fact that S contains *no derivatives* of Ω , whereas $D\Omega$ contains first-order derivatives of Ω in both space and time. Thus, if we are interested in tracking the motion of filaments, and we assume that in the vicinity of a filament, Ω is much more sharply peaked than u or w , we may write

$$\epsilon \equiv \frac{|\nabla w|/|w|}{|\nabla \Omega^u|/|\Omega|} \ll 1, \quad (4.19)$$

and note that S is smaller by a factor ϵ than the convective terms $D\Omega$. This amounts to saying that the filaments should change strength only slowly compared to their convective motion. The benefit of choosing the Elsasser variables is that a filament of simply current or vorticity alone will not last long, but if current and vorticity filaments are correlated so as to form u or w filaments, these structures will persist due to the relative smallness of S .

This is our filamentary representation of 2-d MHD. Unlike hydrodynamics, in which the vorticity field is exactly convected by the velocity field, so that each filament simply moves in the total velocity field, the filaments of a highly intermittent two-dimensional plasma fall into two species. The u -filaments move in the field of the w 's, and the w -filaments move in the field of the u 's.

4.3 Fixed-Strength Filaments

This section deals with the statistics of u - w filaments for which the source S is neglected. In this case, individual filament strengths do not change in time. Let us have N total filaments, N_u of type u and N_w of type w . in which the

u 's have strength $\pm\alpha^u$ and w 's $\pm\alpha^w$. The potentials are given by

$$A^s(\mathbf{x}) = - \int G(\mathbf{x}|\mathbf{x}') \Omega^s(\mathbf{x}') d\mathbf{x}' = - \sum_{i \in s} \alpha^s G(\mathbf{x}|\mathbf{x}_i^s), \quad (4.20)$$

where G is the Green's function for Poisson's equation, $\nabla^2 G = \delta(\mathbf{x} - \mathbf{x}')$, with appropriate boundary conditions. In an infinite domain, $G(\mathbf{x}|\mathbf{x}') \propto \ln |\mathbf{x} - \mathbf{x}'|$.

The filaments move by

$$\begin{aligned} \frac{d\mathbf{x}_i^u}{dt} &= \mathbf{w}(\mathbf{x}_i^u) = \nabla \times \hat{\mathbf{z}} A^w(\mathbf{x}_i^u) \\ \frac{d\mathbf{x}_i^w}{dt} &= \mathbf{u}(\mathbf{x}_i^w) = \nabla \times \hat{\mathbf{z}} A^u(\mathbf{x}_i^w), \end{aligned} \quad (4.21)$$

so this system of filaments is Hamiltonian with the canonically conjugate variables $(\sqrt{|\alpha|}x_i, \sqrt{|\alpha|}y_i)$. The (x, y) are the normal Cartesian coordinates, which we take to be periodic. The Hamiltonian is

$$H(\mathbf{x}_1, \dots, \mathbf{x}_N) = \sum_{i \in u} \sum_{j \in w} \alpha_i^u \alpha_j^w G(\mathbf{x}_i|\mathbf{x}_j), \quad (4.22)$$

which may also be written

$$H = \int A^u \Omega^w = \int \mathbf{u} \cdot \mathbf{w} = \int v^2 - B^2. \quad (4.23)$$

The Hamiltonian is the very same quantity as the parameter in eq. (4.6) which determines the qualitative behavior of the magnetic field in the Fourier description. The fact that we have retained this key parameter as our Hamiltonian is an encouraging justification for omitting S .

The self-energy of a singular vortex filament is infinite. The interaction energy of a such a structure in an external field, however, is well-defined. The potential energy of a given vorticity distribution ω in a velocity field that arises from a vector potential \mathbf{A} is given by

$$E_{\text{int}}^v = \int \omega \cdot \mathbf{A}^v. \quad (4.24)$$

For a given current distribution in a magnetic potential field, on the other hand, the magnetic interaction energy differs by a sign,

$$E_{\text{int}}^B = - \int \mathbf{J} \cdot \mathbf{A}. \quad (4.25)$$

This is because work must be done against the magneto-inductive force in order to maintain a given current distribution while bringing it in from far away. By ignoring the source term in (4.14), we are slowly transferring energy into and out of the system by counteracting the inductive force along the filament. As a consequence, instead of the total magnetic plus kinetic field energy remaining constant, the total interaction energy $\int v^2 - B^2$ is conserved.

In the neutral-fluid vortex model, there is a delicate question of the self-energy of the vortex filaments [28, 30], which must be treated carefully in order to retain correct scaling behavior. In our case, because a single u or w filament has velocity and magnetic fields of equal magnitude. The field of a single filament does not contribute to H , and self-energy considerations do not appear. Rather than an interaction energy, however, it is perhaps more convenient to view H as a parameter that measures whether the fluid is kinetically or magnetically dominated. Unlike the usual plasma β , which measures the ratio of magnetic energy to microscopic, thermal energy, H measures the difference between the magnetic energy and the kinetic energy due to macroscopic fluid motion. There is a natural boundary at $H = 0$. The sign of H can be changed by reversing the signs of the filament strengths of either of the two species. This transformation simply switches the fields \mathbf{v} and \mathbf{B} .

4.3.1 Canonical Ensemble

Let us construct a partition function for the fixed-strength u - w filament system with the Hamiltonian H . The partition function is

$$Z = \int e^{-H/T} \prod_{i,s} d\mathbf{x}_i^s. \quad (4.26)$$

The trick in evaluating this integral is to represent our phase space not in terms of the coordinates of the filaments, but to take as phase variables the Fourier transforms of the filament densities,

$$\rho_s(\mathbf{k}) = \frac{\alpha^s}{V} \sum_{\ell \in s^+} e^{i\mathbf{k} \cdot \mathbf{x}_\ell} - \frac{\alpha^s}{V} \sum_{\ell \in s^-} e^{i\mathbf{k} \cdot \mathbf{x}_\ell} \quad (4.27)$$

in terms of which the Hamiltonian is

$$H = 8\pi V \sum_{\mathbf{k} \neq 0} \frac{1}{k^2} \Re(\rho_u \rho_w^*) + \text{const.}, \quad (4.28)$$

\Re denoting the real part.

Naturally, this substitution is only valid for large N , as, strictly speaking, there should only be as many ρ 's as there are filaments. Nevertheless, if we retain a large number of modes, we find that the Jacobian of our transformation, with error $\sim 1/N$, is

$$J = V^N \prod_{\mathbf{k}, s} \frac{V^2}{\pi N_s \alpha_s^2} e^{\frac{-V^2}{N_s \alpha_s^2} |\rho_s|^2}. \quad (4.29)$$

This can be verified directly by checking explicitly that

$$\langle |\rho_s|^{2n} \rangle = \int |\rho_s|^{2n} \prod_i d\mathbf{x}_i = \int J |\rho_s|^{2n} \prod_{\mathbf{k}, s} d\rho_s = n! \left(\frac{N_s \alpha_s^2}{V^2} \right)^n, \quad (4.30)$$

while all other moments are zero.

The partition function turns out to be

$$Z = \prod_{\mathbf{k}} \frac{k^2}{k^2 - \beta^2 k^{-2}}, \quad (4.31)$$

in which β is the normalized inverse temperature

$$\beta = \frac{4\pi \sqrt{N_u N_w} \alpha^u \alpha^w}{VT}. \quad (4.32)$$

The expected spectra are

$$\begin{aligned} \langle |\rho_s(\mathbf{k})|^2 \rangle &= \frac{N_s \alpha_s^2}{V^2} \frac{k^2}{k^2 - \beta^2/k^2} \\ \langle \Re(\rho_u \rho_w^*) \rangle &= \frac{\sqrt{N_u N_w} \alpha^u \alpha^w}{V^2} \frac{-\beta}{k^2 - \beta^2/k^2} \end{aligned} \quad (4.33)$$

In the case that $N_u = N_w$, $\alpha^u = \alpha^w$, these lead to the ω^2 and j^2 spectra

$$\begin{aligned}\langle \omega^2 \rangle &= \frac{k^2}{k^2 + \beta} \\ \langle j^2 \rangle &= \frac{k^2}{k^2 - \beta}\end{aligned}\tag{4.34}$$

These spectra are of the same form as eq. (2.23). If β is negative, the velocity spectrum will exhibit exaggerated large-scale structures, while if β is positive, magnetic islands of exactly the same form will appear.

4.3.2 Microcanonical Ensemble

The construction of a canonical ensemble assumes that a system is in contact with some reservoir of the conserved quantity. When the conserved quantity is internal energy, this thermal contact is easy to visualize and justify. It is, however, more difficult to envision a reservoir of constant $v^2 - B^2$, and we have very little idea how “thermal contact” between our system and such a reservoir might be maintained. More justifiable is the microcanonical ensemble appropriate for a closed system, in which the system motion is simply constrained to a surface on which the Hamiltonian is constant. This ensemble is also most appropriate for direct comparison with numerical simulations, in which “temperature” is notoriously ill-defined.

To study the microcanonical ensemble, we use the techniques of Edwards and Taylor [27], specifying the value of the Hamiltonian is specified to be E , and calculating the structure function, defined as

$$\Phi(E, V, N) = \int \delta(E - H) \prod_i d\mathbf{x}_i,\tag{4.35}$$

from which follows the entropy (and all other thermodynamic quantities),

$$S(E, V, N) = \ln \Phi\tag{4.36}$$

$$\frac{1}{T} = \left(\frac{\partial S}{\partial E} \right)_{V, N}\tag{4.37}$$

$$P = \left(\frac{\partial S}{\partial V} \right) \left(\frac{\partial S}{\partial E} \right)^{-1}. \quad (4.38)$$

Because our phase variables are physical coordinates, Φ is bounded by the volume of our system. A general consequence of systems with bounded phase space is that negative temperatures may be obtained [18], which will show increased order with higher energies.

Using the explicit representation of the delta function, we calculate

$$\Phi = \frac{1}{2\pi} \int d\lambda J \prod_{k,s} d\rho_s e^{i\lambda[E - 8\pi V \sum_k \frac{1}{k^2} \Re(\rho_u \rho_w^*)]}, \quad (4.39)$$

in which the domain of the ρ_s 's is the entire complex plane. These integrations, with the Gaussian integrand, are easily carried out, leaving only one integration over λ which we rescale to the dimensionless z , leaving

$$\tilde{\Phi} = \frac{1}{2\pi} \int dz e^{iz\tilde{E}} \prod_{n_x, n_y} \frac{1}{1 + \frac{z^2}{\pi^2 \kappa^4}}, \quad (4.40)$$

in terms of dimensionless quantities,

$$\begin{aligned} \tilde{\Phi} &= \Phi \frac{\sqrt{N_u N_w} \alpha^u \alpha^w}{V^N}, \\ \tilde{E} &= \frac{E}{\sqrt{N_u N_w} \alpha^u \alpha^w}. \end{aligned} \quad (4.41)$$

where $\kappa^2 = n_x^2 + n_y^2$ is the dimensionless wavenumber, and $k^2 = \frac{4\pi^2}{V} \kappa^2$.

The product in the integrand runs over all $n_x, n_y \geq 0$ except $n_x = n_y = 0$, and the integral can be reduced to an infinite sum over residues, which occur along the imaginary axis at $z = \pm i\pi\kappa$. The general form for $\tilde{\Phi}$ is

$$\tilde{\Phi} = \sum_{n_x, n_y} P_{n-1}(|\tilde{E}|) e^{-\pi\kappa^2 |\tilde{E}|}, \quad (4.42)$$

where P_{n-1} is a polynomial whose degree is one less than the degeneracy of the (n_x, n_y) mode. Φ , in contrast to the hydrodynamical structure function, is symmetric with respect to E , and differs from a Gaussian distribution in that

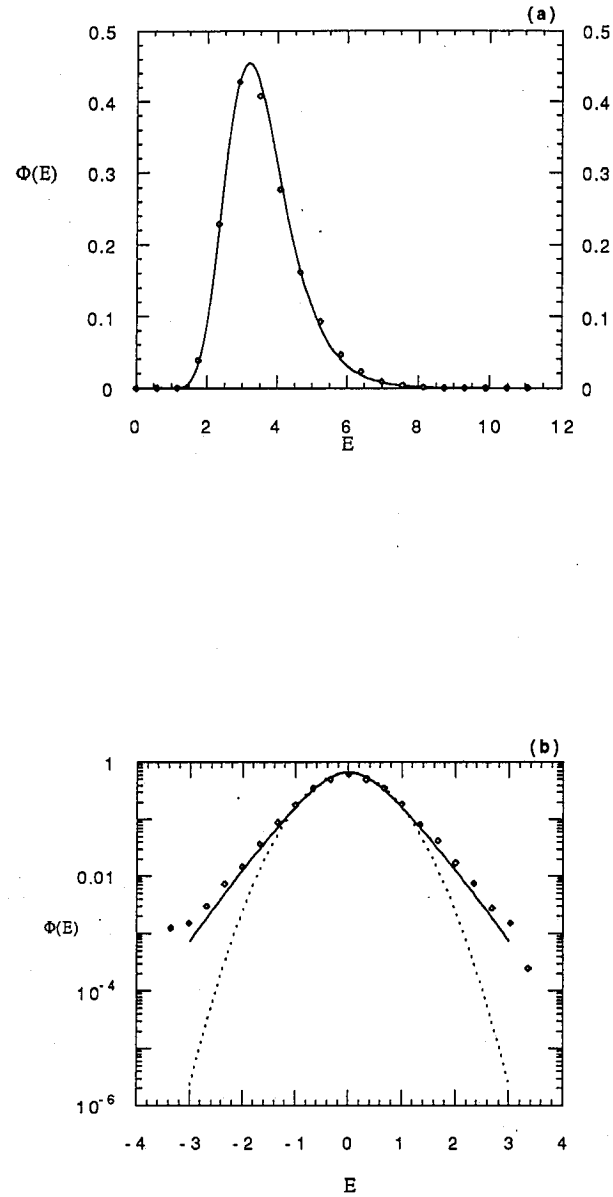


Figure 4.2: Structure functions for (a) the single-species hydrodynamical system, and (b) the $u-w$ system. Solid lines are from theory, while points are histograms from random data samples. The dotted line in (b) is a Gaussian distribution, shown for comparison.

it asymptotically approaches $e^{-\pi\kappa_{\min}|\tilde{E}|}$ as $|\tilde{E}| \rightarrow \pm\infty$. Figure 4.2(a) shows the structure function of the hydrodynamical structure function, from a numerical integration of the results of Ref. [27]. Figure 4.2(b) shows the u - w structure function, $\tilde{\Phi}$, from a numerical integration of eq. (4.40), along with a Gaussian for comparison, both normalized and chosen to correspond at $\tilde{E} = 0$. Also shown are histogram data of \tilde{E} from an ensemble of filament systems with fixed filament intensities and random filament positions. The small number of events in the tails of the distribution of \tilde{E} causes some scatter in the data, but the data conforms to the calculated structure function in the center and clearly deviates from a Gaussian in the tail.

One may also calculate the filament density spectra,

$$\begin{aligned} \frac{\langle |\rho_u(n'_x, n'_y)|^2 \rangle}{N_u \alpha^{u^2}} &= \frac{\langle |\rho_w(n'_x, n'_y)|^2 \rangle}{N_w \alpha^{w^2}} \\ &= \frac{1}{V^2} \frac{1}{2\pi\tilde{\Phi}} \int dz e^{iz\tilde{E}} \frac{1}{1 + \frac{z^2}{\pi^2(n_x'^2 + n_y'^2)^2}} \prod_{n_x, n_y} \frac{1}{1 + \frac{z^2}{\pi^2\kappa^4}}, \end{aligned} \quad (4.43)$$

and the correlation spectrum,

$$\begin{aligned} \frac{\langle \rho_u(n'_x, n'_y) \rho_w^*(n'_x, n'_y) \rangle}{\sqrt{N_u N_w} \alpha^u \alpha^w} &= \frac{1}{V^2} \frac{1}{2\pi\tilde{\Phi}} \int dz \frac{-iz}{\pi\kappa^2} e^{iz\tilde{E}} \frac{1}{1 + \frac{z^2}{\pi^2(n_x'^2 + n_y'^2)^2}} \prod_{n_x, n_y} \frac{1}{1 + \frac{z^2}{\pi^2\kappa^4}} e^{-\pi\kappa^2|\tilde{E}|}. \end{aligned} \quad (4.44)$$

While, $\langle |\rho_u|^2 \rangle$ and $\langle |\rho_w|^2 \rangle$ are even in E , $\langle \rho_u \rho_w^* \rangle$ is odd. Both have a pronounced lowest-wavenumber component when $|\tilde{E}|$ is large. Ensemble-average spectra of usual fluid quantities can be calculated from these density spectra by the relations

$$\begin{aligned} \langle \omega^2 \rangle &= \frac{1}{4} \langle |\rho_u(\kappa) + \rho_w(\kappa)|^2 \rangle \\ \langle j^2 \rangle &= \frac{1}{4} \langle |\rho_u(\kappa) - \rho_w(\kappa)|^2 \rangle \\ \langle \mathbf{v} \cdot \mathbf{B} \rangle &= \kappa^{-2} \frac{1}{2} \left(\langle |\rho_u(\kappa)|^2 \rangle - \langle |\rho_w(\kappa)|^2 \rangle \right). \end{aligned} \quad (4.45)$$

We evaluate (4.40), (4.43), and (4.44) numerically, and in figure 4.3, show $\langle \omega^2(\kappa^2) \rangle$ for $N_u = N_w$ and $\alpha^u = \alpha^w$. The spectrum of ω^2 always flattens out at large κ , and when \tilde{E} is large, there is a dominance of vorticity in the longest wavelength mode, such that the longest-wavelength mode grows proportional to E as $E \rightarrow \infty$. As $E \rightarrow -\infty$, the lowest-wavelength mode approaches a constant value ≈ 0.26 . As mentioned before, changing the sign of E interchanges the spectra of j^2 and ω^2 , so a concentration of magnetic energy at long wavelengths is expected for $\tilde{E} \ll -1$.

Comparing these results with those from [60] in eq. (4.4) we see that, not surprisingly, their magnetic spectrum differs from ours in the limit of large k . Indeed, it is precisely at short length scales that the filament model differs manifestly from the Fourier mode representation. At long wavelengths, though, both pictures give the same prediction: magnetic energy accumulation at large wavelengths. Indeed, the conditions necessary are the same; for (4.4) to yield peaked structure at $k = k_{\min}$, α and γ must be of different signs, or, by eq. (4.6), $\int v^2 < \int B^2$, just as our $E = \int v^2 - B^2$ must be negative to produce the magnetic islands.

The velocity spectrum, however, is quite different. Eq. (4.4) always predicts a flat kinetic energy spectrum, even when the magnetic field is identically zero. The reason is that the Fourier statistics are based on the MHD invariants, but as the magnetic field shrinks to zero, the invariants of the system change. The total energy becomes the kinetic energy normally, but the mean squared magnetic potential goes to zero. The enstrophy, meanwhile, changes at a rate proportional to the magnetic field strength. As the magnetic energy vanishes, the enstrophy should be included as an invariant in the calculations. The omission of the enstrophy as an invariant in the analysis dramatically alters the spectrum. The Elsasser variables approach the neutral limit more easily because none of the field variables vanish for vanishing magnetic field.

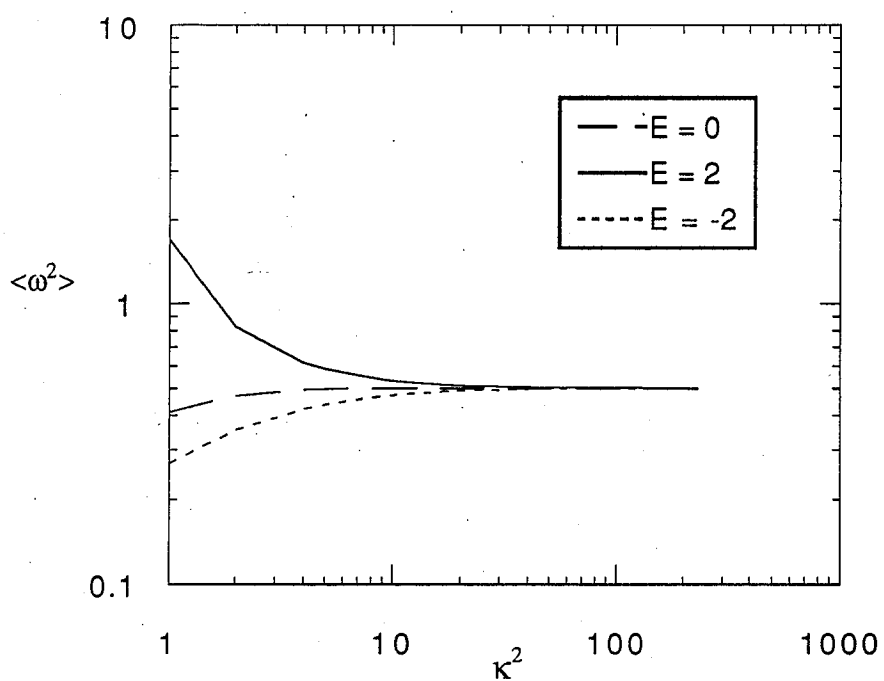


Figure 4.3: Spectra of $\langle \omega^2 \rangle$ from the u - w micro-canonical ensemble. Positive energies give large-scale velocity field structure.

Instead, the u and w fields approach each other and become identical in the zero magnetic field limit.

4.3.3 Most Probable Filamentary States

We use the formalism outlined in [31] to determine the most probably states in the filamentary MHD representation, for systems We have a system of $N \equiv N^u + N^w$ filaments. Of the u filaments, $n_+^u N^u$ of the filaments have strength α^u , and $n_-^u N^u$ have strength $-\alpha^u$, and similarly for the w filaments. We define an N-Point probability function in the microcanonical ensemble,

$$P_N(\mathbf{r}_1^u, \dots, \mathbf{r}_{N^u}^u, \mathbf{r}_1^w, \dots, \mathbf{r}_{N^w}^w) = \delta(E - H) / \Phi(E, V). \quad (4.46)$$

which has been normalized such that

$$\int P_N d\mathbf{r}_1^u, \dots, d\mathbf{r}_{N^w}^w = 1. \quad (4.47)$$

Temperature is defined by

$$\frac{1}{T} = \frac{\partial \ln \Phi}{\partial E}. \quad (4.48)$$

We define the single-filament probability densities

$$\begin{aligned} P_1^{u+}(\mathbf{r}) &= \int P_N \delta(\mathbf{r} - \mathbf{r}_1^u) d\mathbf{r}_1^u, \dots, d\mathbf{r}_{N^w}^w \\ P_1^{u-}(\mathbf{r}) &= \int P_N \delta(\mathbf{r} - \mathbf{r}_{n_+^u N^u + 1}^u) d\mathbf{r}_1^u, \dots, d\mathbf{r}_{N^w}^w \\ &\vdots, \end{aligned} \quad (4.49)$$

which, once known, give us the vorticity fields by

$$\begin{aligned} \langle \Omega^s \rangle &= \int \sum_i \alpha_i^s \delta(\mathbf{r} - \mathbf{r}_i^s) P_N d\mathbf{r}_1^u, \dots, d\mathbf{r}_{N^w}^w \\ &= N^s \alpha^u (n_+^s P_1^{s+} - n_-^s P_1^{s-}). \end{aligned} \quad (4.50)$$

We can obtain a differential equation for $P_1^{s\pm}$ directly from the definitions (4.46) and (4.49) and from the form of the Hamiltonian by differentiating (4.49) with respect to \mathbf{r} . This gives

$$\nabla P_1^{u+} = \int -\nabla H \frac{1}{\Phi} \frac{\partial}{\partial E} \delta(E - H) \delta(\mathbf{r} - \mathbf{r}_1^u) d\mathbf{r}_1^u, \dots, d\mathbf{r}_{N^w}^w. \quad (4.51)$$

As pointed out for hydrodynamical vortex filaments [33], there are two possible scalings of the energy with N . The first, in which energy scales $\propto N$, gives rise to Gaussian probability densities, for which the random-phase approach of the previous section is appropriate. The other possible scaling is $E \propto N^2$, which we adopt here. Because the temperature scales as N , the derivative of P_1 with respect to E is smaller than $\partial\Phi/\partial E$ by a factor of N , and may be neglected. This allows us to rewrite the derivative of the delta function as

$$\begin{aligned} \int \frac{\partial}{\partial E} \delta(E - H) d\mathbf{r}_1^u, \dots, d\mathbf{r}_{N^w}^w \\ &= \frac{\partial}{\partial E} \Phi P_2(\mathbf{r}_i, \mathbf{r}_j) d\mathbf{r}_i d\mathbf{r}_j \\ &\approx \frac{\partial}{\partial E} (\Phi P_1(\mathbf{r}_i) P_1(\mathbf{r}_j)) d\mathbf{r}_i d\mathbf{r}_j \\ &\approx \frac{\partial\Phi}{\partial E} P_1(\mathbf{r}_i) P_1(\mathbf{r}_j) d\mathbf{r}_i d\mathbf{r}_j, \end{aligned} \quad (4.52)$$

where the approximation of the two-point probability density as the product of two single-point probabilities has also been made. The differential equation becomes

$$\nabla P_1^{u+} = \frac{\alpha^w \alpha^u N^w}{T} P_1^{u+} \int \nabla G(\mathbf{r}, \mathbf{r}') (n_+^w P_1^{w+} - n_-^w P_1^{w-}). \quad (4.53)$$

Similar equations can be obtained for the other probability densities, which may be integrated to give differential equations for the potentials A^u and A^w ,

$$\begin{aligned} \nabla^2 A^u &= C^{u+} e^{\frac{\alpha^u}{T} A^w} - C^{u-} e^{-\frac{\alpha^u}{T} A^w} \\ \nabla^2 A^w &= C^{w+} e^{\frac{\alpha^w}{T} A^u} - C^{w-} e^{-\frac{\alpha^w}{T} A^u}. \end{aligned} \quad (4.54)$$

In the case in which $n_+^s = n_-^s$, this becomes

$$\begin{aligned}\nabla^2 A^u &= C^{u2} \sinh\left(\frac{\alpha^u}{T} A^w\right) \\ \nabla^2 A^w &= C^{w2} \sinh\left(\frac{\alpha^w}{T} A^u\right).\end{aligned}\quad (4.55)$$

In the zero magnetic field limit, $A^u \rightarrow A^w$, and we recover the neutral-fluid most-probable state, typical solutions of which describe a pair of large-scale opposite-sign filaments. If we let $\alpha^u = \alpha^w = \alpha$, then from (4.55) follows

$$\begin{aligned}\int |\nabla(A^u + A^w)|^2 &= -\frac{T}{\alpha} \int \frac{\alpha}{T} (A^u + A^w) \left(\sinh \frac{\alpha}{T} A^u + \sinh \frac{\alpha}{T} A^w \right) \\ \int |\nabla(A^u - A^w)|^2 &= \frac{T}{\alpha} \int \frac{\alpha}{T} (A^u - A^w) \left(\sinh \frac{\alpha}{T} A^u - \sinh \frac{\alpha}{T} A^w \right).\end{aligned}\quad (4.56)$$

Because \sinh is a monotonic function, the integrands in eq. (4.56) are all positive definite. This constrains the solutions of (4.55) to obey $A^u + A^w = 0$ if β is positive, or $A^u - A^w = 0$ if β is negative. In other words, there arise two possibilities for the most probable state: either $B = 0$, with the stream function obeying the \sinh -Poisson equation (2.39), or $v = 0$, with the vector potential obeying (2.39).

4.4 Variable-Strength Filaments

We expand our system to allow for filament strengths to change in time under the inductive force. The phase space now consists not only of the filament positions $\{x_i, y_i\}$, but the intensities $\{\alpha_i\}$ as well. At this point we make no attempt to continue with a Hamiltonian approach, but show only that these variables satisfy Liouville's theorem. The flow is conservative in phase space if and only if

$$\sum_s \sum_{i \in s} \frac{\partial \dot{\alpha}_i^s}{\partial \alpha_i^s} + \frac{\partial \dot{x}_i^s}{\partial x_i^s} + \frac{\partial \dot{y}_i^s}{\partial y_i^s} = 0. \quad (4.57)$$

In fact, we can prove a detailed Liouville's theorem in which each term of eq. (4.57) is satisfied separately. The x and y equations of motion are the same as

in the Hamiltonian case, so

$$\frac{\partial \dot{x}_i^s}{\partial x_i^s} + \frac{\partial \dot{y}_i^s}{\partial y_i^s} = 0 \quad (4.58)$$

as before. That the remaining term is zero is no more than the statement that a filament does not change strength under its own field. We write

$$\dot{\alpha}_i = \pm S(\mathbf{x}_i) = \pm \epsilon_{ij3} \partial_\ell u_j \partial_\ell w_k(\mathbf{x}_i). \quad (4.59)$$

The derivative $\partial \dot{\alpha}_i / \partial \alpha_i$ is determined by the field of a single filament, evaluated at its own center. The derivatives satisfy $\partial_x u_x = \partial_y u_y = 0$ at the filament center, so we conclude that

$$\frac{\partial \partial_\ell u_j(\mathbf{x}_i^u)}{\partial \alpha_i^u} \propto \epsilon_{j\ell 3}, \quad (4.60)$$

which gives

$$\frac{\partial \dot{\alpha}_i^s}{\partial \alpha_i^s} \propto \epsilon_{j\ell 3} \epsilon_{ijk} \partial_\ell w_k = 0, \quad (4.61)$$

and proves eq. (4.57).

The case in which the source is ignored has only one constant of the motion: the Hamiltonian $\int \mathbf{u} \cdot \mathbf{w}$. Even though the source term has only a small effect on the motions of individual filaments, the overall effect of neglecting the source is to cause the usual constants of total energy, cross-helicity, and mean square potential to be no longer conserved. What is interesting in our study is that the parameter $\int v^2 - B^2$ is of crucial importance to the qualitative behavior of the plasma, and modeling a system in which that parameter is conserved gives appropriate predictions for the full MHD system.

For filaments with the source term, it is most convenient to speak of the conserved quantities,

$$E^u = \frac{1}{2} \int u^2 = \frac{1}{2} \int v^2 + B^2 + \int \mathbf{v} \cdot \mathbf{B}, \quad (4.62)$$

and

$$E^w = \frac{1}{2} \int w^2 = \frac{1}{2} \int v^2 + B^2 - \int \mathbf{v} \cdot \mathbf{B}, \quad (4.63)$$

in addition to the mean squared magnetic potential,

$$A = \frac{1}{8} \int (A^u - A^w)^2. \quad (4.64)$$

In order to determine to what extent these quantities are preserved by the u - w filament system, we write the energy E^u in terms of filament quantities

$$E^u = \frac{1}{2} \sum_{i,j} \alpha_i^u \alpha_j^u G(\mathbf{x}_i^u, \mathbf{x}_j^u) = \frac{1}{2} \sum_i \alpha_i^u A^u(\mathbf{x}_i^u). \quad (4.65)$$

This energy changes in time as

$$\dot{E}^u = \sum_i \dot{\alpha}_i^u A^u(\mathbf{x}_i^u) + \sum_i \alpha_i^u \dot{\mathbf{z}} \cdot \mathbf{u}(\mathbf{x}_i^u) \times \mathbf{w}(\mathbf{x}_i^u). \quad (4.66)$$

With $\dot{\alpha}_i^u = S(\mathbf{x}_i^u)$ the sum over filaments is just the Monte-Carlo approximation of the corresponding continuous integral. Since we are assuming the system is ergodic and mixing, these approximations will become exact in the limit $N^u \rightarrow \infty$,

$$\lim_{N \rightarrow \infty} \dot{E}^u = \int S A^u + \int \Omega^u \mathbf{u} \times \mathbf{w}. \quad (4.67)$$

Since, in two dimensions,

$$\begin{aligned} \int S A^u &= \frac{1}{2} \int A^u \nabla^2 (\mathbf{u} \times \mathbf{w}) - \frac{1}{2} \int A^u (\nabla^2 \mathbf{u}) \times \mathbf{w} - \frac{1}{2} \int A^u \mathbf{u} \times (\nabla^2 \mathbf{w}) \\ &= -\frac{1}{2} \int \Omega^u \mathbf{u} \times \mathbf{w} + \frac{1}{2} \int \Omega^w \mathbf{u} \cdot \nabla A^u + \frac{1}{2} \int \Omega^u \mathbf{u} \cdot \nabla A^w \\ &= -\int \Omega^u \mathbf{u} \times \mathbf{w}, \end{aligned} \quad (4.68)$$

this energy is conserved in the continuous limit, even though it is not manifestly conserved exactly for finite N .

We will again use the random-phase approximation to evaluate the partition function in terms of filament densities ρ_s .

$$E^u = \sum_{ij} \alpha_i^u \alpha_j^u G(\mathbf{x}_i^u, \mathbf{x}_j^u) = \sum_k \frac{1}{k^2} |\rho_u|^2 + \sum_k \frac{1}{k^2} \sum_i \alpha_i^{u2} \quad (4.69)$$

$$E^w = \sum_{ij} \alpha_i^w \alpha_j^w G(\mathbf{x}_i^w | \mathbf{x}_j^w) = \sum_k \frac{1}{k^2} |\rho_w|^2 + \sum_k \frac{1}{k^2} \sum_i \alpha_i^{w2} \quad (4.70)$$

$$A = \sum_k \frac{1}{k^4} |\rho_u|^2 + |\rho_w|^2 - 2\Re(\rho_u \rho_w^*) + \sum_k \frac{1}{k^4} \left[\sum_i \alpha_i^{u2} + \sum_i \alpha_i^{w2} \right]. \quad (4.71)$$

When writing these invariants in terms of the Fourier modes, a sum of self-energies emerges. When the filaments are allowed to change strength, these self-energies are no longer constant, as the integral over configuration space includes an integral over all filament strengths. The partition function is

$$Z = \int e^{-E^u/T^u - E^w/T^w - A/T^A} \prod_i d\mathbf{x}_i^u d\alpha_i^u \prod_j d\mathbf{x}_j^w d\alpha_j^w. \quad (4.72)$$

When we change the variables of integration from filament positions to Fourier components, we must use the Jacobian for which

$$\begin{aligned} & \exp \left\{ - \sum_k \left[\frac{1}{T^u k^2} + \frac{1}{T^A k^4} \right] \sum_i \alpha_i^{u2} \right. \\ & \quad \left. - \sum_k \left[\frac{1}{T^w k^2} + \frac{1}{T^A k^4} \right] \sum_j \alpha_j^{w2} \right\} \prod_{ij} d\mathbf{x}_i^u d\alpha_i^u d\mathbf{x}_j^w d\alpha_j^w \\ & = J \prod_k d\rho_u d\rho_u^* d\rho_w d\rho_w^*. \end{aligned} \quad (4.73)$$

This Jacobian is again a Gaussian, as can be verified by checking that the moments are

$$\int |\rho_s|^{2n} = n! \left(\frac{N_s \langle \alpha^{s2} \rangle}{V^2} \right)^n \quad (4.74)$$

to leading order in N . All that differs from the case in which the filament strengths are fixed is the replacement of the constant α^{s2} by the expected value

$$\langle \alpha^{s2} \rangle = \int \alpha^{s2} \exp \left\{ - \left[\frac{1}{T^s k^2} + \frac{1}{T^A k^4} \right] \alpha_i^{s2} \right\} d\alpha^s. \quad (4.75)$$

Defining, as before, the normalized inverse temperatures

$$\beta^s = \frac{4\pi N_s^2 \langle \alpha^{u2} \rangle}{VT^s}, \quad \beta^A = \frac{4\pi \sqrt{N_u N_w \langle \alpha^{u2} \rangle \langle \alpha^{w2} \rangle}}{VT^A}, \quad (4.76)$$

the partition function takes the form

$$Z = \prod_{\mathbf{k}} \left[(1 + \beta^u k^{-2} + \beta^A k^{-4}) (1 + \beta^w k^{-2} + \beta^A k^{-4}) - \beta^{A^2} k^{-8} \right]^{-1}, \quad (4.77)$$

and the expected spectra are

$$\begin{aligned} \langle |\rho_u|^2 \rangle &= \frac{1 + \beta^w k^{-2} + \beta^A k^{-4}}{(1 + \beta^u k^{-2} + \beta^A k^{-4}) (1 + \beta^w k^{-2} + \beta^A k^{-4}) - \beta^{A^2} k^{-8}} \\ \langle |\rho_w|^2 \rangle &= \frac{1 + \beta^u k^{-2} + \beta^A k^{-4}}{(1 + \beta^u k^{-2} + \beta^A k^{-4}) (1 + \beta^w k^{-2} + \beta^A k^{-4}) - \beta^{A^2} k^{-8}} \\ \langle \Re(\rho_u \rho_w^*) \rangle &= \frac{\beta^A k^{-4}}{1 + \beta^u k^{-2} + \beta^A k^{-4}} \langle |\rho_u|^2 \rangle \\ &= \frac{\beta^A k^{-4}}{1 + \beta^w k^{-2} + \beta^A k^{-4}} \langle |\rho_w|^2 \rangle. \end{aligned} \quad (4.78)$$

Even in the regime $\langle \mathbf{v} \cdot \mathbf{B} \rangle = 0$, eqs. (4.78) display a great range of possible behaviors. Figure 4.4 demonstrates how, in the limit of small temperatures, these spectra approach the equilibrium spectra of the Fourier-mode theory. On the other hand, in the high temperature regime, these spectra conform more closely to the spectra of the $S = 0$ theory of the previous section, as shown in figure 4.5. Especially noteworthy is the continued allowability of peaked vorticity as well as current in the longest wavelength mode.

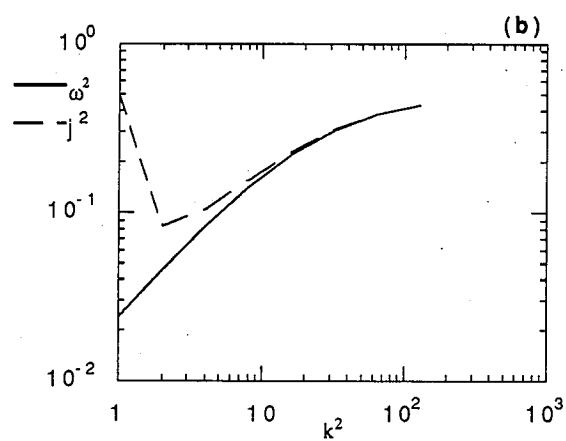
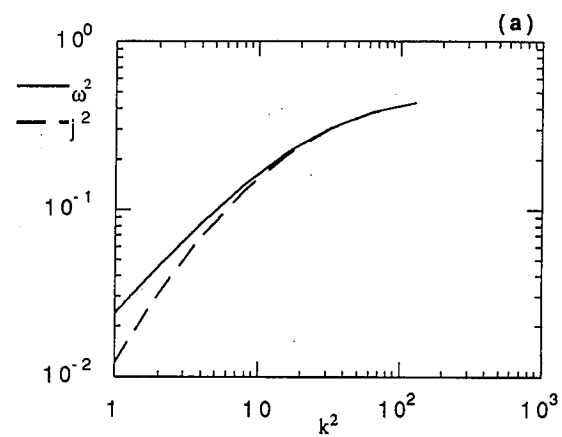


Figure 4.4: Equilibrium spectra of the $u-w$ filamentary system with source included. Regime shown is $|\beta| \gg 1$, the low-energy limit for which the spectra approach the Fourier theory's predictions.

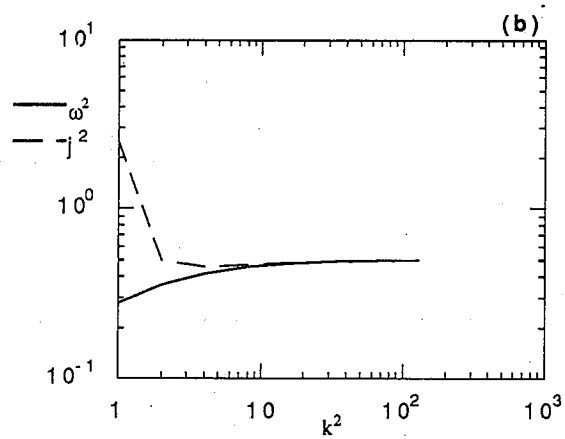
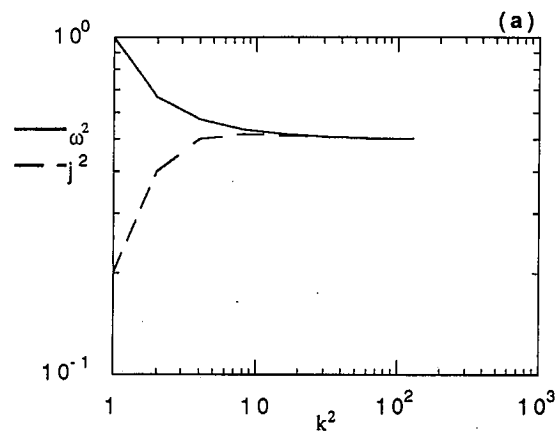


Figure 4.5: Spectra of ω and j for $|\beta| \sim 1$, the high-energy limit that mimics the behavior of the $S = 0$ approximation.

Chapter 5

Simulations of Two-Dimensional MHD Filaments

One of the advantages of the point-vortex representation brought to hydrodynamics was the added ability to model systems with very high Reynolds number. As viscosity decreases, the fluid has an increasing tendency to form extremely small-scale structures [4]. In order for a standard spectral fluid code to model such structures, greater and greater grid size must be used in order to have resolution sufficient to resolve these fine structures. A vortex-based algorithm [57], by assuming such structure *a priori* should be generally able to handle low-viscosity systems at a lower cost. Newer techniques have also been developed [43] in which finite viscosity effects can be included in a vortex system by allowing vortex filaments to combine when brought sufficiently close together, according to some phenomenologically determined reconnection rule [40].

5.1 Numerical Algorithm

Our primary assumption is that the vorticities Ω are concentrated into localized filaments. We will let the filaments have a finite core size,

$$\begin{aligned}\Omega^u(\mathbf{x}, t) &= \sum_i \alpha_i(t) \Delta(\mathbf{x} - \mathbf{x}_i^u(t)) \\ \Omega^w(\mathbf{x}, t) &= \sum_i \alpha_i(t) \Delta(\mathbf{x} - \mathbf{x}_i^w(t)),\end{aligned}\tag{5.1}$$

with shape Δ . We use a finite-particle method [63] such that the shape is a Gaussian,

$$\Delta(\mathbf{x}) = \frac{1}{2\pi a_x a_y} e^{-\frac{x^2}{2a_x^2} - \frac{y^2}{2a_y^2}}. \quad (5.2)$$

The algorithm traces the locations \mathbf{x}_i and strengths α_i of the magnetic vortex filaments. In terms of these variables, the MHD equations are

$$\begin{aligned} \sum_i \dot{\alpha}_i^u \Delta(\mathbf{x} - \mathbf{x}_i^u) + \sum_i \alpha_i^u \dot{\mathbf{x}}_i^u \cdot \nabla \Delta(\mathbf{x} - \mathbf{x}_i^u) \\ + \mathbf{w} \cdot \nabla \sum_i \alpha_i^u \Delta(\mathbf{x} - \mathbf{x}_i^u) = S \\ \sum_i \dot{\alpha}_i^w \Delta(\mathbf{x} - \mathbf{x}_i^w) + \sum_i \alpha_i^w \dot{\mathbf{x}}_i^w \cdot \nabla \Delta(\mathbf{x} - \mathbf{x}_i^w) \\ + \mathbf{u} \cdot \nabla \sum_i \alpha_i^w \Delta(\mathbf{x} - \mathbf{x}_i^w) = -S, \end{aligned} \quad (5.3)$$

which we separate into the two sets of equations for the α 's and the \mathbf{x}_i 's. The positions must evolve by

$$\begin{aligned} \dot{\mathbf{x}}_i^u &= \int \mathbf{w}(\mathbf{x}, t) \Delta(\mathbf{x} - \mathbf{x}_i^u) \\ \dot{\mathbf{x}}_i^w &= \int \mathbf{u}(\mathbf{x}, t) \Delta(\mathbf{x} - \mathbf{x}_i^w). \end{aligned} \quad (5.4)$$

The filament strengths must change in such a way as to satisfy

$$\begin{aligned} \sum_i \dot{\alpha}_i^u(t) \Delta(\mathbf{x} - \mathbf{x}_i^u) &= S(\mathbf{x}, t) \\ \sum_i \dot{\alpha}_i^w(t) \Delta(\mathbf{x} - \mathbf{x}_i^w) &= -S(\mathbf{x}, t). \end{aligned} \quad (5.5)$$

Since S is a continuous function of space, the success of this scheme depends on the filaments being distributed throughout the volume with inter-vortex spacing no larger than the filament cross-section. We let the vortex filaments change strengths according to

$$\begin{aligned} \dot{\alpha}_i^u &= S(\mathbf{x}_i^u)/n^u \\ \dot{\alpha}_i^w &= -S(\mathbf{x}_i^w)/n^w, \end{aligned} \quad (5.6)$$

where n^s is the average number density of the species s . Since the accuracy of this scheme will decrease as the filament distribution becomes more uneven, one future improvement will allow for the addition of extra filaments, with strength initially zero, into areas in which the filament density falls below a threshold value.

In order to solve for the fields to advance the equations, we use a Fast Fourier Transform field solver on a periodic grid. The vorticity is first accumulated as a grid quantity. The vorticity field of a collection of filaments with finite core size is a convolution of the delta-function-shaped filaments with the shape factor Δ ,

$$\begin{aligned}\rho(\mathbf{x}) &= \sum_i \alpha_i \delta(\mathbf{x} - \mathbf{x}_i) \\ \Omega(\mathbf{x}) &= \int \Delta(\mathbf{x} - \mathbf{x}') \rho(\mathbf{x}') d\mathbf{x}' \\ \Omega(\mathbf{k}) &= \Delta(\mathbf{k}) \rho(\mathbf{k}).\end{aligned}\tag{5.7}$$

The convolution of a function f with Δ results in a smoothing of that function. Notationally, for any function f , we define

$$\begin{aligned}\bar{f}(\mathbf{k}) &= \Delta(\mathbf{k}) f(\mathbf{k}) \\ \hat{f}(\mathbf{k}) &= \Delta^{-1}(\mathbf{k}) f(\mathbf{k}).\end{aligned}\tag{5.8}$$

The density ρ may be accumulated to the grid from the particle positions by a variety of techniques. Energy conservation is aided by choosing a scheme in which the grid assignment is continuous as a particle crosses a cell boundary [64]. The scheme which we use in two dimensions assigns weights to the nine cells nearest a particle. Let w_{00} designate the cell nearest the particle, and w_{01} represent the cell directly above, w_{10} directly to the right, etc, and let (x, y) be the relative displacement of the particle relative to the nearest cell. The weights are assigned by

$$w_{00} = \alpha_i \left(\frac{3}{4} - x^2 \right) \left(\frac{3}{4} - y^2 \right)$$

$$\begin{aligned}
w_{01} &= \alpha_i \left(\frac{3}{4} - x^2 \right) \frac{1}{2} \left(\frac{1}{2} + y \right)^2 \\
w_{0-1} &= \alpha_i \left(\frac{3}{4} - x^2 \right) \frac{1}{2} \left(\frac{1}{2} - y \right)^2 \\
w_{10} &= \alpha_i \frac{1}{2} \left(\frac{1}{2} + x \right)^2 \left(\frac{3}{4} - y^2 \right) \\
w_{11} &= \alpha_i \frac{1}{2} \left(\frac{1}{2} + x \right)^2 \frac{1}{2} \left(\frac{1}{2} + y \right)^2 \\
&\vdots
\end{aligned} \tag{5.9}$$

The total of all weights assigned to the neighbor cells is α_i , and the grid quantity, as well as its derivatives, changes continuously with the particle position.

Once Ω is known on the grid, it is Fourier-transformed and the u or w field is solved for straightforwardly:

$$u(\mathbf{k}) = \Delta^2(\mathbf{k}) \frac{i\mathbf{k} \times \hat{z} \rho_u(\mathbf{k})}{k^2}. \tag{5.10}$$

One factor of Δ comes from the smoothing of Ω when accumulated to the grid, and another from the averaging of u over the pushed particle's shape to produce its net motion. Also calculated are the derivatives of the fields,

$$\begin{aligned}
u_{xx}(\mathbf{k}) &= ik_x u_x(\mathbf{k}) = -u_{yy} \\
&\vdots
\end{aligned} \tag{5.11}$$

for use in calculating the source function

$$S = u_{xx}(w_{xy} - w_{yx}) - w_{xx}(u_{xy} - u_{yx}). \tag{5.12}$$

To advance the equations in a time-centered fashion, a predictor-corrector scheme is used. The progression of a time step is as follows.

Known at beginning of time-step:

$$\begin{aligned}
&\alpha^u_{n-1} x^u_{n-1}, y^u_{n-1}, \\
&\alpha^w_{n-1}, x^w_{n-1}, y^w_{n-1}, \\
&\alpha^u_n x^u_n, y^u_n,
\end{aligned}$$

$$\alpha^w_n, x^w_n, y^w_n,$$

Accumulate Ω from particles:

$$\{\alpha, x, y\}_n \rightarrow \rho_n$$

Calculate fields from Ω :

$$\{\Omega\} \rightarrow \{u_n, w_n, S_n\}$$

Find predicted particle quantities:

$$x^u_p = x^u_{n-1} + 2\Delta t w_n(x^u_n)$$

$$\alpha^u_p = \alpha^u_{n-1} + 2\Delta t S_n(x^u_n)$$

$$x^w_p = x^w_{n-1} + 2\Delta t u_n(x^w_n)$$

$$\alpha^w_p = \alpha^w_{n-1} - 2\Delta t S_n(x^w_n)$$

Calculate predicted fields:

$$\{\alpha, x, y\}_p \rightarrow \{\Omega\} \rightarrow \{u_p, w_p\}$$

Advance particle quantities to next time step:

$$x^u_{n+1} = x^u_n + \Delta t \frac{1}{2} (w_n(x^u_n) + w_p(x^u_p))$$

$$\alpha^u_{n+1} = \alpha^u_n + \Delta t \frac{1}{2} (S_p(x^u_n) + S_p(x^u_p))$$

$$x^w_{n+1} = x^w_n + \Delta t \frac{1}{2} (u(x^w_n) + u(x^w_p))$$

$$\alpha^w_{n+1} = \alpha^w_n - \Delta t \frac{1}{2} (S_n(x^w_n) + S_p(x^w_p)).$$

5.2 Constants of the Motion

The ability of the numerical algorithm to conserve the invariants E^u , E^w , and A depends on the degree to which the analytical expression for the time derivative,

$$\dot{E}_u = \partial_t \frac{1}{2} \int A^u \Omega^u = \int \Omega^u (w \cdot \nabla) A^u + \int A^u S. \quad (5.13)$$

is approximated by the discrete expression in terms of filament quantities,

$$\dot{E}_u = \sum_i \alpha_i^u \dot{x}_i^u \cdot \nabla \bar{A}_i^u + \sum_i \dot{\alpha}_i^u \bar{A}_i^u. \quad (5.14)$$

However, even if the filaments are arranged so that the sums of (5.14) can be converted to integrals, there will still be a non-zero time derivative of E^u due to the averaging of quantities over finite-sized filaments instead of point-vortices.

$$\begin{aligned}\dot{E}^u &\approx \int \rho^u \bar{\mathbf{u}} \times \bar{\mathbf{w}} + \int S \bar{A}^u \\ &= \int \rho^u \bar{\mathbf{u}} \times \bar{\mathbf{w}} - \frac{1}{2} \int \bar{\Omega}^u \mathbf{u} \times \mathbf{w} - \frac{1}{2} \int \Omega^u \bar{\mathbf{u}} \times \mathbf{w}.\end{aligned}\quad (5.15)$$

Because of the averaging over particle size (represented by the bars), this expression differs from eqs. (4.67) and (4.68), giving rise to a numerical diffusion. This diffusion goes to zero as the size of the vortices goes to zero, but finite-sized particles are very desirable for de-aliasing and other reasons [65]. Two approaches may be taken to counter this numerical diffusion. One is to rewrite the source term in a way so as to take account of the finite vortex shapes. The form of the source which conserves E^u and E^w for finite-sized vortices is

$$S = \frac{1}{2} \left[\nabla^2 \bar{\mathbf{u}} \times \bar{\mathbf{w}} - \bar{\mathbf{w}} \cdot \nabla \rho^u + \bar{\mathbf{u}} \cdot \nabla \rho^w \right], \quad (5.16)$$

This approach, however, gives an S which is an extremely spiky function of space, and is not well-handled by the interpolation schemes in the code. A second approach is to add a corrective term to the time-derivative of each filament, proportional to the strength of that filament, in such a way as to constrain the energies to remain constant. Such a correction turns out to be only a few percent of the change in strength due to the source term alone.

5.3 Tests of Known Fixed-Strength Filament Solutions

A system of u - w filaments in free space has the Hamiltonian as an invariant, in addition to three invariants arising from the translational and rotational symmetry of the Hamiltonian. These invariants are

$$Z_x = \sum_j \alpha_j x_i$$

$$\begin{aligned}
Z_y &= \sum_j \alpha_j y_i \\
M &= \sum_j \sum_k \alpha_j \alpha_k r_{jk}^2.
\end{aligned} \tag{5.17}$$

where $r_{jk}^2 = |\mathbf{x}_j - \mathbf{x}_k|^2$, and the sum runs over both species. Because of these symmetries, the system is integrable for some small numbers of filaments. For hydrodynamical vortex filaments, Novikov and Sedov [66] explored the three-filament case fully, in particular the case in which a trio of filaments collapse symmetrically to a point. Such solutions exist in the u - w case as well, so these solutions can be used as a test of the code. Because of the periodic boundary conditions of the code, these tests must be run in a small fraction of the computational boundary so that the effects of the image filaments are small.

The first, obvious, integrable case is for $N_u = N_w = 1$. The two filaments will rotate around their center of charge with a period equal to the squared separation divided by the reduced charge. The paths of two rotating filaments are shown in figure 5.1. Also shown is the distance between the filaments as a function of time. The distance varies by about 1% during one revolution. This effect is due to the image filaments. For larger separations, the filaments feel stronger effects from the images. The variation in radius increases, but the orbits are always closed.

For the symmetric collapsing case, we let $N_u = 1, N_w = 2$, numbering the u -filament is no. 1, and the two w -filaments nos. 2 and 3. We seek solutions in which

$$r_{jk}(t) = \lambda(t)r_{jk}(0). \tag{5.18}$$

That is, the triangle comprised by the filaments will shrink such that the ratio of the sides will be preserved. From the constancy of the Hamiltonian, solutions of this type require that

$$\alpha_1 \alpha_2 + \alpha_1 \alpha_3 = 0, \tag{5.19}$$

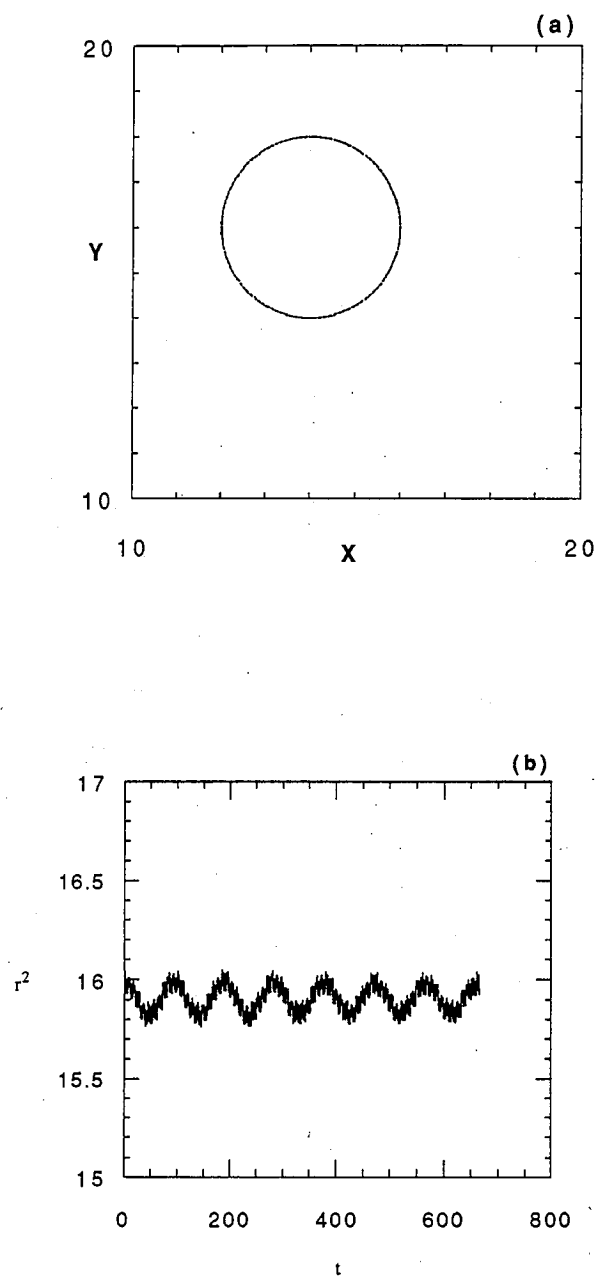


Figure 5.1: Paths of two rotating filaments (a), and the time history of their relative distance (b).

while in order for M to be conserved, we must have $M = 0$. The relative distance between two filaments can only change due to the action of the third filament. The time derivative of r_{jk} follows directly from the equations of motion and can be written

$$\begin{aligned}\dot{r}_{12}^2 &= \mp \frac{2}{\pi} A \alpha_3 r_{13}^{-2} \\ \dot{r}_{13}^2 &= \pm \frac{2}{\pi} A \alpha_2 r_{12}^{-2} \\ \dot{r}_{23}^2 &= \mp \frac{2}{\pi} A \alpha_1 (r_{12}^{-2} - r_{13}^{-2}).\end{aligned}\tag{5.20}$$

A is the area of the triangle formed by the three filaments. The first sign is taken if the filaments are numbered in a clockwise order, the opposite sign if the numbering is counter-clockwise. From eq. (5.20), it follows that

$$\dot{\lambda}^2 = \text{const.} = \mp \frac{2}{\pi} A \alpha_3 r_{13}^{-2} r_{12}^{-2} \Big|_{t=0}.\tag{5.21}$$

The three filaments collapse uniformly to a point as $\lambda \rightarrow 0$, rotating with an angular speed $\propto \lambda^{-2}$. At $\lambda = 0$, they coincide, reflect about the center of charge, and expand again, with the sign of $\dot{\lambda}^2$ reversed. The numerical code of course cannot accurately represent filaments spinning infinitely fast as they collapse to a singularity, but collapse beforehand and expansion afterward can be tracked and checked against theory.

Figure 5.2 shows the triangle of filaments during the numerical test of collapse. Filaments begin at the left, pass through the point of nearest approach in the middle, and end in the positions on the right. The triangle appears to have undergone nearly symmetric reflection. Figure 5.3(a) shows the ratios of the three sides to their initial lengths as the filaments collapse, up to the point where their mutual separation is about 1 grid space, the characteristic size of the Gaussian shapes given the filaments. The solid line is from eq. (5.21). Figure 5.3(b) shows these ratios as the triangle inverts and begins to expand again. The shape of the triangle has changed slightly, as evidenced by

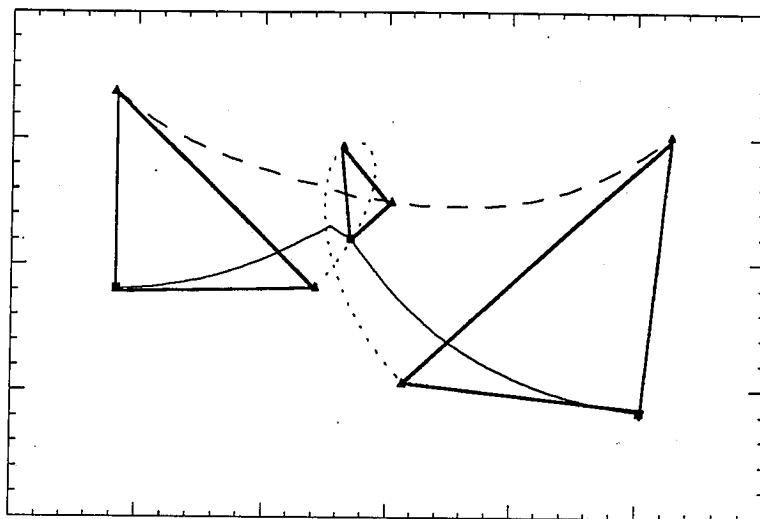


Figure 5.2: Paths of the collapsing trio of u - w filaments. The triangle rotates while shrinking, reflects, and expands.

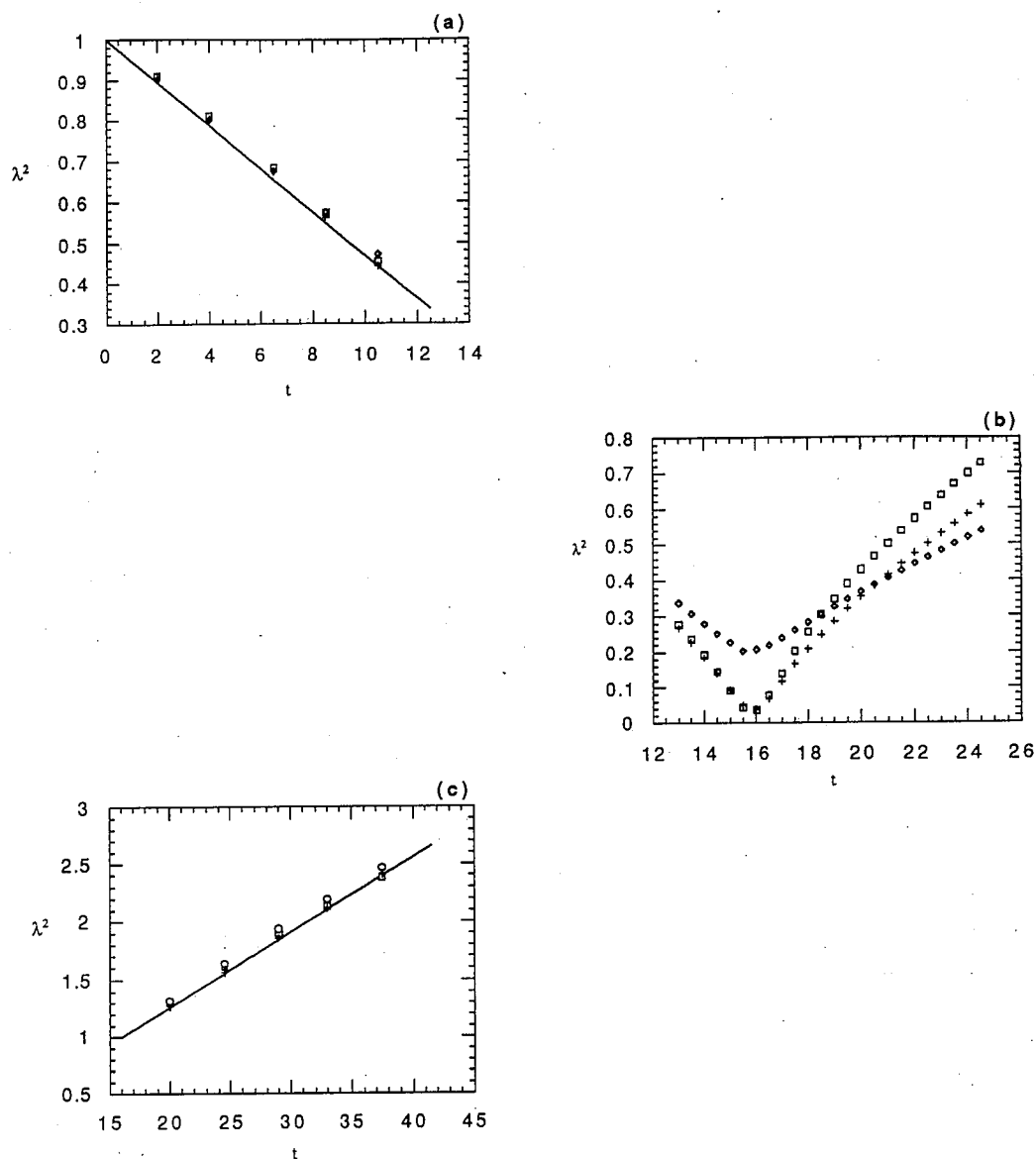


Figure 5.3: Plots of λ^2 , vs. t during (a) collapse, (b) bounce, and (c) expansion. The shape of the triangle is maintained during collapse and expansion, but changes slightly during the bounce.

the fact that the three ratios no longer coincide after the reversal. After this point, we take the sides as new initial positions and track the expansion of this triangle. Figure 5.3(c) shows the ratios of the sides to those lengths as the triangle expands.

5.4 Simulations of Large-N Filament Systems

We run the system on a 2-d grid of 32×32 points. First runs were made with filaments intensities fixed ($S = 0$), with an average filament density of one per cell (1024 of each species). Following the technique of [29] and [27], we load the filaments randomly into boxes distributed on the grid. Varying the size of the boxes provides some control over the energy of the system. Shown in figure 5.4 are u -filament positions for a run with energy $\tilde{E} \approx 75$. This is the lowest energy for which clumping of filaments is visible from phase-space plots. In this run, both u and w are given positive strengths of equal magnitude, and the magnetic energy is much less than the kinetic energy. Contour plots of the magnetic potential and the stream function are shown in figure 5.5. The magnetic field has no obvious structure, but the velocity field has clearly organized into one large positive and one negative vortex. Figure 5.6 shows a similar run with $\tilde{E} \approx 150$. In this run, the initial boxes are small enough that they evolve initially into distinct clusters, which gradually merge until there is only a single clump.

These runs indicate that the statistically preferred state is obtainable from general (and artificial) initial conditions. However, if a high degree of symmetry is imposed, the clusters of filaments do not mix, and interact more as independent filaments in a highly-organized crystal-like state, as shown in Figure 5.7. The initial square lattice quickly evolves to a hexagonal lattice which remains stable. The lattice, however, is loose enough to allow motion of the filament clusters and even interchange of positions in the lattice. During

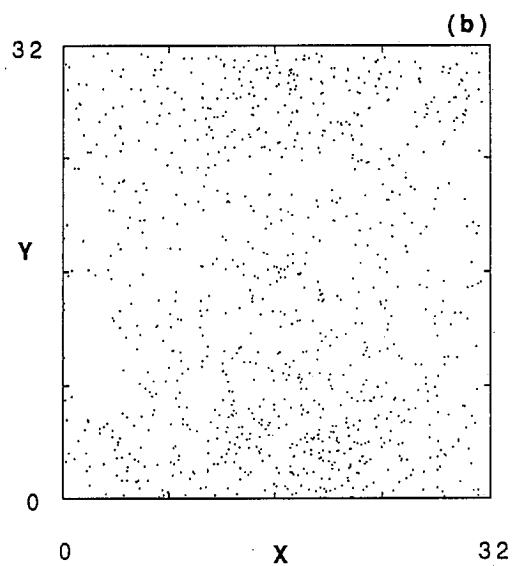
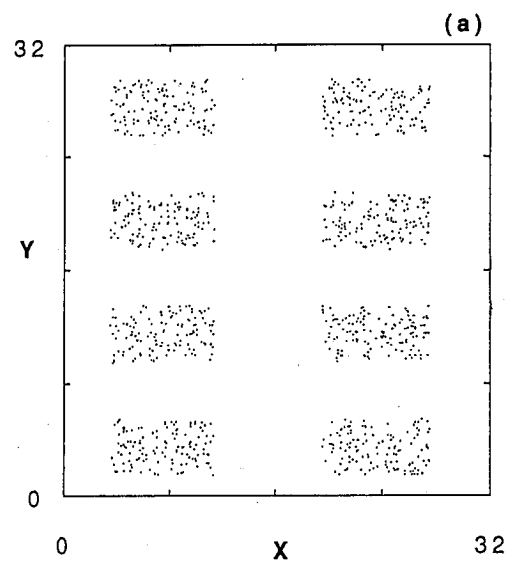
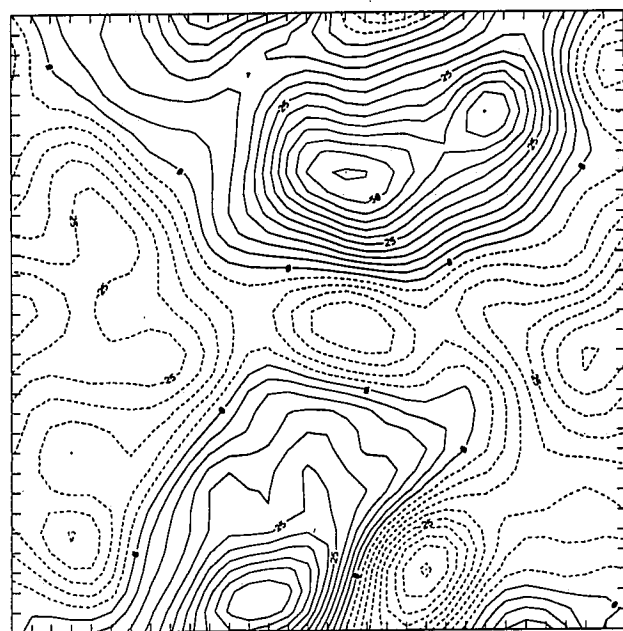
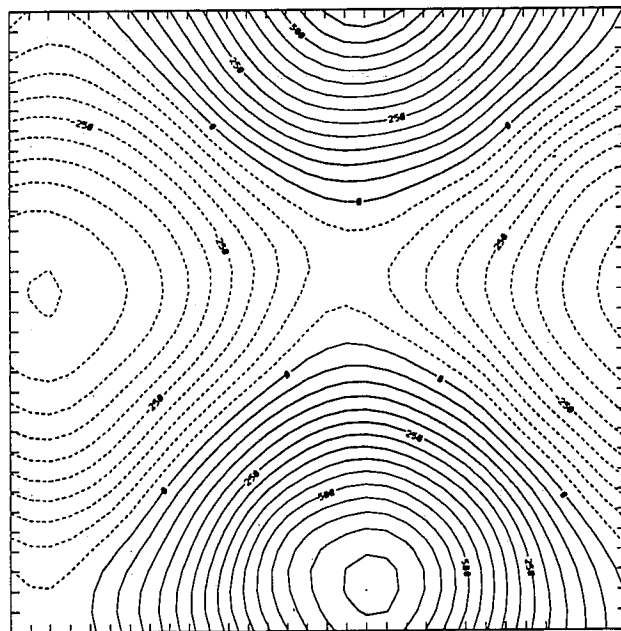


Figure 5.4: Phase-space plot of u -filament positions for $\tilde{E} \approx 75$ (a) initially and (b) at end of run.



CONTOUR FROM -45 TO 55 BY 5



CONTOUR FROM -500 TO 700 BY 50

Figure 5.5: Contours of (a) A_z and (b) Ψ for the final state of the run in the previous figure.

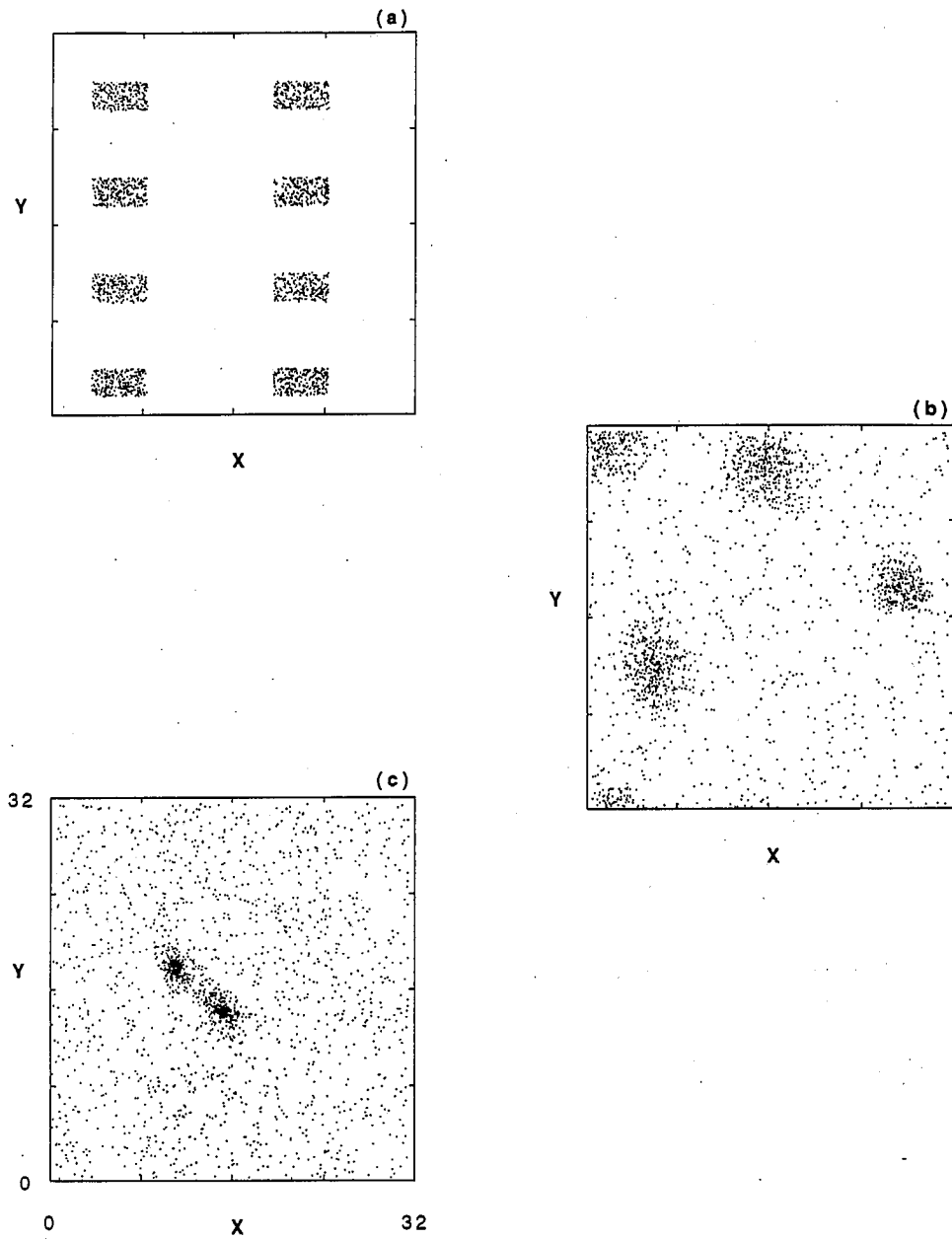


Figure 5.6: Filament positions from a run with $\tilde{E} \approx 150$. Initial positions are shown in (a). Large clusters of filaments form as in (b), eventually merging to a single clump as in (c).

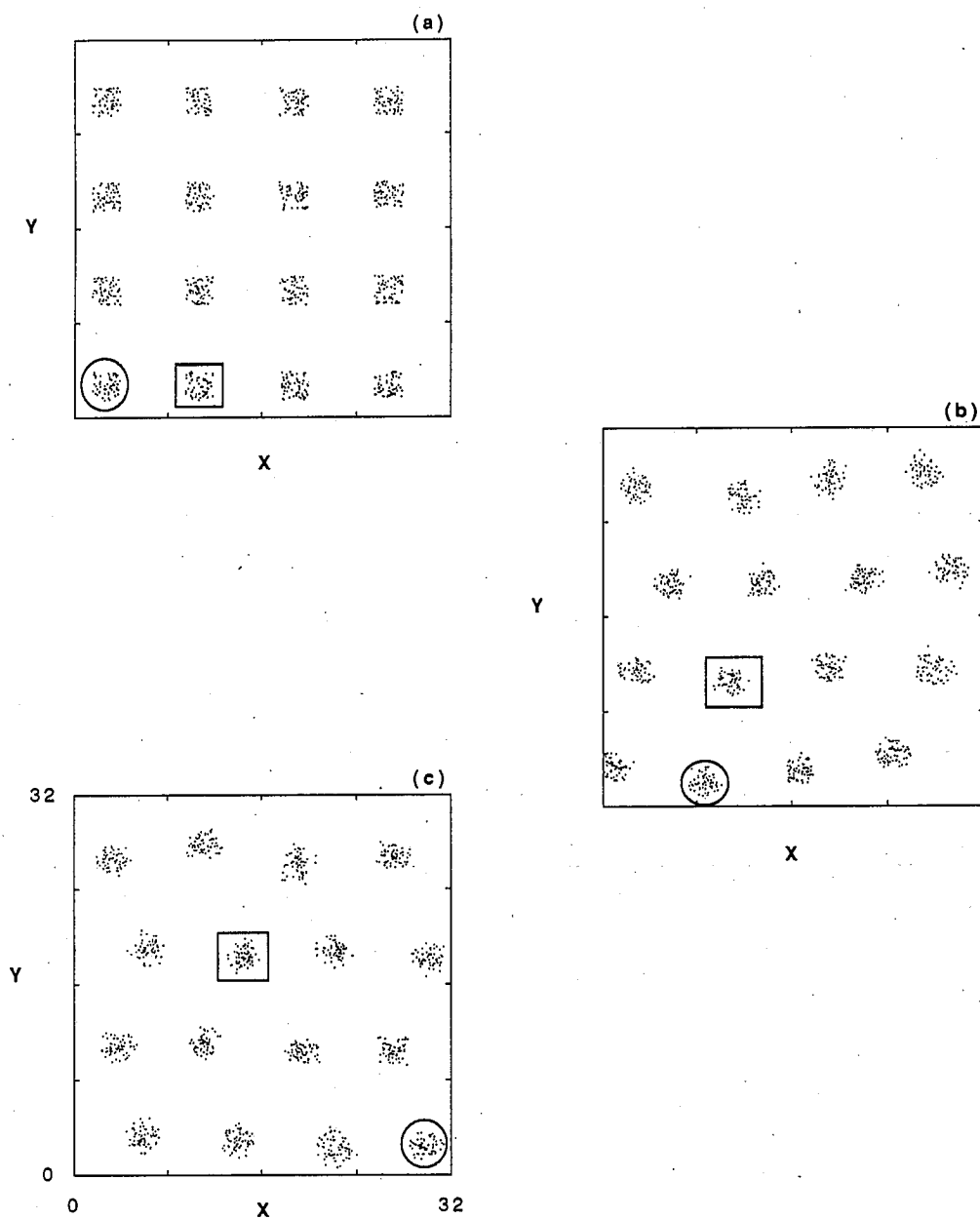


Figure 5.7: Filament positions from a run with filaments clustered onto a square lattice. The clusters quickly fall into a stable hexagonal lattice. Marked clusters correspond to the same cluster of filaments at different times, indicating that clusters occasionally interchange sites on the lattice.

an interchange, the clusters retain their identity.

When studying systems of filaments with both signs of intensity, the box-loading technique does not satisfactorily produce negative energies. In order to obtain starting configurations with a particular desired energy, we employ a Monte-Carlo procedure. The filaments are given random positions, and individual filament positions are proposed. If the proposed configuration has energy closer to the target energy than the present configuration, the proposal is accepted. When the energy falls within an accepted range of the target energy, the positions are saved and become the initial conditions of the dynamic simulation. The systems are thus well-randomized at the beginning of the simulation, and need not be run for so long a time to obtain acceptable statistics.

A time history of the value of H is shown in figure 5.8 for four separate runs, the first with 1024 filaments on a 32^2 grid, the second with 4096 on 32^2 , the third with 1024 on 8^2 , and the last with 1024 on 64^2 . The numerical algorithm conserves the Hamiltonian best on the 8×8 grid, where the density of filaments is greatest, and worst on the large grid, with a low filament density. Figures 5.9, 5.10, and 5.11 show time histories of E^u , E^w , and A in the same format for the same runs. Interestingly, these other quantities, which are strict invariants under the continuous MHD fluid equations, simply fluctuate about a constant value in this approximate system. There is no net degradation or increase in the total energy, cross-helicity or mean-squared flux. This supports even further the contention that a u - w filament system even in which the source S is ignored still serves as an acceptable statistical model for MHD turbulence.

Energies down to ~ 1 are still large enough to show structure, even though the clustering of filaments represented by this is not visible from phase-space plots. Figure 5.12 shows contour lines of the magnetic and velocity fields from a run with $\tilde{E} = 2$. Typical spectra at a single time-step and averaged

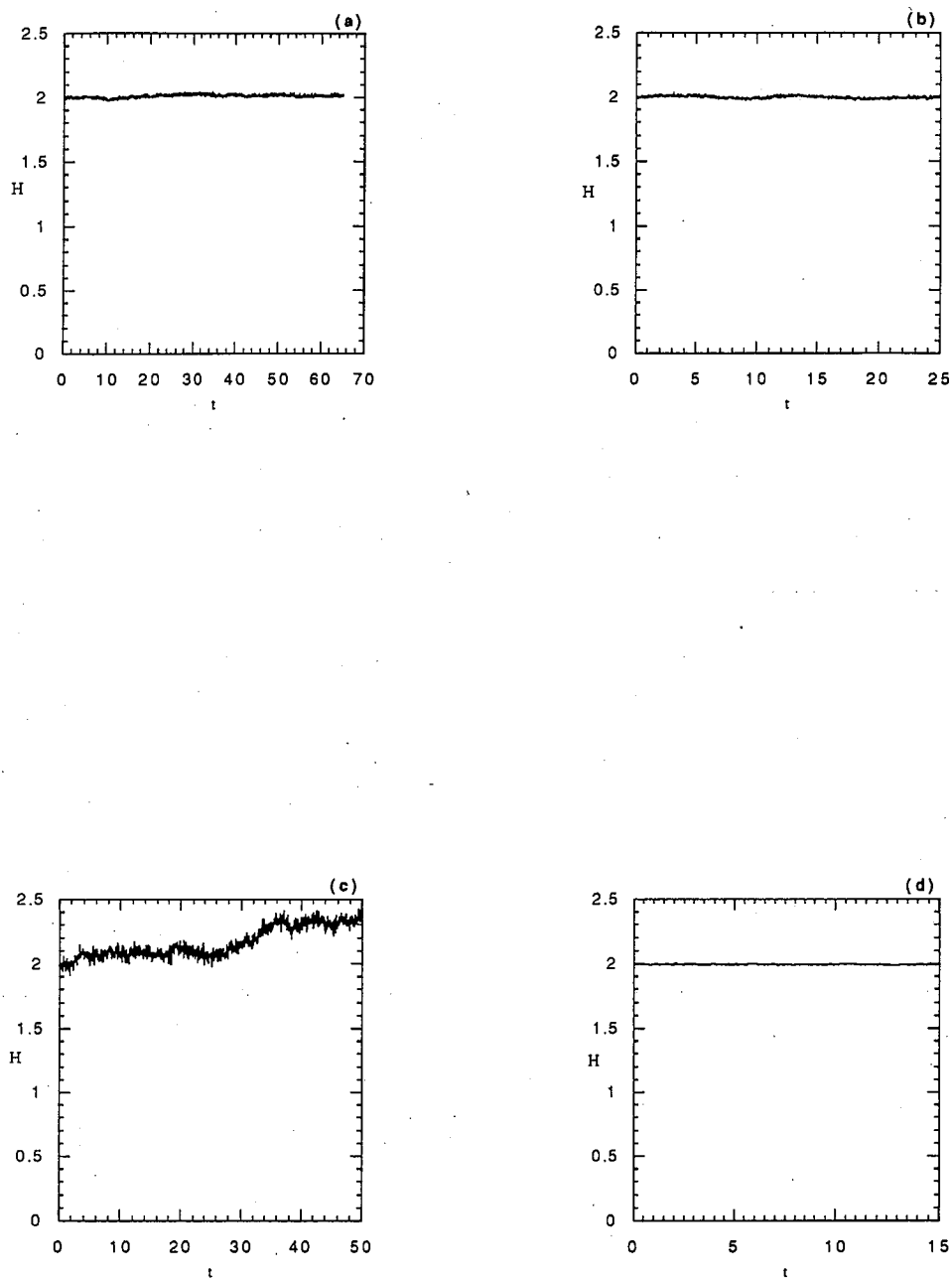


Figure 5.8: Time histories of H for four separate runs with filaments-per-cell of (a) 1, (b) 4, (c) 1/4, and (d) 16.

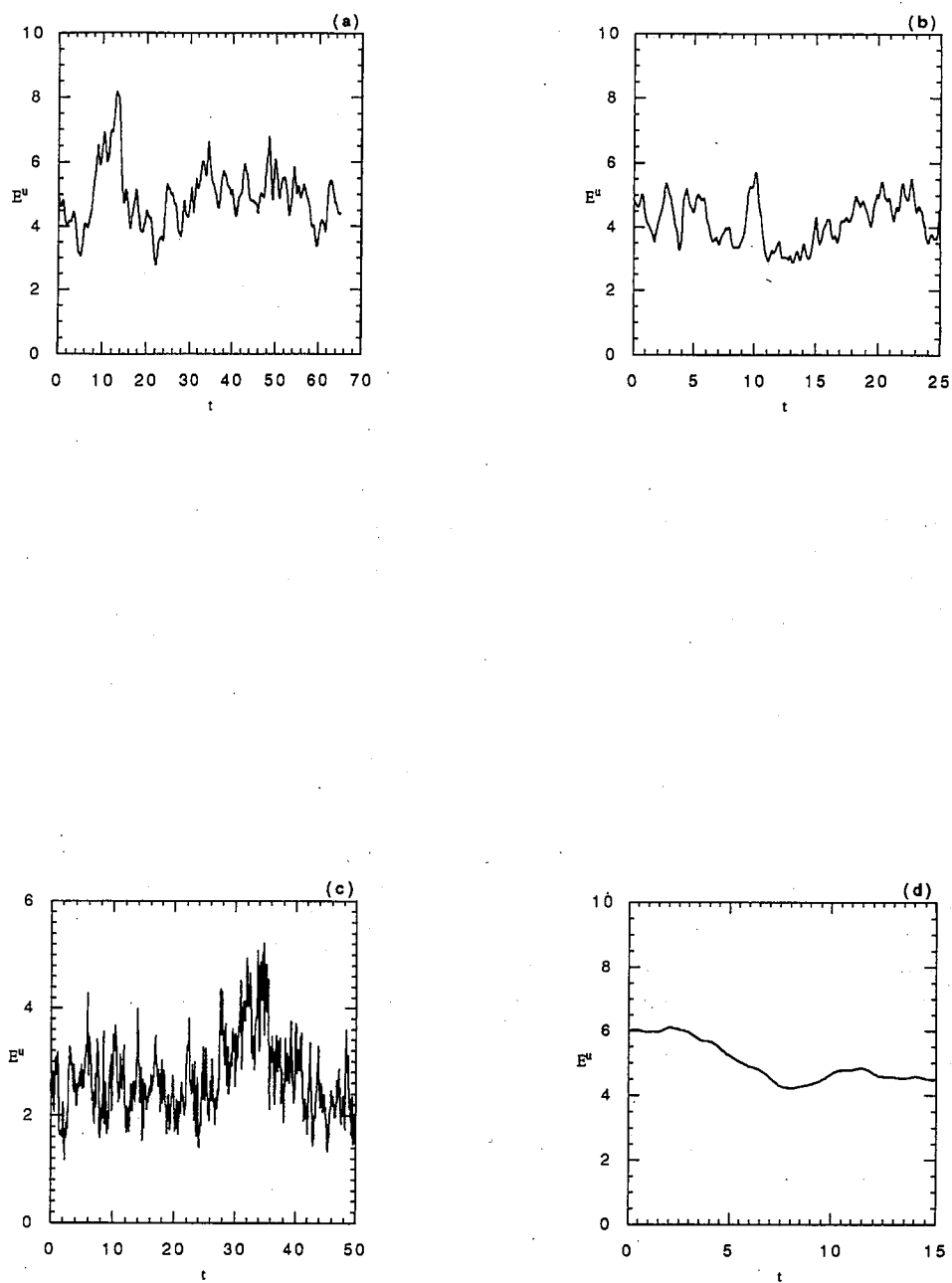


Figure 5.9: Time histories of E^u for the same runs as in the previous figure.

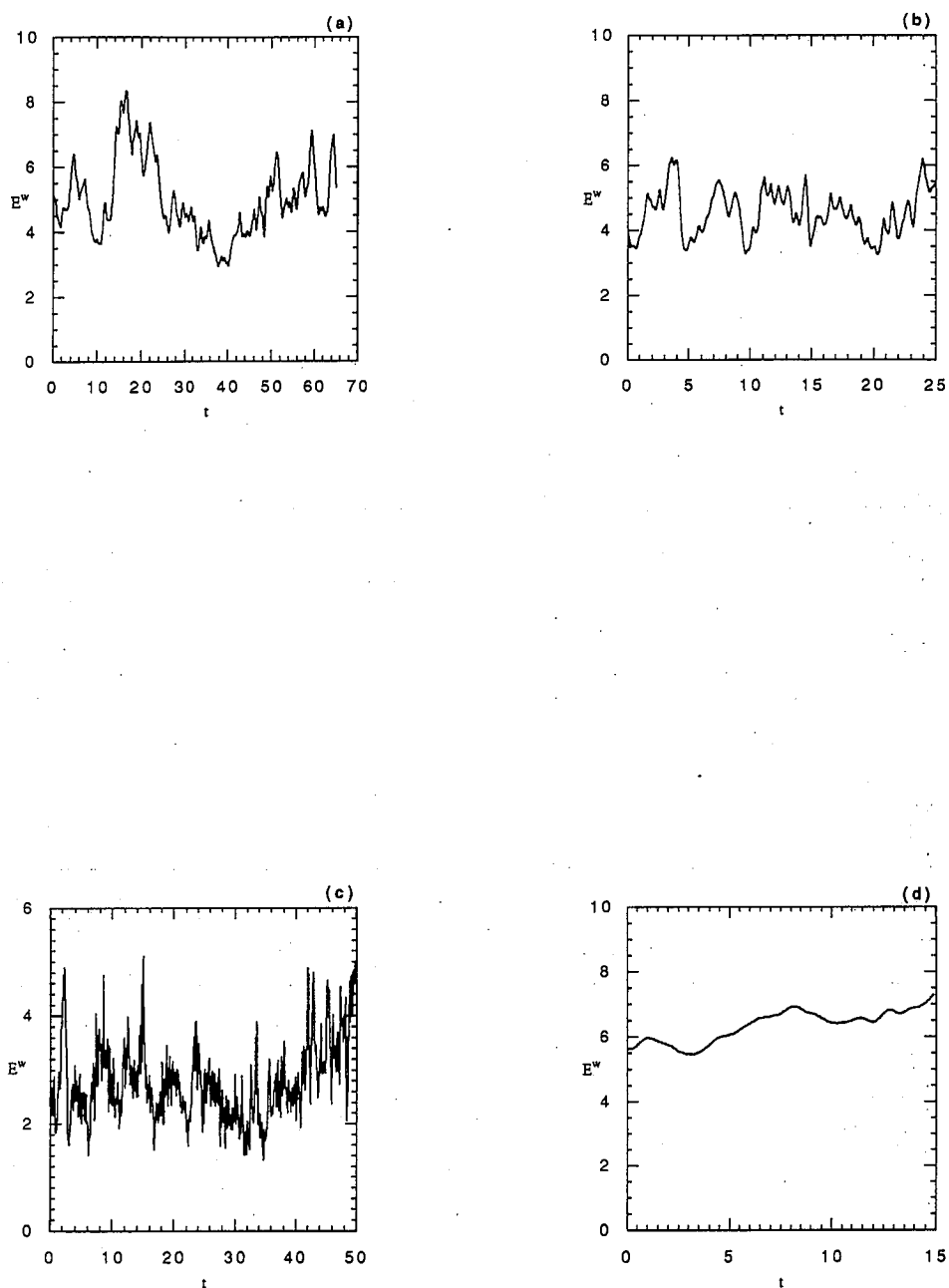
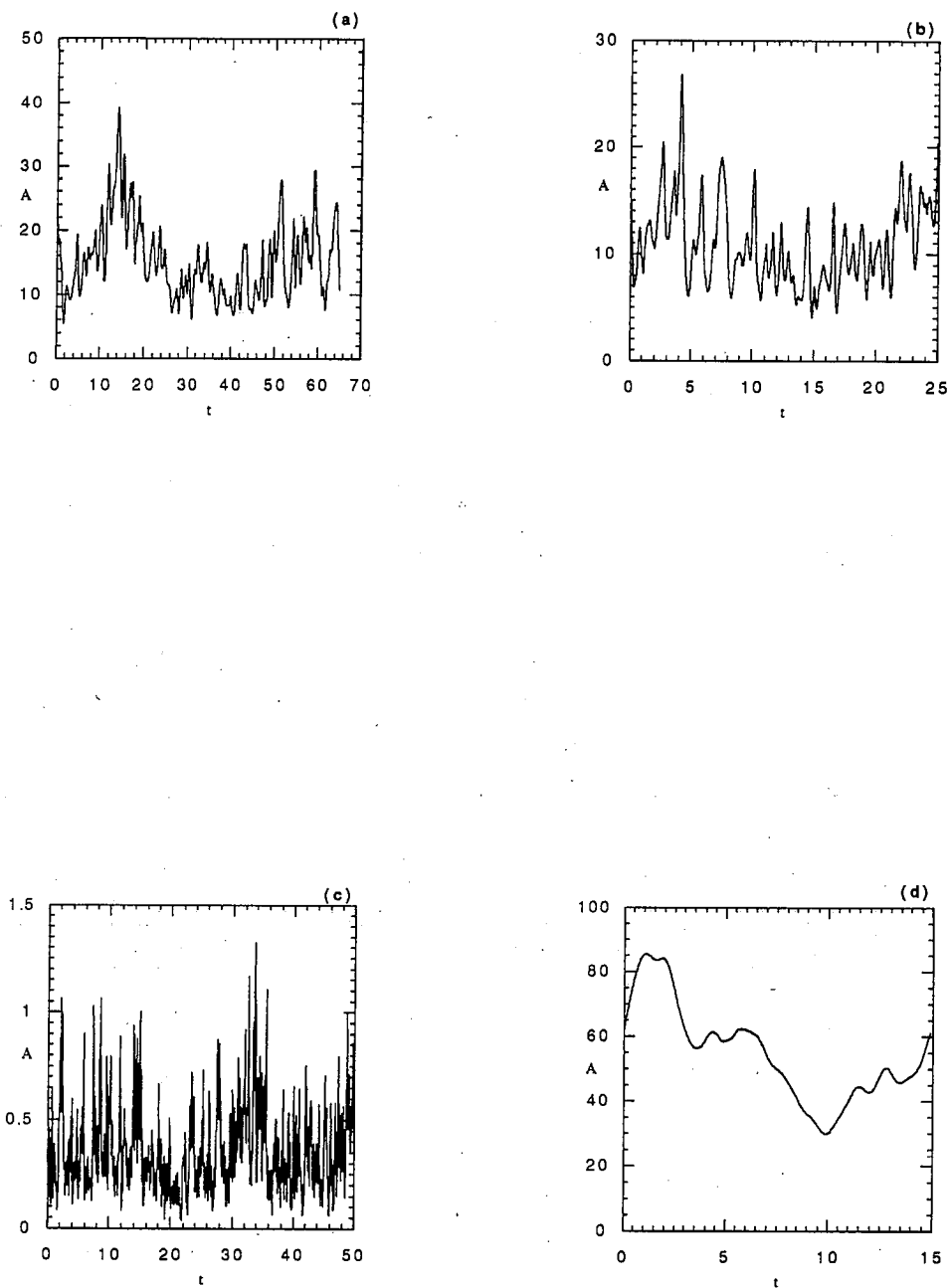


Figure 5.10: Time histories of E^w .

Figure 5.11: Time histories of A .

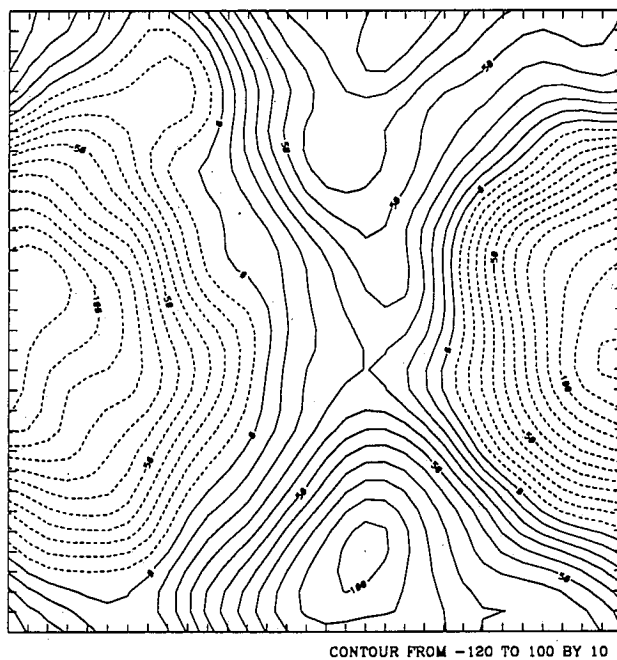
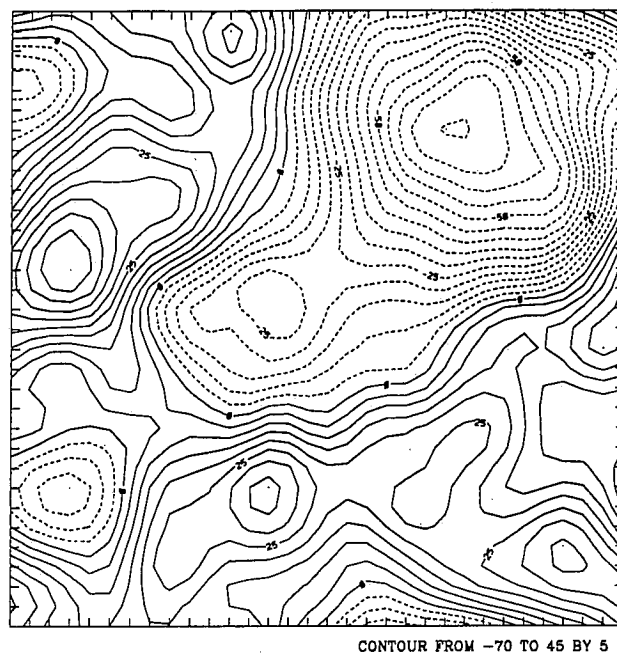


Figure 5.12: A_z and Ψ contours during $\tilde{E} = 2$ run.

through the simulation are shown in figure 5.13. The solid line is the theoretical spectrum from the micro-canonical ensemble, as calculated in the previous chapter. Note that there is some evidence that the trajectories of neutral-fluid vortices are not entirely ergodic [67], although the non-ergodicity appears to be weak [68]. In our case, time-averaged quantities seem to correspond well with the micro-canonical ensemble averages.

As mentioned before, reversing the sign of the Hamiltonian should simply interchange the fields v and B . Shown in figure 5.14 are spectra for a simulation run with $\tilde{E} = -1$. The same correspondence with theory is shown, this time with the magnetic energy spectrum exhibiting long-wavelength structure. Finally, figure 5.15 shows the values of the lowest wavenumber modes, $\omega^2(k_{\min})$ and $j^2(k_{\min})$, as a function of \tilde{E} . The asymptotic behaviors $\langle \omega^2 \rangle \propto \tilde{E}$ and $\langle j^2 \rangle \rightarrow \text{const.}$ are clearly demonstrated.

A number of runs were also carried out with $S \neq 0$, that is, with the filament strengths changing in time according to the inductive force. As mentioned, there is inherent numerical diffusion in our algorithm due to the finite size of the computational filaments. Figures 5.16 and 5.17 show time histories of the putative invariants E^u , E^w , A , and the former Hamiltonian H , and the time-averaged spectra of ω^2 and j^2 . The energies decay away due to the diffusion, but H remains relatively constant. This makes sense to some extent, for if the ohmic and resistive decay rates are comparable, the kinetic and magnetic energies should both decay at the same, and H , the difference between the two, will remain roughly constant. The diffusion at small length scales changes the form of the spectra at short wavelengths, falling off as κ^{-2} rather than approaching a constant. The values of the longest-wavelength modes, however, continue to agree with theoretical predictions.

The numerical diffusion of our scheme can be compensated for by adding an artificial small correction to the source S . This correction ensures that E^u

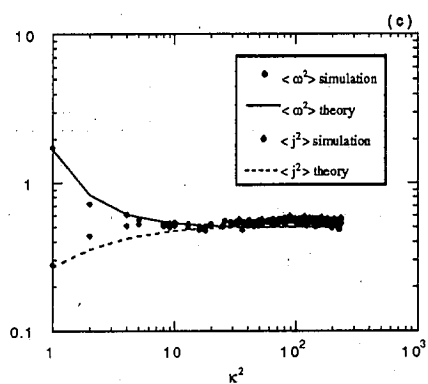
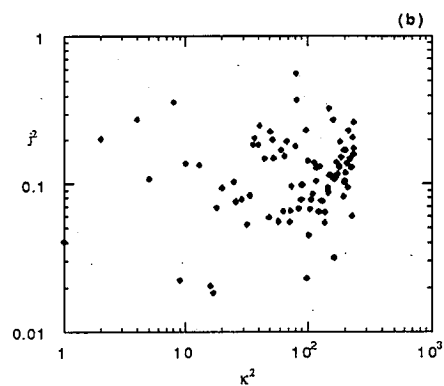
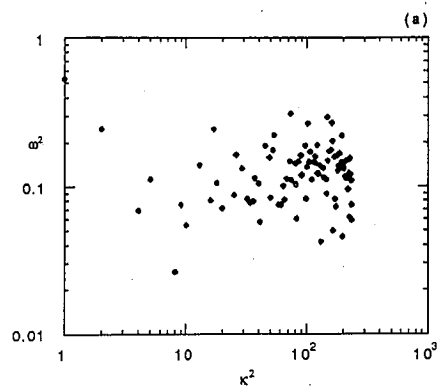


Figure 5.13: Current and vorticity spectra (a) at a single time-step and (b) averaged over 2000 time steps. $\bar{E} = 2$.

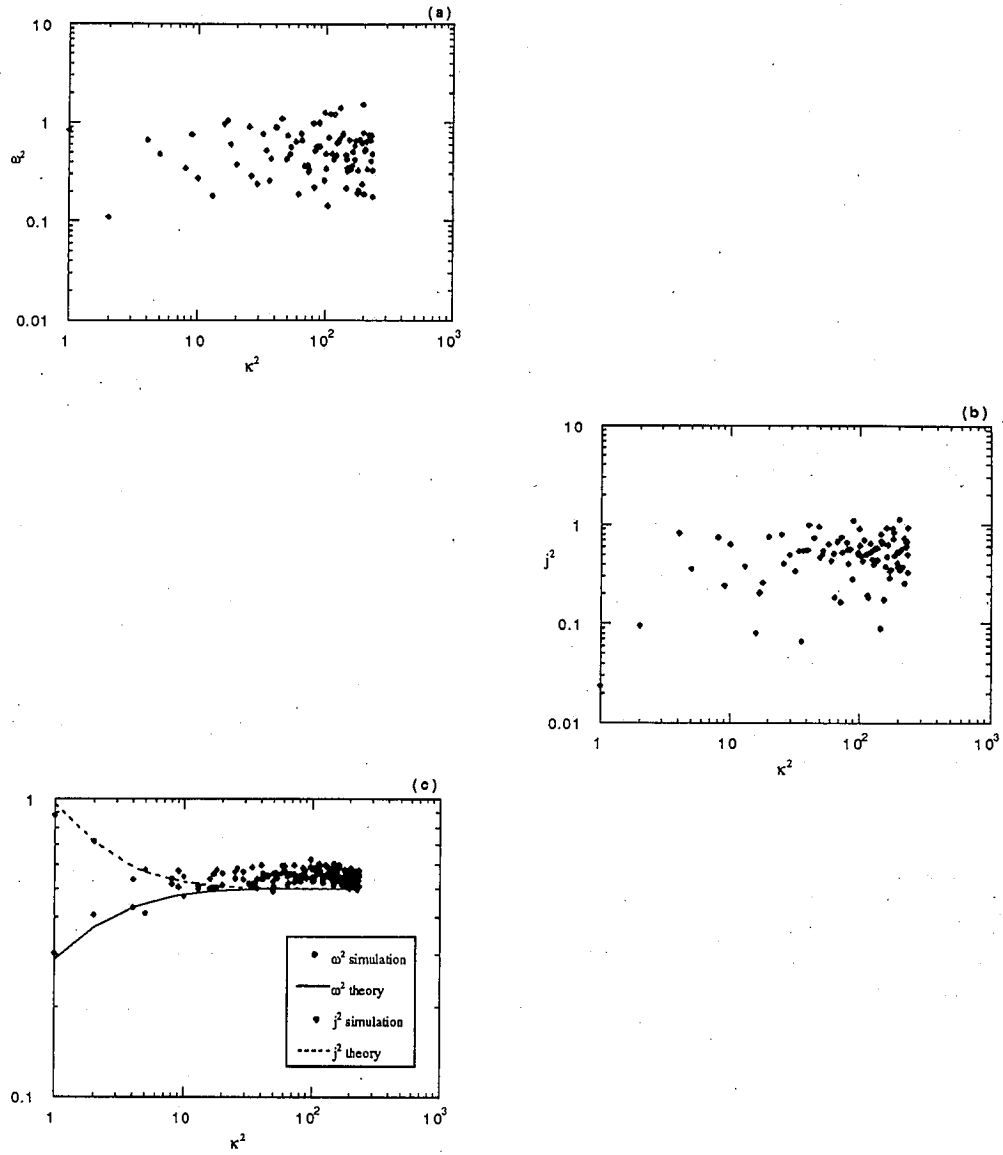


Figure 5.14: Current and vorticity spectra (a) at a single time-step and (b) averaged over 2000 time steps. $\bar{E} = -1$.

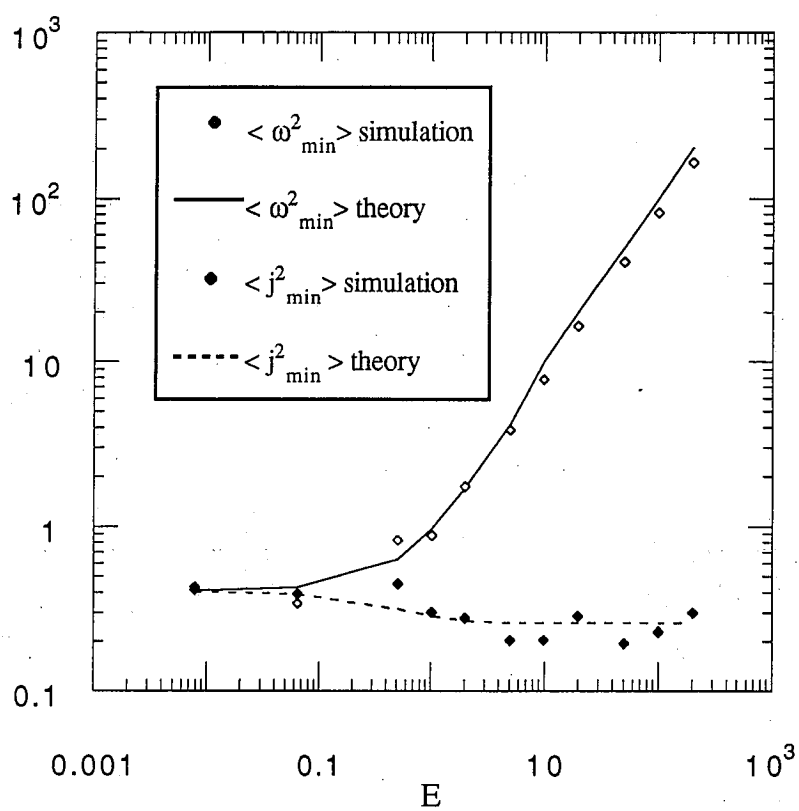


Figure 5.15: Values of the minimum k mode of ω^2 and j^2 from a series of simulations, compared with theory.

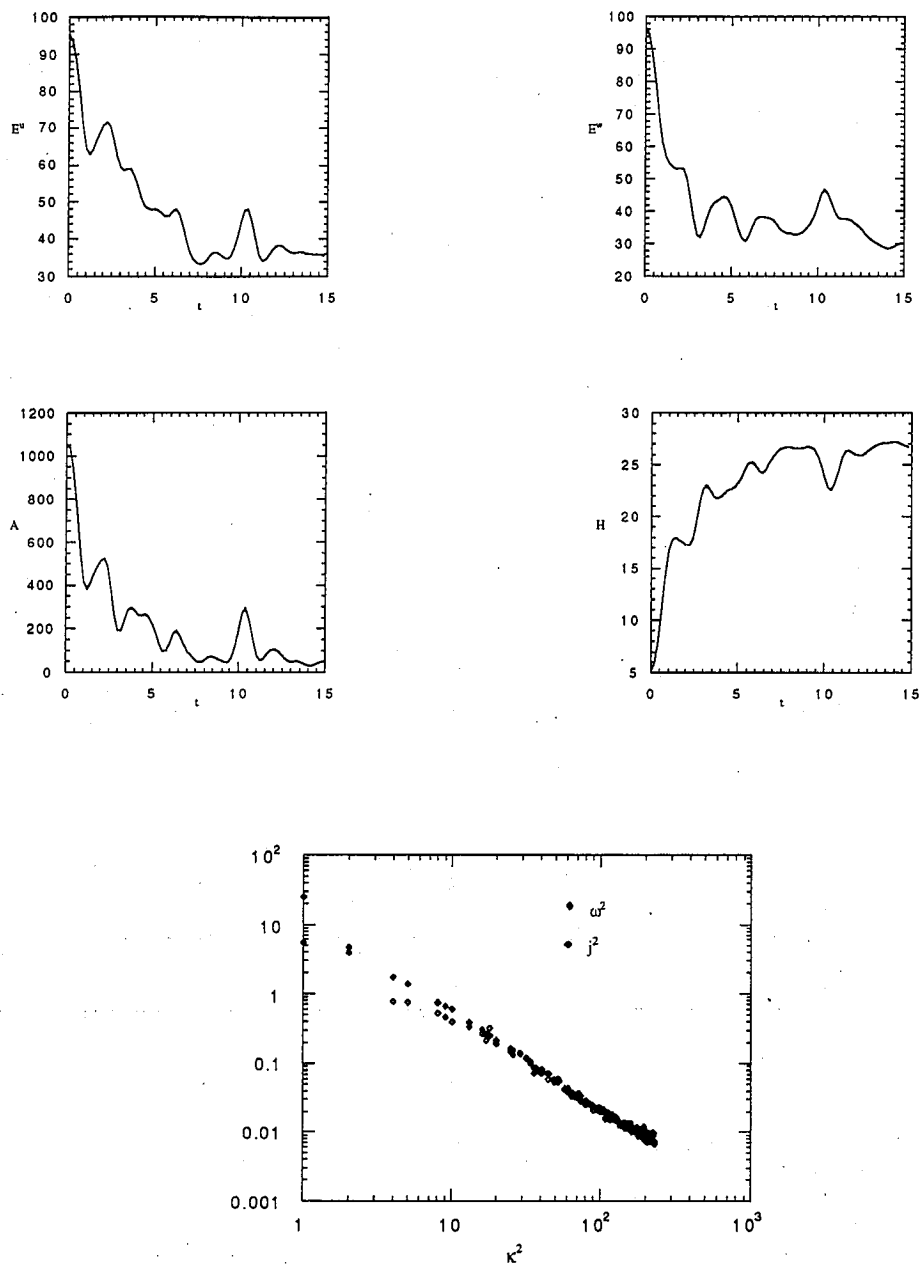


Figure 5.16: Time histories and spectra for velocity-dominated $S \neq 0$ run. Diffusion leads to a decay of the invariants and a $1/k^2$ spectrum at large k . Small k values agree with $S = 0$ theory based on average value of H .

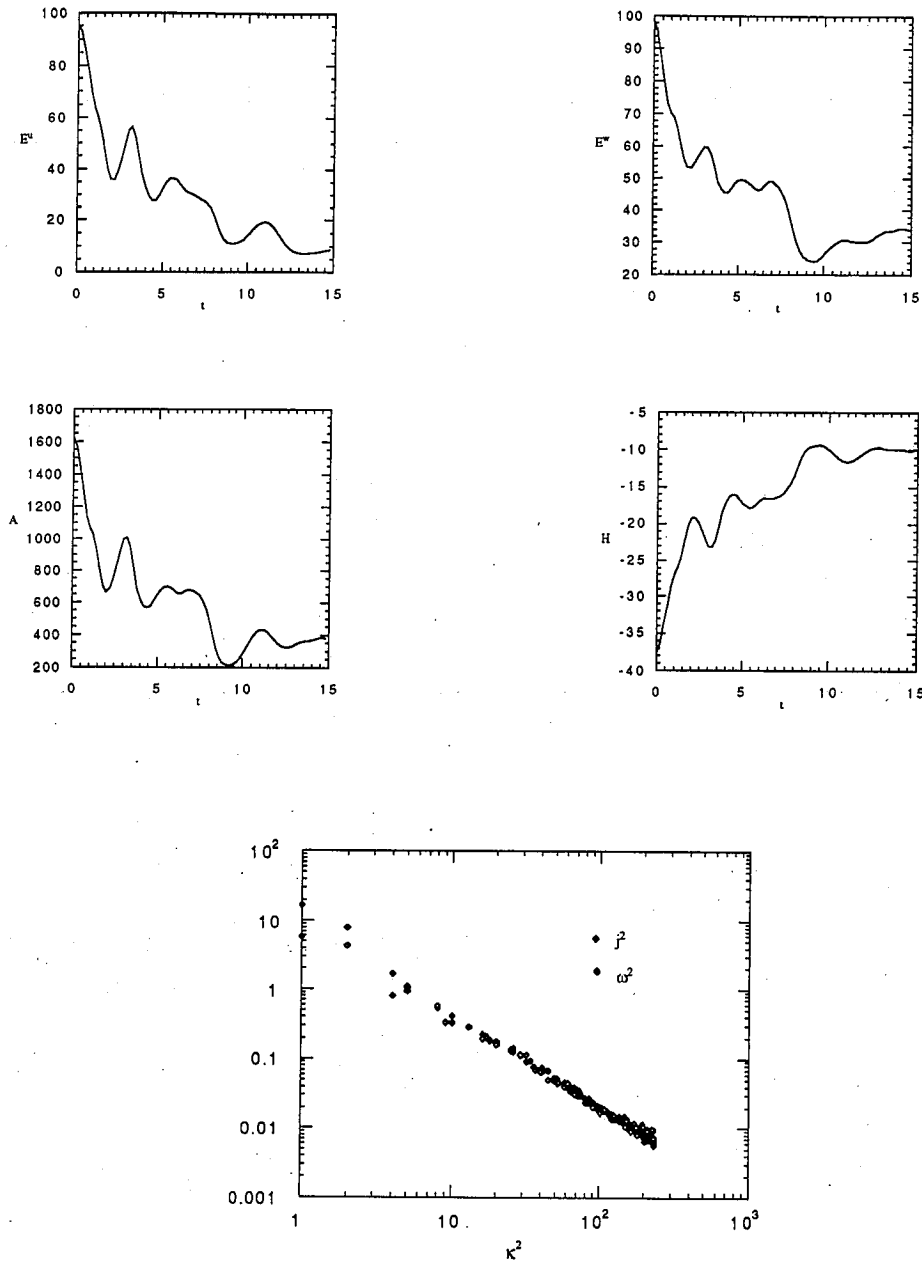


Figure 5.17: Time histories and spectra for magnetically-dominated $S \neq 0$ run. As in the previous figure, diffusion alters the large- k spectrum, but the long wavelength behavior agrees with $S = 0$ theory.

and E^w will stay constant, although A remains unconstrained. Results from a pair of such runs are presented in figures 5.18 and 5.19. The values of A and H do not systematically decay in these cases either. The spectrum, lacking the drain on small-scale modes, flattens out for large κ , and displays long-wavelength behavior consistent with the theoretical predictions.

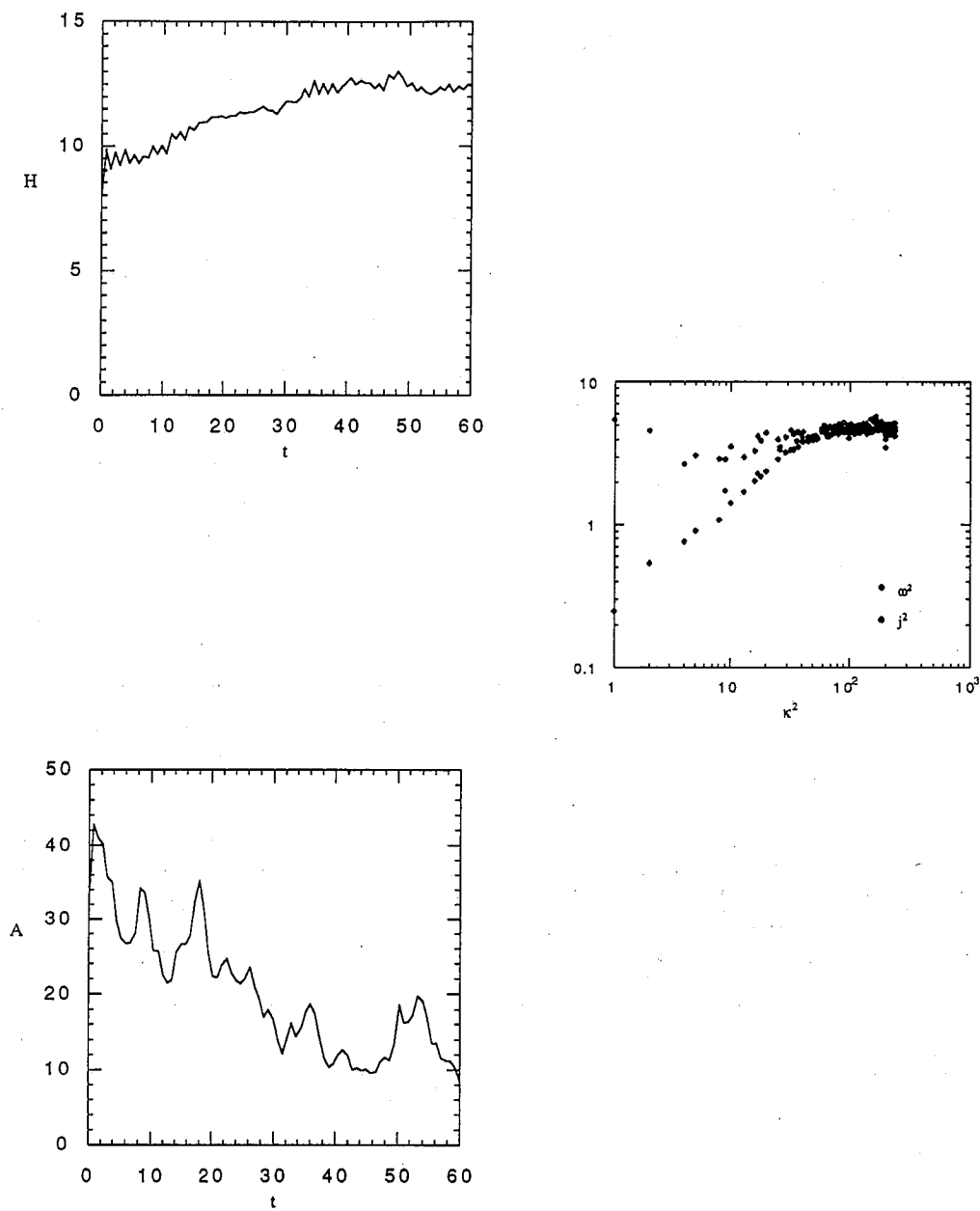


Figure 5.18: Time histories and spectra from velocity-dominated run with diffusion compensated for. Spectra show shape and asymptotic behavior consistent with theory.

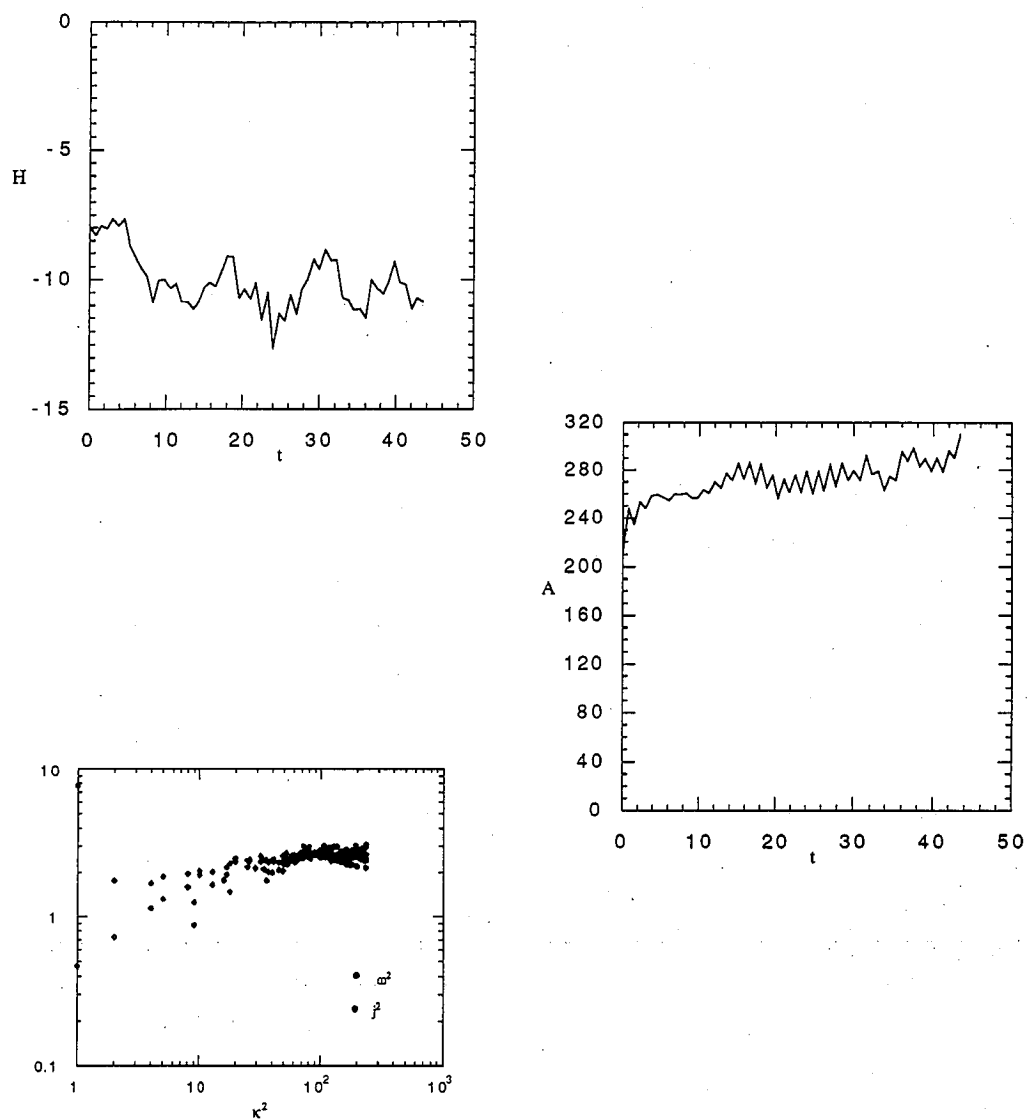


Figure 5.19: Time histories and spectra from magnetically-dominated run with diffusion correction.

Chapter 6

Filamentary Objects in Three Dimensional MHD Turbulence

Three-dimensional MHD turbulence can be expected to have organizational properties similar to two-dimensional turbulence, due to the fact that there are still more than one quadratic invariant of the field equations. One loses $\int A_z^2 d^2x$ but gains $\int \mathbf{A} \cdot \mathbf{B} d^3x$. In neutral fluids with low dissipation, intense intermittency is beginning to be observed in laboratories [69] and simulations [70, 71, 72] under general conditions. General filamentary objects [73, 74] are also being studied with adapted computational models [75, 76], and are meeting with success.

In three dimensions, the computational advantage of this approach is even greater than in two dimensions. Given a system in which strongly intermittent structures are present, the spatial resolution required to resolve the swirls and eddies of a large three-dimensional system is an especially great burden on present-day machines and techniques. In contrast, when modeling vortex filaments as discrete objects, all fluid information is contained within the filament positions, so there is no need to resolve spatial scales as finely. Reducing the size of the problem is especially important in higher dimensions.

Fourier-based investigations of three-dimensional MHD turbulence [77, 78, 79] have predicted invariant spectra which are peaked at the maximum wavelength, and predictions were confirmed in numerical simulations. The

treatment here is less detailed than the two-dimensional presentation, concentrating on outlining a vortex-based numerical scheme, and presenting some qualitative results of simulations.

6.1 Isolated Current-Vorticity Distributions

A general description of singular u -type and w -type filaments parameterizes the vorticities in terms of curves $\mathbf{q}(s, t)$:

$$\begin{aligned}\Omega^u(\mathbf{x}, t) &= \sum_i \alpha_i^u \int \mathbf{q}_i'^u \delta(\mathbf{x} - \mathbf{q}_i^u(s, t)) ds \\ \Omega^w(\mathbf{x}, t) &= \sum_j \alpha_j^w \int \mathbf{q}_j'^w \delta(\mathbf{x} - \mathbf{q}_j^w(s, t)) ds,\end{aligned}\tag{6.1}$$

where the prime indicates differentiation with respect to the curve parameter s . The fields may be decomposed,

$$\begin{aligned}\mathbf{u} &= \mathbf{u}_p + \mathbf{u}_t + \mathbf{u}_0 \\ \mathbf{w} &= \mathbf{w}_p + \mathbf{w}_t + \mathbf{w}_0,\end{aligned}\tag{6.2}$$

into a poloidal component,

$$\begin{aligned}\mathbf{u}_p(\mathbf{x}, t) &= \sum_i \alpha_i^u \int \frac{\mathbf{x} - \mathbf{q}_i^u(s, t)}{|\mathbf{x} - \mathbf{q}_i^u(s, t)|^3} \times \mathbf{q}_i'^u ds \\ \mathbf{w}_p(\mathbf{x}, t) &= \sum_j \alpha_j^w \int \frac{\mathbf{x} - \mathbf{q}_j^w(s, t)}{|\mathbf{x} - \mathbf{q}_j^w(s, t)|^3} \times \mathbf{q}_j'^w ds,\end{aligned}\tag{6.3}$$

plus a toroidal component,

$$\begin{aligned}\mathbf{u}_t(\mathbf{x}, t) &= \sum_i \beta_i^u \int \delta(\mathbf{x} - \mathbf{q}_i^u(s, t)) \mathbf{q}_i'^u ds \\ \mathbf{w}_t(\mathbf{x}, t) &= \sum_i \beta_i^w \int \delta(\mathbf{x} - \mathbf{q}_i^w(s, t)) \mathbf{q}_i'^w ds,\end{aligned}\tag{6.4}$$

plus background fields \mathbf{u}_0 and \mathbf{w}_0 . The toroidal field is non-zero only exactly on points that are on a vortex filament, and is only important when filaments overlap. One can comfortably take $\mathbf{u}_t = \mathbf{w}_t = 0$. Eq. (6.3), the Biot-Savart

law, can be solved in Fourier space given any set of filament curves. The fields may be interpolated to the filament positions, and used to advect them forward in time.

In this investigation, we will treat, rather than the extended structures of (6.1), a special case of such filaments, vortex distributions which are compact and localized. When the mean filament separation is large compared to the internal structure size, a turbulent MHD fluid may be represented as a collection of isolated u - w current-vorticity distributions which are advected by each other and whose strengths change according to some source.

Given the multipole expansions for a particular vortex,

$$A(\mathbf{x}, t) = \sum_{n=0}^{\infty} \frac{1}{n!} M_{i_1, \dots, i_n}^{(n)}(t) \frac{\partial^n}{\partial x_{i_1} \dots \partial x_{i_n}} G(\mathbf{x} | \mathbf{x}_i(t)), \quad (6.5)$$

with G the Green's function for Poisson's equation, fields of arbitrary specifications can be represented by suitably chosen distributions of point particles possessing internal degrees of freedom (the multipole moments).

The equations of motion of a u -particle are solved by

$$\begin{aligned} \dot{\mathbf{x}}^u &= \mathbf{w}(\mathbf{x}^u) \\ \dot{M}_{i_1, \dots, i_n}^{(n)} - (M_{i_1, \dots, i_n}^{(n)} \cdot \nabla) \mathbf{w}(\mathbf{x}^u) &= S, \end{aligned} \quad (6.6)$$

and similarly for w -filaments. The source term is unique only up to an additive gradient, because such a gradient added to the potentials does not actually change the fields. The source term again represents the induction of current in the advecting vortices, and will be neglected in the following treatment.

In three dimensions, the fundamental vortex object is the vortex ring, or point dipole. A treatment in terms of point dipoles for hydrodynamical turbulence was considered in [80] and [81]. In hydrodynamics, one must cope with the problem that a vortex loop moves under its own influence at a speed that scales inversely with the loop size. The problem of infinitely speedy rings

is not present in our system, since a loop does not self-interact. We treat here the case $S = 0$.

Our turbulent fluid is represented by the positions and dipole strengths of the vortices, i.e. by the $6N$ variables D_i and \mathbf{x}_i . Defining the “Dipole field” as

$$D^s(\mathbf{x}) \equiv \sum_i D_i^s \delta(\mathbf{x} - \mathbf{x}_i^s), \quad (6.7)$$

the field arising from the dipoles is given by

$$\mathbf{u}(\mathbf{x}) = D^u(\mathbf{x}) - \nabla \int D^u(\mathbf{x}') G(\mathbf{x}|\mathbf{x}') d\mathbf{x}'. \quad (6.8)$$

The filaments positions and dipole moments change according to

$$\dot{D}_i^u = -\nabla(D_i^u \cdot \mathbf{w})|_{\mathbf{x}_i^u}, \quad \dot{D}_i^w = -\nabla(D_i^w \cdot \mathbf{u})|_{\mathbf{x}_i^w}, \quad (6.9)$$

and can be derived from a Hamiltonian of the form

$$\begin{aligned} H(\mathbf{x}_1^u, D_1^u, \dots, \mathbf{x}_N^u, D_N^u) \\ = \sum_{i \in u} D_i^u \cdot \mathbf{w}(\mathbf{x}_i^u) = \sum_{j \in w} D_j^w \cdot \mathbf{u}(\mathbf{x}_j^w), \end{aligned} \quad (6.10)$$

where the \mathbf{x} 's are conjugate to the D 's such that

$$\dot{\mathbf{x}}_i = \frac{\partial H}{\partial D_i}, \quad \dot{D}_i = -\frac{\partial H}{\partial \mathbf{x}_i}, \quad (6.11)$$

and $\mathbf{u}(\mathbf{x})$ and $\mathbf{w}(\mathbf{x})$ are given by eq. (6.8). As in two dimensions,

$$H = \int \mathbf{u} \cdot \mathbf{w} = \int v^2 - B^2. \quad (6.12)$$

6.2 Canonical Ensemble

Let us adopt a mean-field approximation, in which

$$\mathbf{u} = \frac{4\pi N_u}{V} \langle D^u \rangle, \quad \mathbf{w} = \frac{4\pi N_w}{V} \langle D^w \rangle. \quad (6.13)$$

If we treat $\langle D^u \rangle$ as a given constant and consider D^w a variable, our partition function is

$$Z = \left[\int e^{\frac{-4\pi N_u \langle D^u \rangle D^w}{VT}} dD^w \right]^{N_w}, \quad (6.14)$$

and we can find the mean relative orientation of the dipole fields by

$$-\frac{\partial \ln Z}{\partial (\frac{1}{T})} = \frac{4\pi N_u N_w}{V} \langle D^u \rangle \cdot \langle D^w \rangle. \quad (6.15)$$

Defining $D_{||}^w = D^w \cdot \langle \hat{D}^u \rangle$, note that

$$\langle D_{||}^w \rangle = |\langle D^w \rangle|. \quad (6.16)$$

Let us fix the magnitude of a single dipole at D^w , and integrate only over the relative orientation to obtain

$$\langle D_{||}^w \rangle = D^w F \left(\frac{4\pi N_u |\langle D^u \rangle| D^w}{VT} \right) \quad (6.17)$$

with

$$F(x) = \frac{e^x(x-1) + e^{-x}(x+1)}{x(e^{-x} - e^x)} = \frac{1}{x} - \coth x. \quad (6.18)$$

An identical calculation in which $\langle D^w \rangle$ is fixed gives

$$\langle D_{||}^u \rangle = D^u F \left(\frac{4\pi N_w |\langle D^w \rangle| D^u}{VT} \right). \quad (6.19)$$

This result is similar to the expected orientation of a system of magnetic dipoles. In that case, the parallel component solves $D_{||} = F(\beta D_{||})$. When the temperature drops below the Curie point, this equation acquires a non-zero solution, and the dipoles align themselves. Our solution is of the form $D_{||} = F(\beta_1 F(\beta_2 D_{||}))$. There is likewise a critical temperature below which non-trivial solutions exist, $T_c = \frac{4\pi}{3} D^u D^w \sqrt{N_u N_w} / V$, as shown in figure 6.1. The dipoles in these solutions align themselves, with u 's anti-parallel to w 's. This is the minimum energy state, because it aligns the magnetic moments, but cancels the kinetic energy that the dipoles carry.

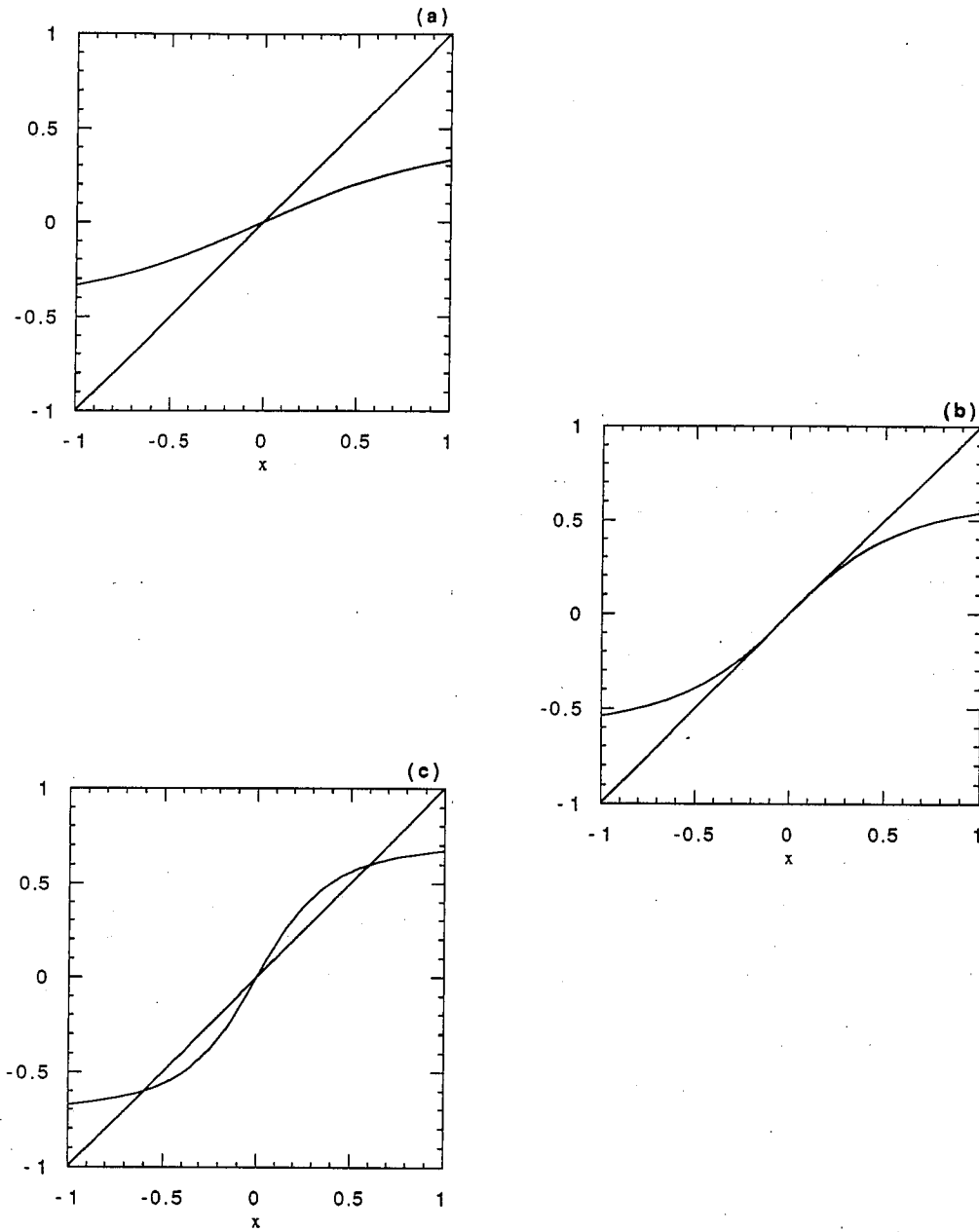


Figure 6.1: Graphical solutions of $x = F(\beta F(\beta x))$ for (a) $\beta = 2$, (b) $\beta = 3$, and (c) $\beta = 4$.

6.3 Numerical Study

A particle-in-cell code can also be used to study this system in three dimensions. In this case, we accumulate the dipole density $\mathbf{D}(\mathbf{x})$ as defined in (6.7) from the particles to a grid, and calculate the fields in Fourier space:

$$\mathbf{u}(\mathbf{k}) = 4\pi\mathbf{D}^u(\mathbf{k}) - 4\pi\mathbf{k}\frac{\mathbf{D}^u\cdot\mathbf{k}}{k^2}. \quad (6.20)$$

Chefranov [80] produced some exact solutions for two-dipole hydrodynamical systems, which is identical to a u - w system with one dipole of each type and $S = 0$. We use these solutions as test cases for the three-dimensional code. The two dipoles have equal and opposite magnitudes \mathbf{D} , separated by the vector \mathbf{r} , both of which lie in the x - y plane. The angle between these two vectors, ϕ , determines the character of the solutions. For $\cos^2 \phi < 1/3$, the dipoles approach along a logarithmic spiral, while for $\cos^2 \phi > 1/3$, the two dipoles move away, their strengths growing without limit with $|\mathbf{D}| \propto t^{3/5}$. The solutions are indeterminate when the dipoles coincide, so there is no prediction of what the state of the dipoles will be after the collision.

The predictions we compare with are that, given the value of the Hamiltonian, H ,

$$\begin{aligned} \frac{d}{dt}\mathbf{D} \cdot \mathbf{r} &= \text{const.} = 5H \\ \frac{d}{dt}r^5 &= \mathbf{D} \cdot \mathbf{r}. \end{aligned} \quad (6.21)$$

Figures 6.2 and 6.3 shows plots of $\mathbf{D} \cdot \mathbf{r}$ and r^5 for two different cases, the first case the degenerate solution in which \mathbf{D} and \mathbf{r} are parallel and the dipoles approach along a straight line, and the second a spiral collapsing case, $\cos \phi = 0$. When approaching along a straight line, the dipoles simply move through one another, but in the spiraling cases, the dipoles appear to interact and scatter almost as soon as they are within each others' Gaussian core, moving outward along a different expanding path.

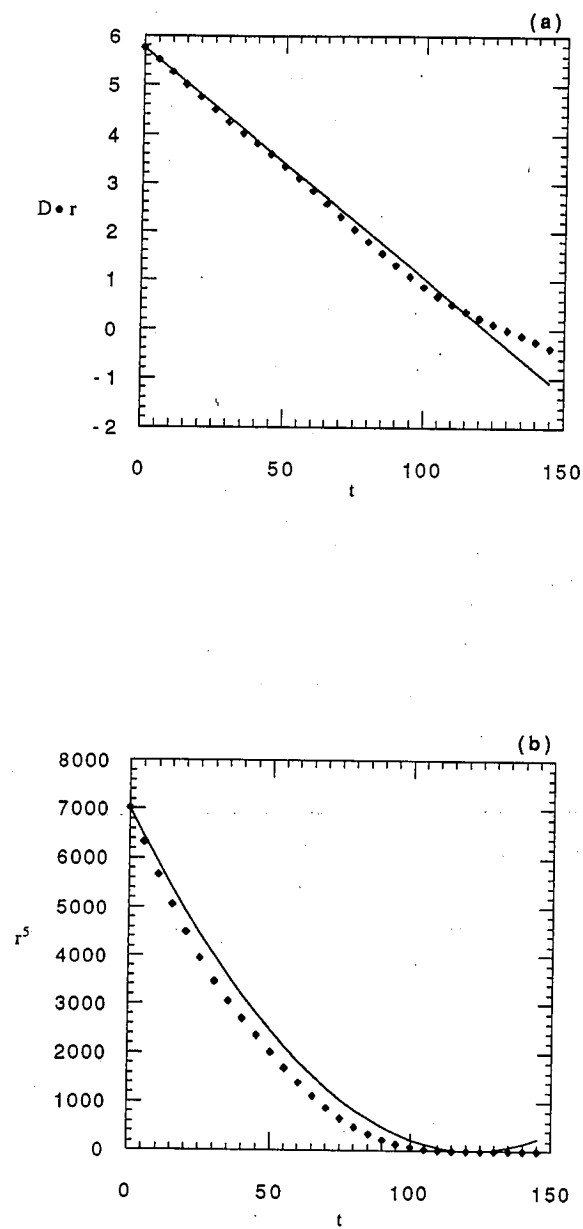


Figure 6.2: Plots of $D \cdot r$ and r^5 for dipoles collapsing along a line.

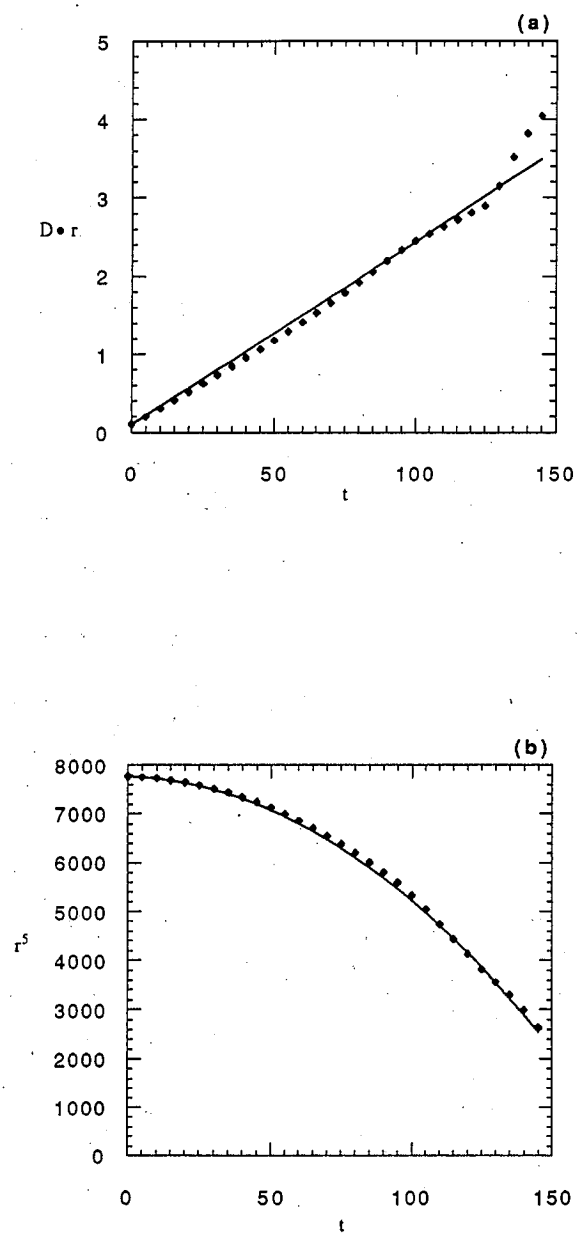


Figure 6.3: Plots of $D \cdot r$ and r^5 for dipoles collapsing along a spiral.

We have run this system for 4096 dipoles of each species in a 16^3 computational cube. Dipoles were placed on grid points, and given random orientations. From such uniform random initial conditions, the system always chose to evolve a net magnetic field by orienting the u -dipoles opposite that w -dipoles. Figure 6.4 shows time histories of D^s , the sum of dipole vectors for each species. The mean dipole strengths of the two species mirror each other, growing in opposite directions. The mean alignment angle, $\langle \cos \theta \rangle \equiv \langle \hat{D}^u \rangle \cdot \langle \hat{D}^w \rangle$, for these three runs are shown in figure 6.5. The angle approaches π , indicating the net alignment of u and w dipoles pointing in opposite directions.

A glance at eq. (6.6) shows that there is the potential for exponential growth of a dipole in a suitable field. Indeed, two dipoles aligned opposite each other will move directly away from each other, and the magnitude of the dipole moments will grow in time without limit. This produces some computational hazards once the dipoles have aligned themselves. To study the behavior of dipoles which begin aligned, we conduct numerical runs in which a dipole is allowed to change its orientation, but not its magnitude. These runs begin with u dipoles oriented randomly within a cone pointing in the $+\hat{z}$ direction, w dipoles similarly oriented around $-\hat{z}$. This configuration corresponds to a mean magnetic field in $+\hat{z}$ with no net motion of the fluid.

Figures 6.6 and 6.7 show the computational volume of these fixed-magnitude runs. The initial magnetic field is generally vertical. Plotted in this volume are surfaces on which $B^2 = 0.7B_{\text{max}}^2$. Stronger fields are present within the volume defined by this surface. Initially, B^2 is within 30% of the maximum throughout nearly the entire computational volume. The general attraction between oppositely-aligned dipoles brings u and w dipoles together, and the magnetic field becomes more localized. Finally the magnetic field becomes dominantly concentrated into a vertical column. These structures live for a time and then decay away.

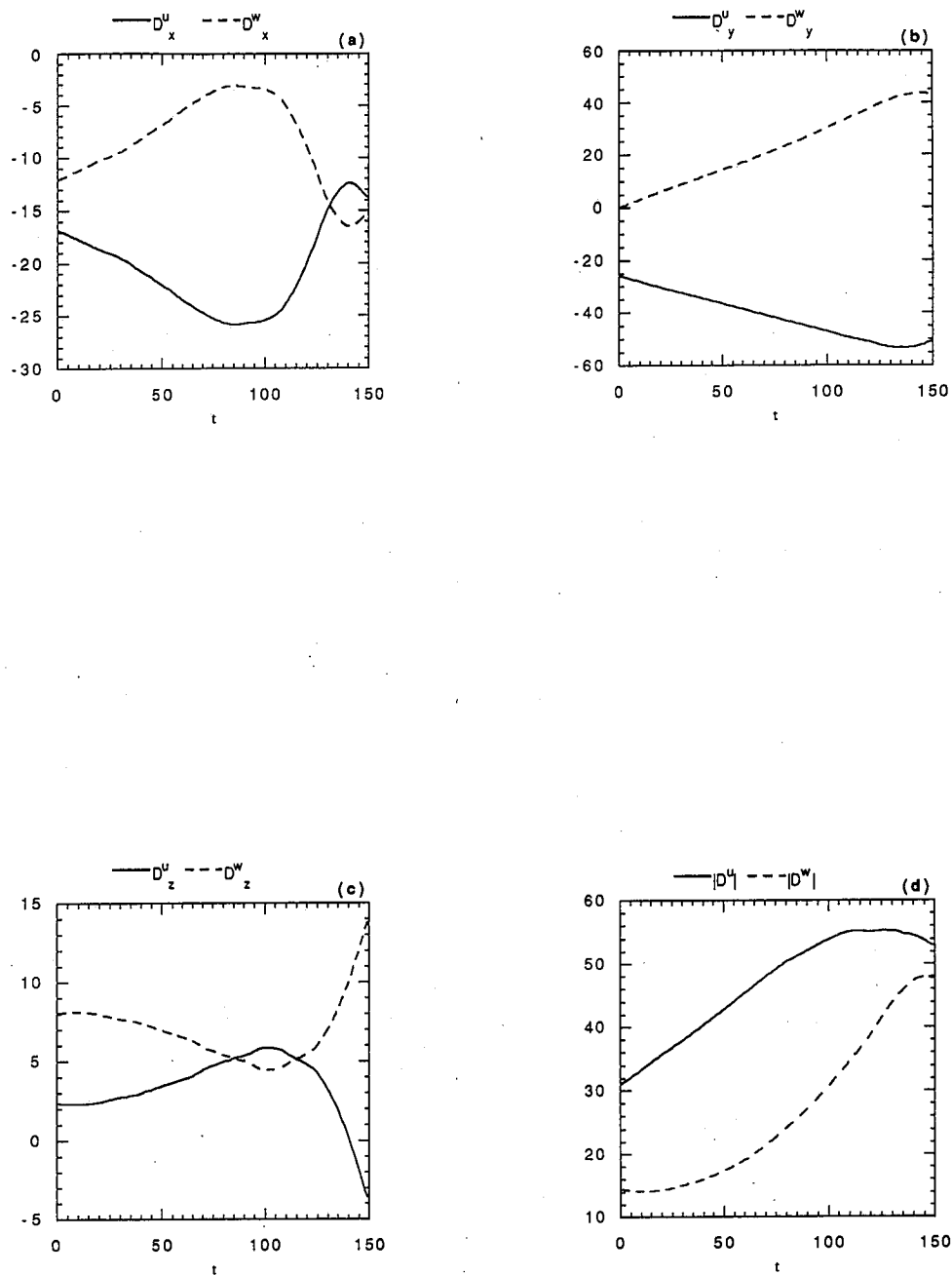


Figure 6.4: Time histories of the spatial components (a-c) and the magnitude (d) of the total dipole strengths of the u and w fields. Initial conditions are random, from which the two fields grow in opposite directions, generating a magnetic field.

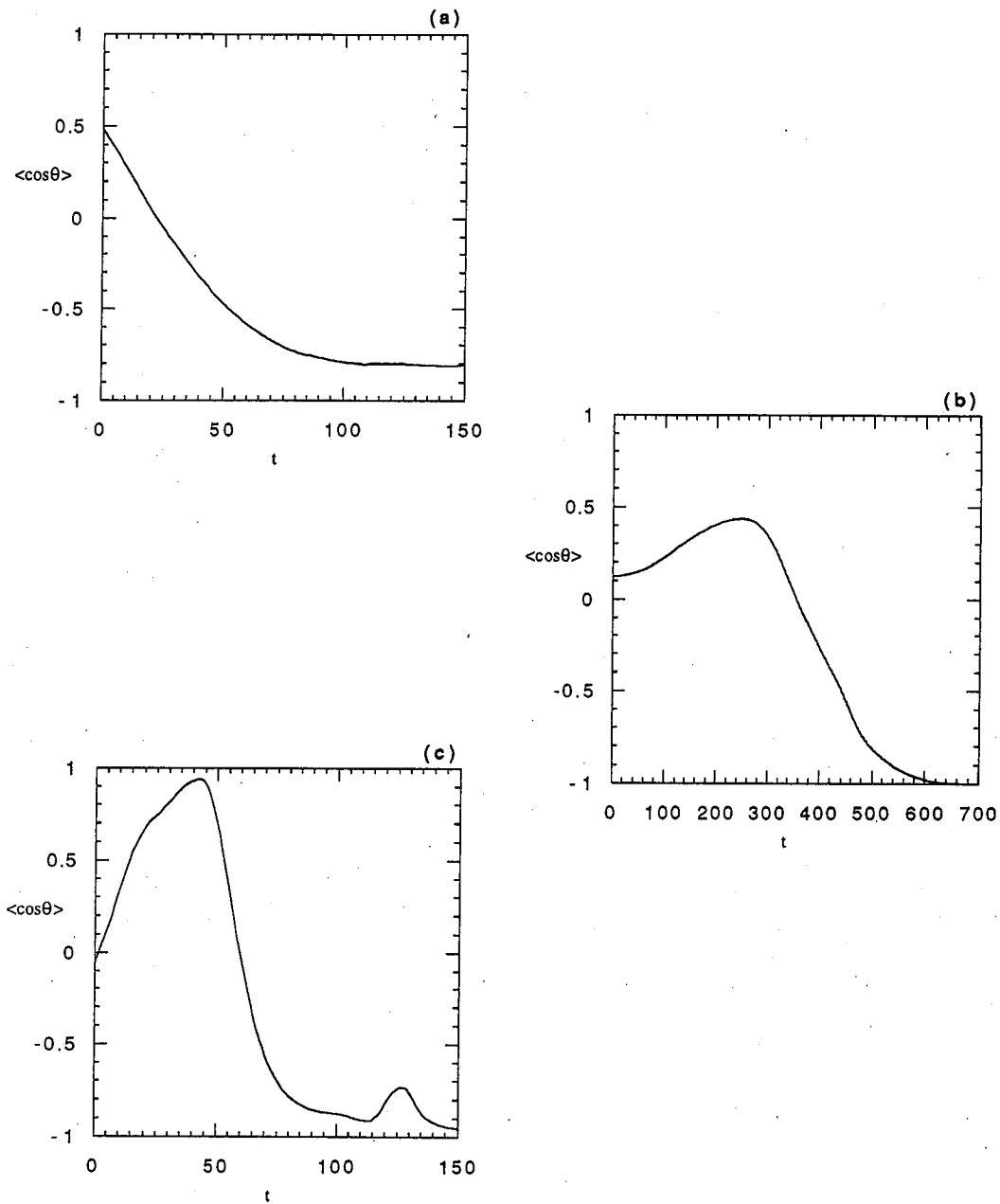


Figure 6.5: Time history of mean alignment angle between u and w fields for three separate runs with different random initial conditions.

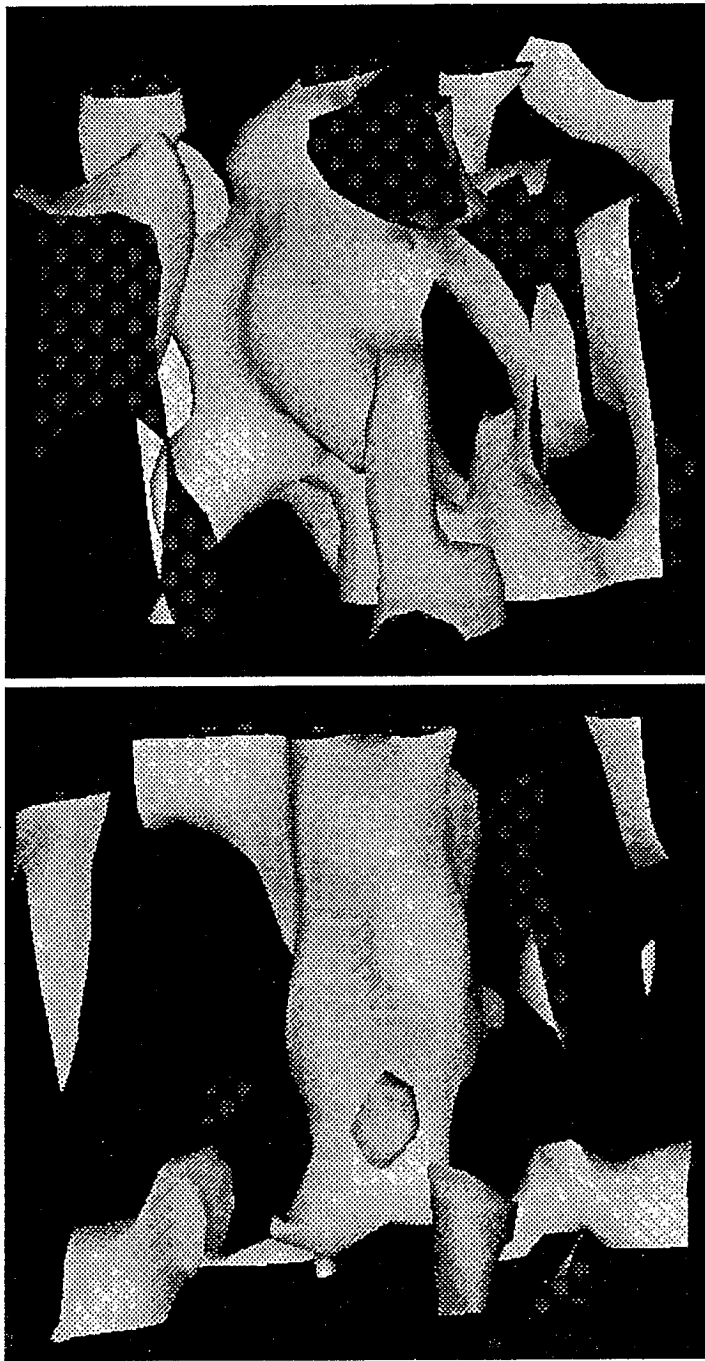


Figure 6.6: Surfaces of constant B^2 for fixed dipole magnitude run (a) at initial time and (b) as the field begins to organize.

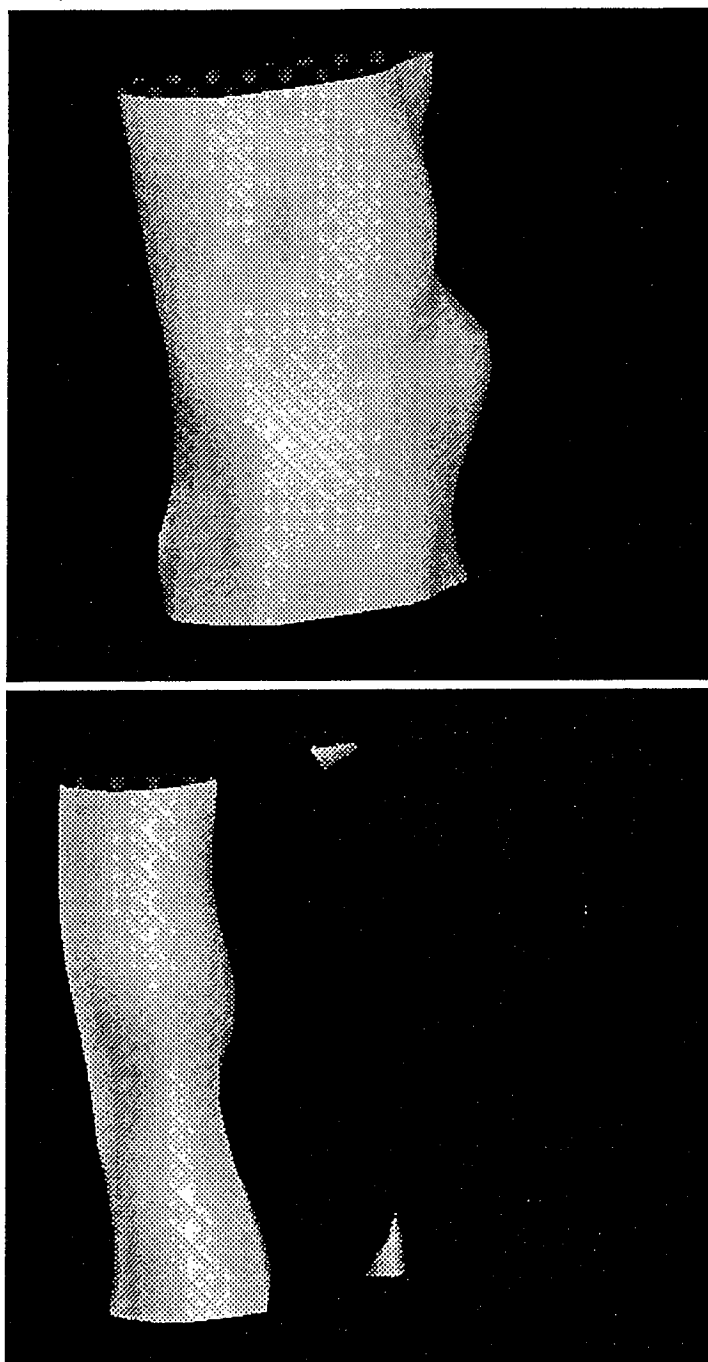


Figure 6.7: Continuation of the run from the previous figure, showing organization of magnetic field into flux tubes.

Chapter 7

Overview

Decades of scientific study of continuous non-linear systems have made plain that continuity implies anything but smoothness. Singularities seem always eager to form in fluids [69, 4], superfluids [3], condensed matter [82], and plasmas [83, 84, 85, 12, 15], and only dissipation can hold them back. Intermittencies in a plasma can be brought about not only by fluid motion, but by current running along stochastic magnetic field lines, as in an tokamak's "ergodic limiter" [86], or in coronal loops [87]. Intense intermittencies have profound effects on the dynamics of turbulence, but are not well represented by typical statistical theories based on a Fourier decomposition of the fluid variables.

It has been asserted [2] that different approaches to discretization of functional integrations cannot in general be expected to yield equivalent results. This could explain why Fourier-mode and point-vortex models of two-dimensional turbulence, while both making similar qualitative predictions, have not yielded results that correspond exactly even in their continuum limits. The mathematical inequivalence of a discrete system with countably infinite degrees of freedom and a continuous system with uncountably infinite degrees of freedom is ultimately responsible for the discrepancies, but until a suitable analysis framework for continuous systems is developed, a choice of discrete representations must be made, and that choice may ultimately rely on phenomenology.

We have shown that a point-vortex discretization like that of hydrodynamics is possible in general for MHD. The discrete-vortex model has spawned

a very wide variety of research (See Refs. [88, 89, 90, 91] for examples of avenues of analysis not expounded herein). Quantum-mechanically too, vortex lattices [92, 93] have received attention for their application to high-temperature superconductors [94, 95], as have “anyons” [96, 97, 98, 99], which can be interpreted as a charged particle attached to a magnetic flux tube. Given the great volume of research having to do with filamentary objects and vortices, a description of general MHD in terms of them seems increasingly natural.

In addition, computational constraints provide another motivation. Because of the tendency of high Reynolds-number neutral fluids to form small-scale vortical structures, a collection of discrete vortices can serve as a more economical representation of a turbulent fluid than a usual spectral code [57], and the fluid thus represented need not necessarily be inviscid. Taylor [100] has shown that the small-scale diffusive processes in a viscid fluid can be represented by a point-vortex model if the vortex strengths are chosen appropriately, and Carnevale et. al. showed that, with appropriately derived rules for close encounters between finite-size vortices [40], a discrete vortex model works well at representing a viscid fluid. Taking an analogous approach to MHD simulations could lead to similarly efficient numerical models of magnetic turbulence.

In constructing a statistical theory, careful account must be made of the invariants of the system’s evolution, as failing to account for one of the constants of the motion can completely alter the form of the expected states. For an ideal fluid, great care must be taken, for there are an infinite number of invariants of the motion, but most do not survive discrete truncation of the system. In two-dimensional MHD, three invariants which do survive truncation are the total energy, cross-helicity, and mean squared magnetic potential, although no proofs exist which guarantee that these are the only three. Additional headaches arise if one wishes to study MHD in the low magnetic-field limit, in which the magnetic invariants approach zero identically, but the enstrophy begins to change slowly enough that it should also be counted as an invariant.

Throughout, of course, careful attention must be paid to time scales. If one waits long enough, any non-zero magnetic field will destroy the constancy of the enstrophy, while at the same time, viscous and ohmic dissipation whittle away at the energy.

We have presented a filamentary model for two-dimensional MHD which is a Hamiltonian system. The Hamiltonian is equal to the *difference* between the (bulk, not thermal) kinetic energy and the magnetic energy, a parameter that has proven critical in determining behavior in previous theories, and not unlike the usual plasma β . When this quantity is large and positive, the velocity field exhibits large-scale structure in the form of two oppositely-rotating vortices at the system's longest wavelength. In this state, the magnetic field has no large-scale structure. Conversely, when the Hamiltonian is large and negative, the stream-function switches roles with the magnetic potential, and the magnetic field is organized into two large-scale magnetic islands, while the velocity field does not display long wavelength correlations. As the magnetic field is reduced in strength, this Hamiltonian approaches that of the hydrodynamical point-vortex theory, something that is not true of Fourier-based theories.

In three dimensions, a mean-field statistical calculation of singular dipoles shows that a turbulent magnetic fluid possesses a statistically favorable state in which there is no net fluid velocity, but a mean magnetic field does arise. This is reminiscent of Parker's argument [101] that the formation of filamentary fields in the convection zone of the sun is energetically favorable. Simulations bear this out, showing cylindrical concentrations of magnetic field in the complete absence of any driving forces. This statistical theory could help explain the formation of magnetic flux ropes which form in the strongly turbulent, high- β plasma of the solar photosphere, and then are carried outward by the bouyancy force. To the extent that vertical flux ropes in the photosphere can be represented two-dimensionally, our 2-d filamentary theory could explain the

tendency of these ropes to group together in granules, super-granules, and sunspots without resorting to convective forces.

Another link may be made to a recent calculation [102, 103] which shows that the fluctuation-dissipation theorem applied to a plasma gives rise to zero-frequency magnetic fluctuations, i.e., magnetic fields which are not necessarily constant throughout space, but which persist in time. What is remarkable is that the field does not arise from any driving force, but is simply a natural feature of the fluctuations around equilibrium in a plasma. In the low-frequency limit, a kinetic plasma may be described by fluid equations, and we can expect a coupling between the particle temperature and the pseudo-temperature of the vortices, which can be thought of as a temperature for long-wavelength magnetic modes. Since the discrete-dipole model also indicates that non-zero magnetic fields are statistically favored in a randomized plasma, we find this encouraging. The question of how small magnetic structures come together to form very large-scale cosmological magnetic structures is also applicable to our model.

Bibliography

- [1] H. Tasso, Phys. Lett. A **120**, 464 (1987).
- [2] A. Royer, J. Math. Phys. **25**, 2873 (1984).
- [3] K. W. Schwartz, Phys. Rev. Lett. **64**, 1130 (1990).
- [4] J. C. McWilliams, J. Fluid Mech. **146**, 21 (1984).
- [5] M. Brachet, M. Meneguzzi, H. Politano, and P. L. Sulem, J. Fluid Mech. **194**, 333 (1988).
- [6] J. C. McWilliams, Phys. Fluids A **2**, 547 (1990).
- [7] A. Pouquet, J. Fluid Mech. **83**, 1 (1978)
- [8] J. O. Stenflo, Solar Phys. **32**, 41 (1973).
- [9] F. Yusef-Zadeh, in *The Center of the Galaxy* (Boston: Kluwer, 1988), p. 243
- [10] *Physics of Magnetic Flux Ropes*, ed. C. T. Russell, E. R. Priest, and L. C. Lee (Washington D. C.: AGU, 1990)
- [11] H. Zirin, *Astrophysics of the Sun* (Cambridge: Cambridge University Press, 1988)
- [12] R. Jha, P. K. Kaw, S. K. Mattoo, C. V. S. Rao, Y. C. Saxena, and ADITYA Team, Phys. Rev. Lett. **69**, 1375 (1992).
- [13] S. Orszag and C. Tang, J. Fluid. Mech **90**, 129 (1979).

- [14] W. H. Matthaeus and D. Montgomery, Ann. NY Acad. Sci. **357** 203 (1980).
- [15] D. Biskamp and H. Welter, Phys. Fluids B **2**, 1787 (1990)
- [16] T. Tajima, J. Sakai, H. Nakajima, T. Kosugi, F. Brunel, and M. R. Kundu, Ap. J. **321**, 1031 (1987).
- [17] E. G. Zaidman and T. Tajima, Ap. J. **338**, 1139 (1989).
- [18] L. Onsager, Nuovo Cime. Suppl. **6** (9), 279 (1949).
- [19] R. H. Kraichnan and D. Montgomery, Rep. Prog. Phys. **45**, 547 (1980).
- [20] A. Hasegawa, Adv. Phys. **35**, 1 (1985).
- [21] T. D. Lee, Q. Appl. Math **10**, 69 (1952).
- [22] R. H. Kraichnan, Phys. Fluids **8**, 575 (1965).
- [23] R. H. Kraichnan, Phys. Fluids **10**, 1417 (1967).
- [24] R. H. Kraichnan, J. Fluid Mech. **67**, 155 (1975).
- [25] J. B. Taylor and B. McNamara, Phys. Fluids **14**, 1492 (1971).
- [26] J. B. Taylor, Phys. Lett. A **40**, 1 (1972).
- [27] S. F. Edwards and J. B. Taylor, Proc. R. Soc. Lond. **336A**, 257 (1974).
- [28] S. E. Seyler, Jr., Phys. Fluids **19**, 1336 (1976).
- [29] J. G. Joyce and D. Montgomery, J. Plasma Phys. **10**, 107 (1973).
- [30] D. Montgomer and G. Joyce, Phys. Fluids **17**, 1139 (1974).
- [31] Y. B. Pointin and T. S. Lundgren, Phys. Fluids **19**, 1459 (1976).

- [32] T. S. Lundgren and Y. B. Pointin, *J. Stat. Phys.* **17**, 323 (1977).
- [33] T. S. Lundgren and Y. B. Pointin, *Phys. Fluids* **20**, 356 (1977).
- [34] T. Huld, A. H. Nielsen, H. L. Pécseli, and J. Juul Rasmussen, *Phys. fluids B* **3**, 1609 (1991).
- [35] C. E. Seyler, Jr., Y. Salu, D. Montgomery, and G. Knorr, *Phys. Fluids* **18**, 803 (1975).
- [36] C. Basdevant and R. Sadourny, *J. Fluid. Mech.* **69**, 673 (1975).
- [37] L. C. Kells and S. A. Orszag, *Phys. Fluids* **21**, 162 (1978).
- [38] R. Benzi, G. Paladin, S. Patarnello, P. Santangelo, and A. Pulpiani, *J. Phys. A* **19**, 3771 (1986).
- [39] P. Santangelo, R. Benzi, and B. Legras, *Phys. Fluids A* **1**, 1027 (1989).
- [40] J. C. McWilliams, *J. Fluid Mech.* **219**, 361 (1990).
- [41] A. N. Kolmogorov, *Dokl. Akad. nauk SSR* **30**, 301 (1941).
- [42] H. A. Rose and P. S. Sulem, *J. Physique* **39**, 441 (1978).
- [43] G. F. Carnevale, J. C. McWilliams, Y. Pomeau, J. B. Weiss, and W. R. Young, *Phys. Rev. Lett.* **66**, 2735 (1991).
- [44] W. H. Matthaeus, W. T. Stribling, D. Martinez, S. Oughton, and D. Montgomery, *Physica D* **51**, 531 (1991).
- [45] J. B. Taylor, *Rev. Mod. Phys.* **58**, 741 (1986).
- [46] V. A. Gordin and V. I. Petviashvili, *Zh. Eksp. Teor. Fiz.* **95**, 1711 (1989).
 [Sov. Phys. JETP **68**, 988 (1989)].
 A.D. Beklemishev, V. A. Gordin, R. R. Khayrutdinov, V. I. Petviashvili,
 and T. Tajima, submitted to *Nucl. Fusion* (1991).

- [47] D. Biskamp, Comments Plasma Phys. **10**, 165 (1986).
- [48] J. Y. Hsu and M. S. Chu, Phys. Fluids **30**, 1221 (1987).
- [49] B. B. Kadomtsev, Sov. J. Plasma Phys. **13**, 443 (1987).
- [50] W. H. Bennett, Phys. Rev. **45**, 890 (1934).
- [51] J. B. Taylor, IFS preprint # 447 (1991).
- [52] D. J. Tetreault, Phys. Fluids **32**, 2122 (1988).
D. J. Tetreault, Phys. Fluids **B1**, 511 (1989);
D. J. Tetreault, Phys. Fluids **B2**, 53 (1990);
- [53] D. Montgomery, L. Turner, and G. Vahala, J. Plasma Phys. **21**, 239 (1979).
- [54] J. Ambrosiano and G. Vahala, Phys. Fluids **24**, 2253 (1981).
- [55] B. V. Chirikov, Phys. Rep. **52**, 263 (1979).
- [56] Y. H. Ichikawa, T. Kamimura, and T. Hatori in *Statistical Physics and Chaos in Fusion Plasmas*, ed. C. W. Horton and L. E. Reichl, (John Wiley and Sons, 1984) 21.
- [57] J. P. Christiansen, J. Comp. Phys. **13**, 363 (1973).
- [58] W. W. Lee and H. Okuda, J. Comp. Phys. **26**, 139 (1978).
- [59] Irie, private communication (1991).
- [60] D. Fyfe and D. Montgomery, J. Plasma Physics **16**, 181 (1976).
D. Fyfe, G. Joyce, and D. Montgomery, J. Plasma Physics **17**, 317 (1977).
D. Fyfe, D. Montgomery, and G. Joyce, J. Plasma Physics **17**, 369 (1977).
- [61] W. M. Elsasser, Phys. Rev. **79**, 183 (1950).

- [62] J. W. Belcher and L. Davis, *J. Geophys. Res.* **76**, 3534 (1971).
- [63] C. K. Birdsall, A. B. Langdon, and H. Okuda, in *Methods of Computational Physics*, vol. 9, ed. by B. Alder, S. Fernback, and M. Rotenberg (Academics: New York, 1970).
- [64] R. W. Hockney and J. W. Eastwood, *Computer Simulation Using Particles* (Mcgraw-Hill, New York, 1985).
- [65] T. Tajima *Computational Plasma Physics: With Applications to Fusion and Astrophysics* (Addison-Wesley: New York, 1989).
- [66] E. A. Novikov and Yu. B. Sedov, *Sov. Phys. JETP* **50**, 297 (1979).
- [67] K. M. Khanin, *Physica D* **4**, 261 (1982).
- [68] J. B. Weiss and J. C. McWilliams, *Phys. Fluids* **A3**, 835 (1991).
- [69] S. Douady, Y. Couder, and M. E. Brachet, *Phys. Rev. Lett.* **67** (8), 983 (1991).
- [70] R. M. Kerr, *J. Fluid Mech.* **153**, 31 (1985).
- [71] Y. Kimura, to appear in *Topological Aspects of the Dynamics of Fluids and Plasmas*, proceedings of the Program of the Institute for Theoretical Physics, ed. by H. K. Moffatt, G. M. Zaslavsky, M. Tabor, and P. Comte (Kluwer: Dordrecht, Netherlands).
- [72] R. Grauer and T. Sideris, *Phys. Rev. Lett.* **67**, 3511 (1991).
- [73] R. Harris and J. Hearst, *J. Chem. Phys.* **44**, 2595 (1966).
- [74] N. Saito, K. Takahashi, and Y. Yunoki, *J. Phys. Soc. Japan* **22**, 219 (1967).
- [75] S. Kida, *J. Fluid Mech.* **112**, 397 (1981).

- [76] A. Pumir and E. Siggia, *Phys. Fluids* **30** (6), 1606 (1987).
- [77] T. Stribling and W. H. Matthaeus, *Phys. Fluids B* **2** (9), 1979 (1990).
- [78] U. Frisch, A. Pouquet, J. Léorat, and A. Mazure, *J. Fluid Mech.* **68**, 769 (1975).
- [79] D. Montgomery, L. Turner, and G. Vahala, *Phys. Fluids* **21**, 757 (1978).
- [80] S. G. Chefranov, *Sov. Phys. JETP* **66** (1), 85 (1987).
- [81] P. H. Roberts, *Mathematika* **19**, 169 (1972).
- [82] D. R. Nelson, *Phys. Rev. Lett.* **60**, 1971 (1988).
- [83] J. O. Stenflo, *Astron. Astrophys. Rev.* **1**, 3 (1989).
- [84] C. T. Russell, E. R. Priest, and L. C. Lee, *Physics of Magnetic Flux Ropes* (American Geophysical Union, Washington D.C., 1990).
- [85] C. Zwaan, *Solar Phys.* **100**, 397 (1985).
- [86] W. Feneberg and G. H. Wolf, *Nucl. Fusion* **21**, 669 (1981).
S. C. McCool, A. J. Wootton, A. Y. Aydemir, R. D. Bengtson, J. A. Boedo, R. V. Bravenec, D. L. Brower, J. S. DeGrassie, T. E. Evans, S. P. Fan, J. C. Forster, M. S. Foster, K. W. Gentle, Y. X. He, R. L. Hickock, G. L. Jackson, S. K. Kim, M. Kotschenreuther, N. C. Luhmann, Jr., W. H. Miner, Jr., N. Ohyaabu, D. M. Patterson, W. A. Peebles, P. E. Phillips, T. L. Rhodes, B. Richards, C. P. Ritz, D. W. Ross, W. L. Rowan, P. M. Schoch, B. A. Smith, J. C. Wiley, X. H. Yu, S. B. Zheng, *Nucl. Fusion* **29**, 547 (1989).
- [87] P. L. Similon and R. N. Sudan, *Ap. J.* **336**, 442 (1989).
- [88] J. M. Kosterlitz, *J. Phys. C* **7**, 1046 (1974).

- [89] R. A. Smith, Phys. Rev. A **43**, 1126 (1991).
- [90] V. Berdichevsky, I. Kunin, and F. Hussain, Phys. Rev. A **43**, 2050 (1991).
- [91] L. J. Campbell and K. O'Neil, J. Stat. Phys. **65**, 495 (1991).
- [92] J. Bouchaud, M. Mézard, and J. Yedidia, Phys. Rev. Lett. **67**, 3840 (1991).
- [93] G. Goldin, R. Menikoff, D. Sharp, Phys. Rev. Lett. **67**, 3499 (1991).
- [94] H. Safar, P. L. Gammel, D. A. Huse, D. J. Bishop, J. P. Rice, D. M. Ginsberg, Phys. Rev. Lett. **69**, 824 (1992).
- [95] M. Charalambous, J. Chaussy, P. Lejay, Phys. Rev. B **45**, 45 (1992).
- [96] Y. Wu, Phys. Rev. Lett. **53**, 111 (1984).
- [97] N. Manton, Phys. Rev. Lett. **67**, 1462 (1991).
- [98] C. Trugenberger, R. Menikoff, and D. Sharp, Phys. Rev. Lett. **67**, 1922 (1991).
- [99] M. Sporre, J. Verbaarschot, and I. Zahed, Phys. Rev. Lett. **67**, 1813 (1991).
- [100] J. B. Taylor, presented at IFS staff seminar (1992).
- [101] E. N. Parker, Ap. J. **191**, 245 (1974).
- [102] T. Tajima, S. Cable, K. Shibata, and R. M. Kulsrud, Ap. J. **390**, 309 (1992).
- [103] S. Cable and T. Tajima, Phys. Rev. A **46**, 3413 (1992).

Vita

Rodney Michael Kinney was born on July 28, 1963 in Minneapolis, Minnesota to Robert and Carol Kinney, where he spent many nights sleeping and sucking his thumb in his father's laboratory. He grew up in love with the Sonoran desert around Tucson, Arizona, acquiring a passion for playing the piano which persists to this day. In 1981, he left for Pasadena, California to attend the California Institute of Technology, at which Blacker House and the student body in general taught him many social skills of questionable value, while the faculty filled his head with physics. Graduating with honors in 1985, he came directly to Austin, Texas and the University thereof, where he discovered Toshiki Tajima, to become his academic advisor, and Lari Mychelle Larimer, to become his beloved wife.

Permanent address: c/o Robert and Carol Kinney
456 22nd Ave. SE
St Petersburg, FL 33705

This dissertation was typeset with \LaTeX^\dagger by the author.

[†] \LaTeX is a document preparation system developed by Leslie Lamport as a special version of Donald Knuth's \TeX Program.